Fall 8-16-2024

There and Back Again: Creating, Characterizing, and Curing Murine Models of Rare Neuromuscular Disease

Sarah Holbrook
University of Maine of Orono, holbrook.sarah@maine.edu

THERE AND BACK AGAIN: CREATING, CHARACTERIZING, AND CURING MURINE MODELS OF RARE

NEUROMUSCULAR DISEASE

By

Sarah Holbrook

B.S. University of Maine, 2017

A DISSERTATION

Submitted in Partial Fulfillment of the

Requirements for the Degree of

Doctor of Philosophy

(in Biomedical Science)

The Graduate School

The University of Maine

June 2024

Advisory Committee:

Gregory A. Cox, Associate Professor, The Jackson Laboratory, Advisor

Robert W. Burgess, Professor, The Jackson Laboratory

Catherine Kaczarowski, Associate Professor, The Jackson Laboratory

Dustin Updike, Assistant Professor, Mount Desert Biological Laboratory

Bruce O' Hara, Professor, The University of Kentucky

THERE AND BACK AGAIN: CREATING, CHARACTERIZING, AND CURING MURINE MODELS OF RARE

NEUROMUSCULAR DISEASE

By Sarah Holbrook

Thesis/Dissertation Advisor: Dr. Gregory
Cox

An Abstract of the Thesis/Dissertation
Presented in Partial Fulfillment of the
Requirements for the
Degree of Doctor of Philosophy in
(Biomedical Sciences)
August 2024

Orphan diseases, or diseases that affect less than 200,000 people around the globe, are less extensively researched leaving patients with questions and often without treatments let alone a cure. Developing models to research orphan diseases requires documentation of the few human patients suffering from the disease, development of a model, and extensive phenotyping of that model to determine viability as a translatable model of the disease. This dissertation is in itself rare as it follows the development of an animal model all the way through to human clinical trials of an Investigational New Drug. The disease of interest is a severe neuromuscular degenerative disease called Spinal Muscular Atrophy with Respiratory Distress type 1, or SMARD1, affecting young children. This disease is caused by recessive mutations in *IGHMBP2 and* marked by diaphragmatic paralysis within the first years of life leading to respiratory distress followed by severe muscular atrophy starting in the distal limbs. However, there is phenotypic severity with some milder cases occurring later in childhood not always accompanied by respiratory distress categorized as a Charcot-Marie-Tooth disease type 2S (CMT2S) and even some more severe cases initially diagnosed as Sudden Infant Death Syndrome (SIDS). As such, to reflect the range of disease severity, the Cox lab made several models via CRISPR. The 11 alleles made

encompass off-target mutations as well as human alleles. Through histological analysis of key muscles and nerves and genetic crosses of transgenic models, the spectrum of severity has been documented as well as the fact that *IGHMBP2* associated diseases are neurogenic though do impact muscle as well. To test respiratory distress of these animals, the PiezoSleep system was troubleshooted to analyze breath rate and it was found that there is indeed respiratory distress in our severe models. RNAseq of the spinal cords also indicated that the RNA sensing innate immune system pathway, the RIG-I Like Receptor pathway, played a part in these diseases as well as NEMF associated diseases. Due to these models and phenotyping, we were able to test gene therapy in these models finding that treatment greatly mitigated the NMD phenotype and lengthened lifespan. The creation and characterization, of rare disease models are vital to creating and testing therapeutics. The relationship between IGHMBP2 and NEMF also shows potential for finding novel categories of neuromuscular disease opening up avenues for treatments that treat a larger amount of patients as well as increase our understanding of neuromuscular development and maintenance.

DEDICATION

This dissertation is dedicated to Jack Dupal, Charlotte Hanson, Uncle Frank Anicetti, Jimmy Huston, Harold Scott, Gerald St. Pierre, Shirley Huston, Michael Holbrook, 'Jackie' Fowler and most importantly, my mum, 'Tiny' Holbrook. These were all family and dear friends who believed I could become Dr. Holbrook when I started my journey towards a PhD, but passed away before I was able to accomplish that title.

ACKNOWLEDGEMENTS

TABLE OF CONTENTS

LIST OF FIGURES

CHAPTER 1

Characterizing Novel Mouse Models of Rare Disease

1.1 Introduction

In the United States, the definition of rare disease constitutes a condition that impacts less than 200,000 people. Some conditions are so rare that only 1 person has been recorded with said disease. These diseases are often named after a person diagnosed with the disease (sometimes the first person or a particularly famous person such as Lou Gehrig's disease so named after the famous baseball player) or after the clinicians or researchers who first discovered it (such as Charcot Marie Tooth disease after the first three researchers documenting similarly presenting conditions (Martin et al., 2019; Mead et al., 2023; Kazamel et al., 2015).

1.2 Commonly Rare

However, despite each individual disease being rare, 1 in 10 Americans is afflicted with a rare disease with ~2/3 of rare disease cases being children. 72% of rare disease are genetic in origin with ~80% of said mutations being inherited (eClinicalMedicine, 2023). Many neuromuscular diseases are rare and developmental leading to an array of symptoms not limited to impacted mobility, respiratory distress, trouble swallowing, and early onset of death conditions (Martin et al., 2019; Mead et al., 2023). Due to the complicated mechanisms underlying the neuromuscular system and the long networks of glial cells, neurons, and muscles, a deficit in one part of the system can have catastrophic results on the entire neuromuscular relay. From spinal motor neurons to acetylcholine receptors, scientists and clinicians must assess each aspect of the neuromuscular system, and sometimes beyond, to determine the root of the problem. This requires holistic expertise in analyzing gene expression, histological assays, behavioral tests, and creative thinking in order to understand a neuromuscular disease. This is of particular importance in rare diseases where very little research may have been conducted meaning many rare

disease researchers are exploring unknown territory. Due to this rarity, rare diseases are sometimes

called 'orphan' disease due to no research or treatment being dedicated to them. In fact, only 5% of rare

diseases have a treatment available and only 1/3 of potential patients have access to them

(eClinicalMedicaine, 2023). As genomic testing and phenotypic assessments, especially for younger

patients, improve, the number of genes associated with neuromuscular disorders increases. Since 2017,

an average of 27 genes are documented annually (Yubero et al., 2021).

1.3 A Need

Despite this increased need in personalized medicine and rare disease research, clinical trials and studies

are often expensive. With few people being afflicted by a particular rare disease and fewer people

studying said diseases, animal models or patient cell cultures can be hard to find and labs willing to

investigate said disease even harder. If treatments are found in these labs, then it will be difficult to

have pharmaceutical backing for potential clinical trials. Even beyond that, if funding is found for each of

these steps, finding patients that are applicable for said trials and being able to transport them can

sometimes be difficult due to the nature of the diseases making transportation incredibly difficult.

Undeterred by these challenges, many patient foundations, labs, and some companies are in rare

disease work. From free flight transportation for patients from organizations like Angel Flight to

investment in clinical trials from medical technology companies such as Alcyone, these entities have

progressed the knowledge, technology, and treatments available to patients as well as their emotional

well-being. Since the first FDA approved cell-based therapy, tisagenlecleucel, was released to the public

in 2017, 17 more cell and gene therapy-based treatments have been approved for conditions such as

Spinal Muscular Atrophy (SMA) and hemophilia with dozens of trials in progress (Tufts Medical Center,

2023). With each trial, clinical and pre-clinical, techniques are refined and improved. Cell specificity in

gene therapy is being improved through directed evolution of the capsids of adeno-associated viruses

(AAV) to better target specific cells combatting the complication of the liver sequestering most of the

AAV gene therapy treatment (Choudhury et al., 2016; Li et al., 2016). The liver can sequester so much of

a gene therapy dose, that for therapies that must reach large tissues such as the skeletal muscle, it

would require toxic doses of virus to reach the cells that need the treatment (Morales et al., 2020). Gene

therapy vectors have also been evolved in labs in ways to combat hurdles like the blood-brain barrier

making gene therapy transfer to the spinal cord less invasive via an intravenous injection rather than an

intrathecal or intracerebroventricular injection (Nonnenmacher et al., 2021).

1.4 Beyond Need, A Yearning

Besides such research in rare diseases evolving at an exponential rate and the diagnostics for said

diseases improving, rare diseases hold vital information about the development and maintenance of our

bodies. Understanding the role of a gene in a rare disease allows us to know how and why that

particular gene is vital to our well-being. For example, retinitis pigmentosa (RP), is a disorder associated

with abnormalities in the photoreceptors and/or retina of the eyes leading to vision loss. There have

been over 40 genes associated with RP some of which are dominant, recessive, or X-linked. The study of

these genes has lead to more knowledge about the development of the retina as well as essential

vitamins and avenues of treatment for vision loss that are not exclusive to RP (Ferrari et al., 2011).

When it comes to neuromuscular disease, any injury or mutation causing any part of the neuromuscular

system from the cerebellum, the schwann cells, to the mitochondria of the muscles can greatly impact

the whole system and impact mobility causing widespread effects. Mutations resulting in deficits in

myelination, axonal growth, metabolism, stress response, translation, and ribosome quality control in

the neurons, muscles, and or supporting glial and structural cells are common causes of neuromuscular

disease (Martin et al., 2019). Though some gene mutations are specific to the muscles and/or nerves,

there are also ubiquitously expressed genes such as IGHMBP2 that seem to impact the motor neurons

especially. This may be due to the metabolic and translational burden of the muscles and motor neurons due to their length (with some motor neurons reaching over 1 meter) and energy expenditure (De Vos et al., 2017, Chen et al., 2022).

1.5 My Part

The following dissertation will guide you through my small part in the rare neuromuscular disease field. The creation of a spectrum of neuromuscular rare disease murine models, the characterization of said murine models through their behaviors, muscles, and nerves, and finally the quest for a cure through hard work, creativity, passion, and just a little luck.

CHAPTER 2

Characterizing the Severe Side of the Spectrum of Disease associated with IGHMBP2

Clinically relevant mouse models of severe Spinal Muscular Atrophy with Respiratory Distress type 1

Sarah E. Holbrook[1,2,], Amy N. Hicks[1], Paige B. Martin[1], Timothy J. Hines[1], Harold P. Castro[1], *Gregory A. Cox[1,2]

1. The Jackson Laboratory, Bar Harbor, ME, USA

2. The University of Maine, Orono, ME, USA

*Corresponding author:

The University of Maine, 168 College Ave., Orono, ME, USA

Telephone: 207-581-3071

Email: gregory.a.cox@maine.edu

Abstract

Spinal Muscular Atrophy with Respiratory Distress (SMARD1) is a lethal infantile disease, characterized by the loss of motor neurons leading to muscular atrophy, diaphragmatic paralysis, and weakness in the trunk and limbs. Mutations in *IGHMBP2*, a ubiquitously expressed DNA/RNA helicase, have been shown to cause a wide spectrum of motor neuron disease. Though mutations in *IGHMBP2* are mostly associated with SMARD1, milder alleles cause the axonal neuropathy, Charcot-Marie-Tooth disease type 2S (CMT2S), and some null alleles are potentially a risk factor for sudden infant death syndrome (SIDS). Variant heterogeneity studied using an allelic series can be informative in order to create a broad spectrum of models that better exhibit the human variation. We previously identified the *nmd*[2J] mouse model of SMARD1, as well as two milder CMT2S mouse models. Here, we used CRISPR-Cas9 genome editing to create three new, more severe Ighmbp2 mouse models of SMARD1, including a null allele, a deletion of C495 (C495del) and a deletion of L362 (L362del). Phenotypic characterization of the IGHMBP2[L362del] homozygous mutants and IGHMBP2[C495del] homozygous mutants respectively show a more severe disease presentation than the previous *nmd*[2J] model. The IGHMBP2[L362del] mutants lack a clear denervation in the diaphragm while the IGHMBP2[C495del] mutants display a neurogenic diaphragmatic phenotype as observed in SMARD1 patients. Characterization of the *Ighmbp2*-null model indicated neo-natal lethality (median lifespan=0.5days). These novel strains expand the spectrum of SMARD1 models to better reflect the clinical continuum observed in the human patients with various *IGHMBP2* recessive mutations.

2.1 Introduction

Spinal muscular atrophy with respiratory distress type 1 (SMARD1; OMIM#604320) is an autosomal

recessive disease caused by mutations in the ubiquitously expressed DNA/RNA helicase,

immunoglobulin μ-binding protein (*IGHMBP2*) (Grohmann et al., 2001, Grohmann et al., 2004). Although

SMARD1 was the first disease to be associated with *IGHMBP2,* within recent years, it has been observed

that variants in *IGHMBP2* can give rise to a whole spectrum of motor neuron disease (MND), including

Charcot-Marie-Tooth disease type 2S (CMT2S), a later-onset sensorimotor peripheral neuropathy

(Cottenie et al., 2014). SMARD1 patients have an initial onset of distal limb weakness between 6 weeks

and 6 months of age, respiratory distress with diaphragmatic weakness, and often require ventilator

dependence and nutritional support (Pitt et al., 2003, Viguier et al., 2018). Less severe presentations are

classified as CMT2S, which is defined by axonal motor and sensory involvement in a length-dependent

manner and an absence of diaphragmatic weakness (Cottenie et al., 2014, Wagner et a., 2015).

While it is known that *IGHMBP2* variants cause motor neuron diseases (MNDs), it is unknown why this

ubiquitously-expressed helicase is critical for motor neuron viability. The spectrum of MNDs suggests

that allelic combination and genetic modifiers are likely to play a role in disease severity (7-9). Cases of

patients with inherited homozygous or compound heterozygous putative null alleles typically have the

earliest onset and most severe symptoms (Grohmann et al., 2001, Grohmann et al., 2004, Guenther et

al., 2009). Atypical cases of *IGHMBP2*-associated diseases have occurred, such as intrafamilial

heterogeneity (Wagner et al., 2015, Joseph et al., 2009) and late-onset respiratory symptoms (Vanoli et

al., 2015). Phenotypic heterogeneity within the human population indicates a clinical continuum of

severity, and understanding the impact of mutation contribution to severity may lend insight to the

overall function of IGHMBP2 in motor neuron viability. Addressing these questions with mouse models

can enhance our understanding of IGHMBP2's function, as well as provide essential resources for pre-clinical assessment of much needed therapeutics.

2.1.1 Null alleles in humans and mice: a novel model of SIDS

Sudden infant death syndrome (SIDS) has also been loosely associated with mutations in *Ighmbp2.* Three families (Grohmann et al., 2004, Jackson et al., 2017), as well as two families that we have had personal correspondence with had a first-born child potentially carrying mutations in *IGHMBP2* and diagnosed as SIDS. Not until a subsequent child, with similar respiratory distress presentation, did they get a genetic diagnosis*,* which confirmed mutations in *IGHMBP2*. While 5 families seems to be minimal or anecdotal, the overall rarity of this disease means that there are only about 90 published cases in which about 5% have reported sibling SIDS diagnoses. *IGHMBP2* -associated SIDS may be under diagnosed as molecular autopsies of SIDS patients is still not common practice and the panels that are used often focus on genes associated with cardiac dysfunction (Campuzano et al., 2018, Scheiper et al., 2018). Models for *IGHMBP2* – associated SIDS will be critical to identify the function of IGHMBP2 in neurodevelopment and to allow for the basis of *IGHMBP2* screening in SIDS cases.

One critical barrier to studying *IGHMBP2*-associated diseases and potential therapeutics is the dearth of models representing the phenotypic heterogeneity observed in patients. We have previously discovered and defined a mouse model on the C57BL/6J background that currently represents SMARD1 (Cox et al., 1998). This model harbors a mutation in a splice donor site, causing mis-splicing of the mRNA ~80% of the time (Cox et al., 1998). These mice (nmd^{2J}) still maintain ~20% wildtype protein levels and have a motor neuron disease onset at about 2-3 weeks of age, with a median lifespan of 91.5 days. While this model recapitulates much of the disease phenotype of SMARD1 patients, the hallmark diaphragmatic paralysis observed in human patients is absent. Even at end of life, these mice maintain innervation of the diaphragm and many of the trunk muscles that are necessary for respiration (Grohmann et al., 2001,

Shababi et al., 2018). Much of what we know about the disease, including its impact in motor neurons is based on findings in this *nmd*[2J] mutation, but it is clear that the *nmd*[2J] model is insufficient for understanding the entire range of *IGHMBP2*-associated diseases. Additional novel models recapitulating the phenotypic spectra observed in patients are an essential tool to determine the severity and phenotypes of other hypomorphic and null mutations, as well as identify the therapeutic window for treating early-onset presenting patients.

2.1.2 Hypomorphic IGHMBP2 alleles in human and mice: A better mouse model of SMARD1

The primary model used for studying SMARD1 had been the *nmd*[2J] model, which we previously reported (Grohmann et al., 2001, Cox et al., 1998) until the recent description of the **Ighmbp2**[D564N] model (Smith et al., 2022). The *nmd*[2J] model has been critical for dissecting pathomechanisms, but is not without its limitations. One such limitation is that the nature of the mutation is a splicing variant, which causes the mRNA to mis-splice about 80-90% of the time. This hypomorphic mouse has reduced levels of otherwise wildtype protein, which should be able to function at a normal enzymatic capability.

2.1.3 Creating a Spectrum of Murine Phenotypes

Here we report the creation and characterization of three novel mutations in *Ighmbp2*, each of which causes phenotypes previously unseen in the *nmd*[2J] model. The first mutation, a single amino acid deletion, IGHMBP2[L362del], has an earlier onset and greater severity compared to the established *nmd*[2J] mouse. The second mutation, IGHMBP2[C495del], is also a single amino acid deletion in a different exon that causes an even earlier onset MND phenotype. The third novel mutation, an early termination and protein-null mutation, presents as a neonatal lethal model. Analyses of lifespan, neuromuscular junctions, distal nerves, and muscle histology indicate that all three models have an earlier onset more severe presentation of distal axonopathy than the previously defined *nmd*[2J] model, which is already more severe than our recently described CMT2S models (Martin et al., 2023). These new models will

provide the basis for research and pre-clinical trials representing human patients with more severe forms of SMARD1.

2.2 Results

2.2.1 CRISPR-Cas9 Induced Mutations

Using CRISPR-Cas9 genome editing, we targeted exon 8 of mouse *Ighmbp2* to recreate a known allele *nmd^J* (p.L362del) that was reportedly viable, but phenotypically more severe than *nmd^2* [7]. In addition to the targeted allelic event, we identified a founder carrying a novel insertion and deletion resulting in a frameshift and early stop codon. From identified founders we genotyped *Ighmbp2^{em3}* (henceforth IGHMBP2^{L362del}), the targeted historical allele, and *Ighmbp2^{em4}* (henceforth IGHMBP2-null). We also created *Ighmbp^{em6}* (henceforth IGHMBP2^{C495del}), based off a severe patient mutation that showed respiratory distress 3 days after birth (Grohmann et al., 2004).

2.2.2 Hypomorphic IGHMBP2^{L362del} and IGHMBP2^{C495del} mutations cause decreased growth and shortened lifespan

Initial characterization of the IGHMBP2^{L362del} mutation (*Ighmbp2^{em3}*), a recapitulation of the lost *nmd^{1J}* strain with a reportedly more severe *nmd* allele (Cox et al., 1998), showed that homozygous mice, are smaller than wildtype littermates by two weeks of age. Mice homozygous for the IGHMBP2^{C495del} mutation are smaller than the IGHMBP2^{L362del} mutants, (**Figure 1a,b**) and failed to gain weight during their 7 day lifespan (**Figure 1c**). IGHMBP2^{C495del} mutants also have a shorter lifespan of ~ 7 days while the median lifespan of IGHMBP2^{L362del} mutants are 20.5 days. These are both more severe than the historical *nmd^{2J}* mutant model, which has a median lifespan of 91.5 days (**Figure 1d**). A small but notable fraction (~20%) of the IGHMBP2^{L362del} mutant mice, lived past 4 weeks of age. Long-lived IGHMBP2^{L362del} mutant mice were still smaller than littermates, with hindlimb wasting and deficits in motor function. At one

week of age, IGHMBP2^{L362del} mutants are overtly similar to wildtype littermates; however, by two weeks many are very small, with some unable to right themselves. IGHMBP2^{C495del} mutants are notably different at one week of age, weighing significantly less by p4, and show difficulty righting themselves at p4 (**Figure 1b**).   When IGHMBP2^{L362del} mutant mice are tested for motor function at 2 weeks of age with an inverted wire hang assessment, IGHMBP2^{L362del} mutant mice are unable to perform the task; this does not improve for mice surviving past 3-4 weeks of age. IGHMBP2^{C495del} mutant mice did not live past p9 and are therefore not able to be assessed by the wire hang assay (not shown).

Figure 1. The L362del variant in Ighmbp2 caused growth deficiencies and shortened lifespans.
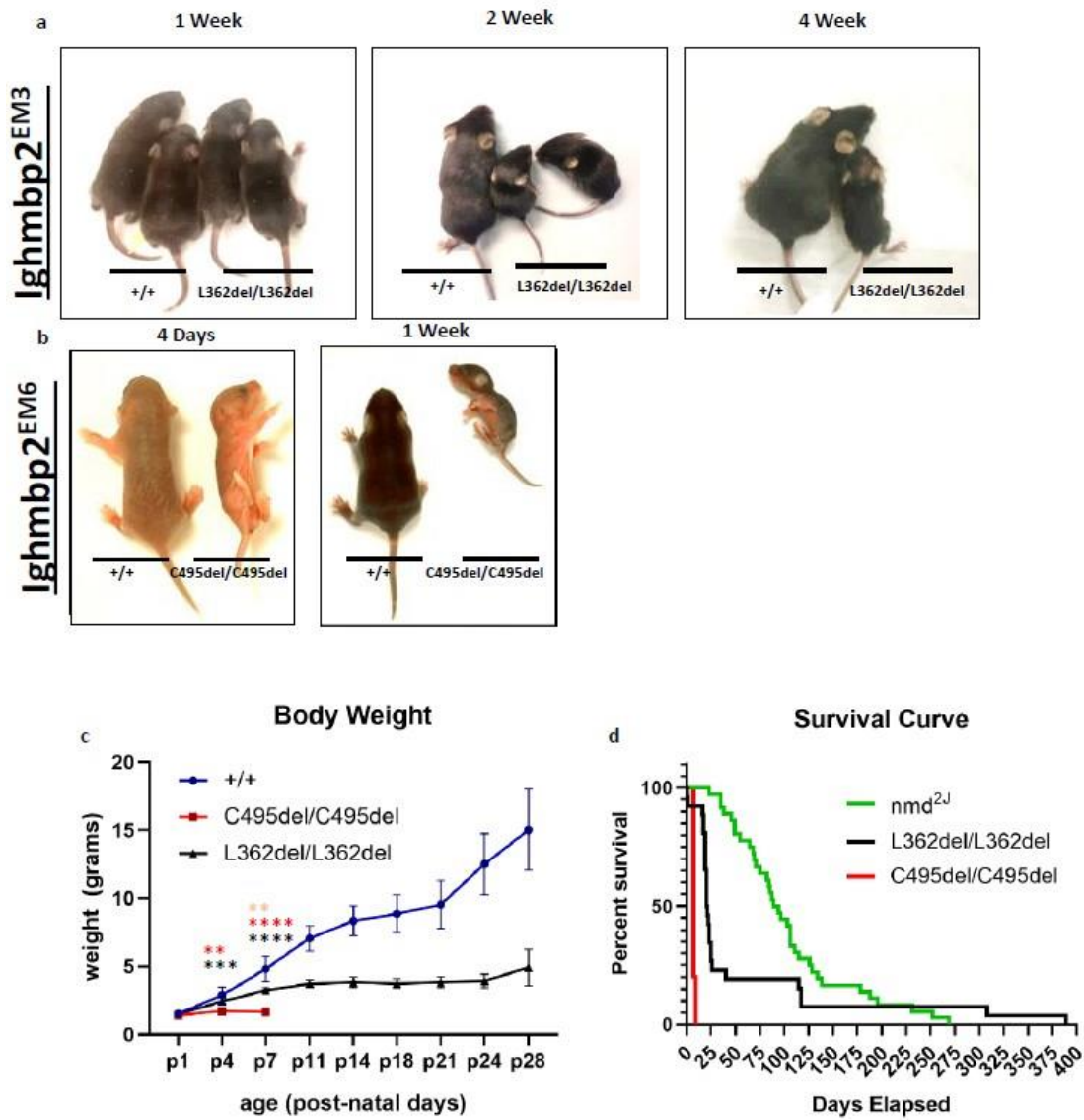
Figure 1. The L362del variant in Ighmbp2 caused growth deficiencies and shortened lifespans. (a) Deletion of three nucleotides CTG in exon 8 (c. 1084_1086del) causes an in-frame single amino acid deletion (p.L362del). (b) Wildtype (+/+) and mutant (L362del) mice are smaller, but not overtly smaller at one week. However, by 2 weeks of age the mice are significantly smaller in size and some are unable to right themselves. Mice that survive past three to four weeks are smaller overall in body size with significant atrophy in the hindlimbs. (c) Growth curve of mixed sex L362del mutants, L362del heterozygous, and wildtype (+/+) littermates. +/+ (week 2: n=3; 8.93±1.38, week 3: n=5; 10.38±.722) heterozygous (week 1: n=10, 4.76±.74, week 2: n=14, 8.2±1.66, week 3: n=5, 9.72±.74, week 4: n=4, 15.9±.6) and mutant (week 1: n=6, 3.07±.16, week 2: n=11, 3.4±.919, week 3: n=5, 5.12±2.35, week 4: n=3, 3.8±.265). Two way ANOVA with Sidak multiple of het v wt . Week 1 p=0.398 (*), Week 2 p<0.0001 (****), Week 3 p<0.0001 (****), Week 4 p<0.0001 (****). (d) Survival curve of L362del mutants (n=26, median=20.5days) compared to wildtype littermates show a reduced lifespan. When compared to the historical data for the nmd2J/2J (n=36, median= 91.5 days) are observed as having an earlier and more severe lifespan. Log-rank (Mantel-Cox) p=0.0103 (*).

2.2.3 IGHMBP2[L362del] and IGHMBP2[C495del] mutant mice do not display diaphragmatic paralysis. A

hallmark presentation of SMARD1 is respiratory distress caused by diaphragmatic paralysis and phrenic

palsy, a phenotype that the *nmd[2J]* mouse does not model well (Grohmann et al., 2004, Villalón et al.,

2018). We assessed histological changes in two main breathing muscles, the diaphragm and intercostals,

to determine if rapid progression of disease and premature death in IGHMBP2[L36del] and IGHMBP2[C495del]

mutants respectively are due to respiratory distress. In human patients' x-rays of the chest

cavity, there is a protrusion of the diaphragm into the chest cavity. Similarly, IGHMBP2[L362del] mutant

mice exhibit protrusion of the diaphragm into the chest cavity, compared to the wildtype littermates

which appear to have a broader, flatter diaphragm as expected (**Figure 2a-c**).

14

Figure 2. L362del mutation more severely impacts intercostal muscles than nmd2J or wildtype.

Figure 2
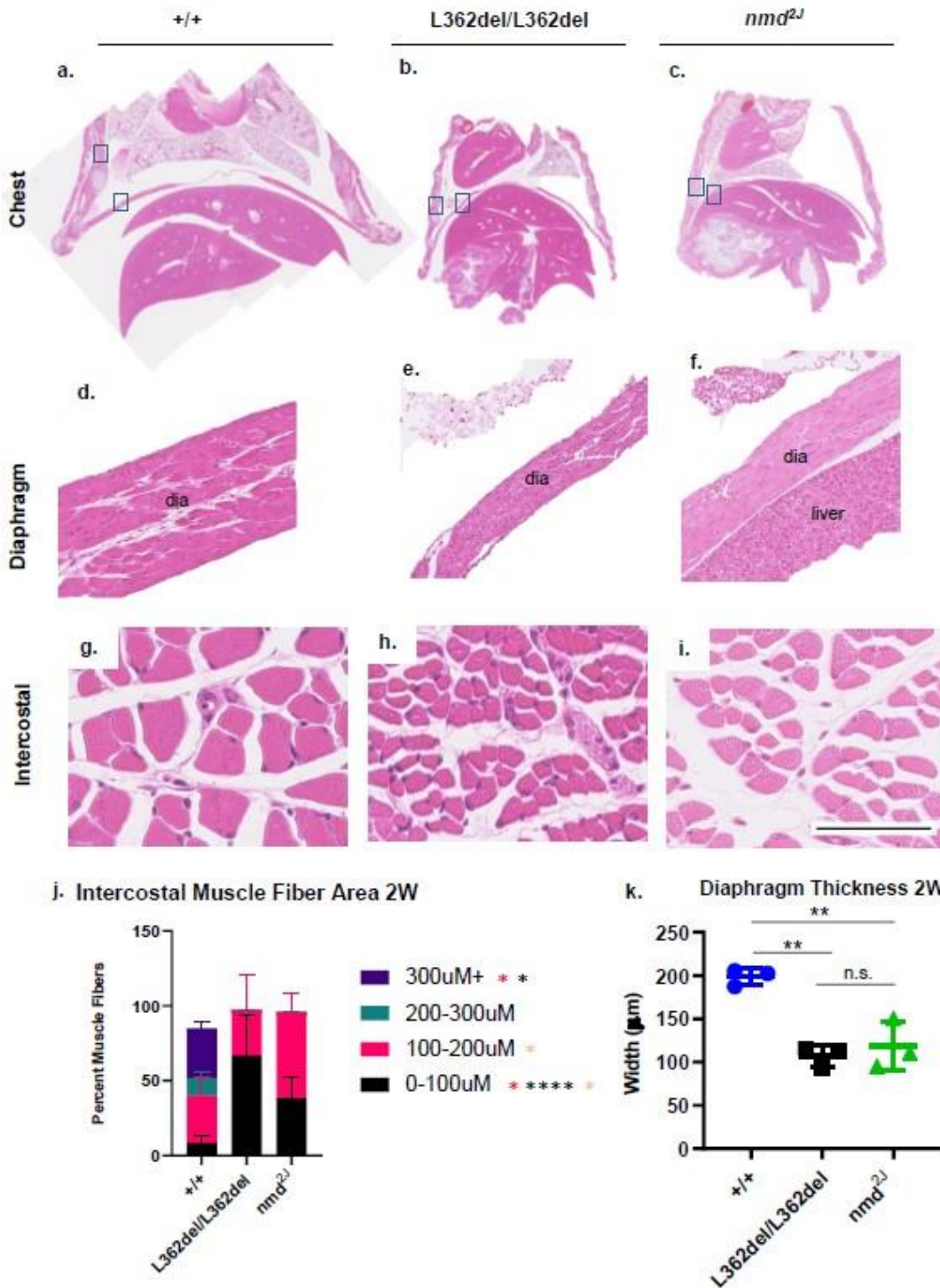
Figure 2. L362del mutation more severely impacts intercostal muscles than nmd2J or wildtype. At two weeks of age whole chest cavity cross sections of wildtype (a), L362del (b,c) and nmd2J (d), show that L362del and nmd2J are smaller overall in size. Cross section of diaphragms from the whole chest cavity shows thinner diaphragms for L362del (f,g) and nmd2J (h) compared to a wildtype (e). Cross-sections of the intercostal muscle show that wildtype (i) has larger more robust muscle fibers than L362del (j,k) mice that are smaller and more atrophied than nmd2J (l) at the same time-point. Scale bar in (l) represents 50μm for intercostal muscles (i-l), 200μm for diaphragm cross section (e-h) and 1340μm for whole chest cavity (a-d). Thickness of diaphragm (m) n 2-week old mice of wildtype (n=3, 198.3±9.5μm), L362del (n=3,107.1±12.1μm, p=0.0024) and 2J/2J (n=3, 118.7±28.4μm, p=0.0047) show thinner diaphragms in L362del and nmd2J compared to age-matched wildtype. (n) Analysis of muscle fiber area of intercostal muscle indicate a shift toward smaller muscle fibers in both L362del and nmd2J mutants, with L362del having the highest percentage of fibers in the smallest range, while nmd2J has the highest percentage in the small-medium area range.

0-100: Wildtype (n=3, 8.2±4.6%), L362del (n=3, 66.8±26.9%), nmd2J (n=3,38.2±14.2%).

100-200: Wildtype (n=3, 31.9±12.4%), L362del (n=3, 30.3±23.7%), nmd2J (n=3, 57.4±12.3%).

200-300: Wildtype (n=3, 11.47±4.3%), L362del (n=3, 0.2±0.2%), nmd2J (n=3, 0.2±0.4%).

300+: Wildtype (n=3, 28.2±12.9%), L362del (n=3, 0±0%), nmd2J (n=3, 0±0%).

Figure 3. NMJ and phrenic nerve morphology are not changed in L362del mutant mice at 2 or 3 weeks.
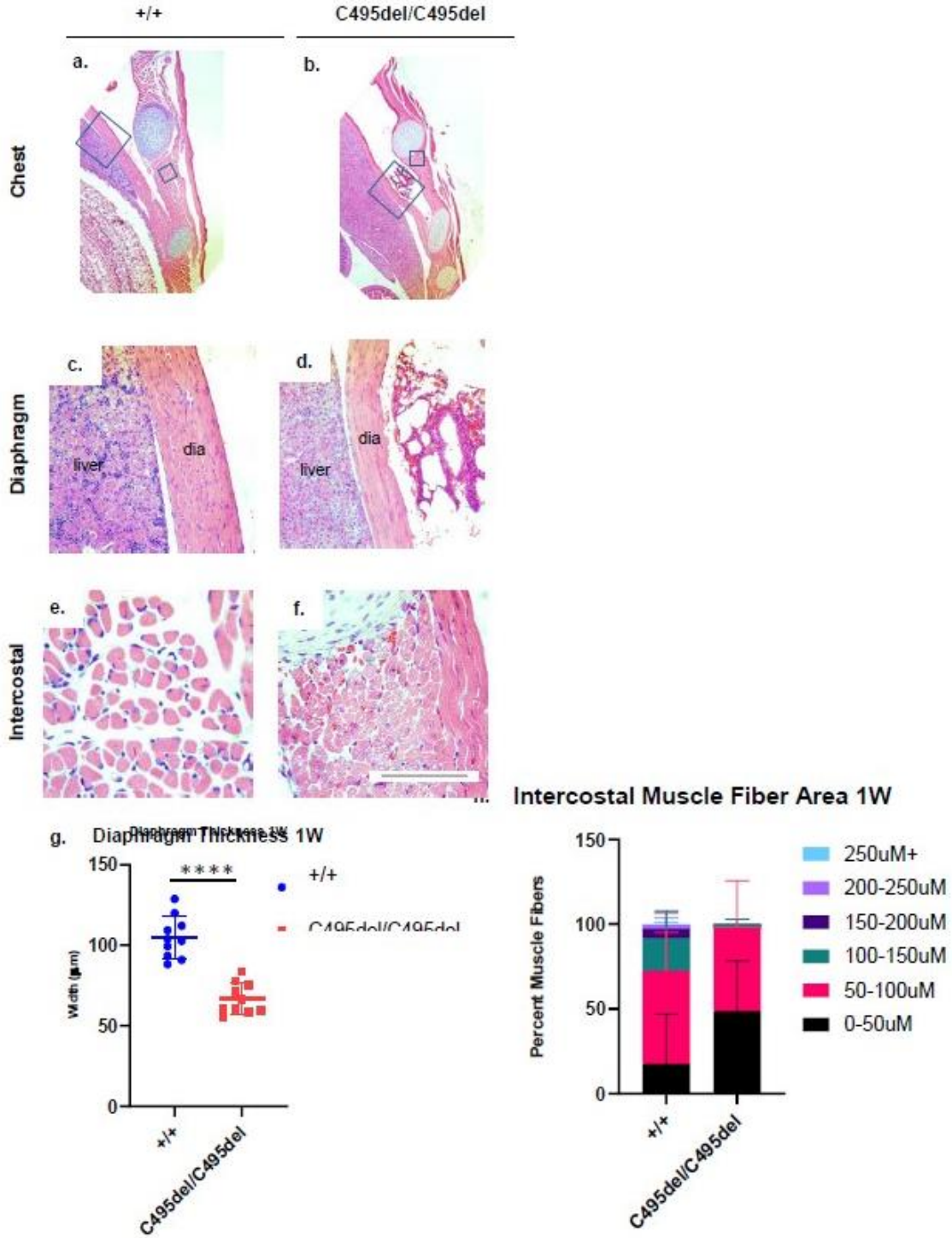
Figure 3. NMJ and phrenic nerve morphology are not changed in L362del mutant mice at 2 or 3 weeks. Representative images of diaphragmatic NMJs from the left dorsal region in wildtype (a) and L362del mutant (b) at 2 weeks of age. Scale bar for (a,b) is 50µm. (c) Analysis of NMJ occupancy in 2W wildtype, heterozygous and mutant L362del mice shows no difference in occupancy at the neuromuscular junction throughout the diaphragm. Dissection and assessment of myelinated axon counts in L362del mutant and wildtype mice show that at both two and three weeks right phrenic wildtype nerves (d,f) are comparable in size and morphology to L362del mutant (e,g). (h) Quantification of the left and right phrenic nerve show no significant myelinated axon count between the wildtype (2W Left: n=3, 253±16.6 ; 3W Left: n=3, 251±5.7; 2W Right: n=3, 264.6±22.9; 3W Right: n=4, 258.7±10.8) and L362del mutant mice (2W Left: n=6, 252.3±7.8 ; 3W Left: n=6, 243.2±8.3 ; 2W Right: n=, 262.7±8.24; 3W Right: n=4, 237.7±13.94) at either 2 or 3 weeks of age. (i) Analysis of the axonal area in the right phrenic nerve at 2 and 3 weeks shows no significant difference between wildtype and L362del mutants.0-100: Wildtype (n=3, 8.2±4.6%), L362del (n=3, 66.8±26.9%), nmd2J (n=3,38.2±14.2%).

100-200: Wildtype (n=3, 31.9±12.4%), L362del (n=3, 30.3±23.7%), nmd2J (n=3, 57.4±12.3%).

200-300: Wildtype (n=3, 11.47±4.3%), L362del (n=3, 0.2±0.2%), nmd2J (n=3, 0.2±0.4%).

300+: Wildtype (n=3, 28.2±12.9%), L362del (n=3, 0±0%), nmd2J (n=3, 0±0%).

Cross sections of whole chest from wildtype and mutant mice at 2 weeks showed that both *nmd*[2J] *and* IGHMBP2[L362del] mutants have thinner diaphragms than wildtype (**Figure 2d-f, k**). Assessment of intercostal muscle fiber areas show that both IGHMBP2[L362del] and *nmd*[2J] had a higher percentage of smaller fiber areas (**Figure 2g-i, j**). IGHMBP2[L362del] mutants display a higher percentage of the smallest muscle fibers (0-100µm^2) compared to *nmd*[2J], suggesting more overall intercostal atrophy in the IGHMBP2[L362del] model. Assessment of the intercostals and diaphragm of IGHMBP2[C495del] mutant mice compared to wildtype mice at 1 week of age also show atrophied intercostal muscles and thinner diaphragms (**Figure 3a-h**). When adjusted for weight by comparing p7 old IGHMBP2[C495del] mutants with p1 old wildtype pups, the intercostal muscles are still more atrophied and the diaphragm is still thinner. (**Supplementary Figure 1a,b).** This suggests both a potential developmental and progressive wasting of the muscles in both mutants.

To determine if muscle morphological differences were neurogenic, we performed neuromuscular junction (NMJ) staining of the diaphragms. We crossed the IGHMBP2^{L362del} heterozygous mice to mice expressing YFP under the Thy1 promoter (Thy1-YFP16), allowing us to observe the nerves and pre-synaptic terminals with the transgenically expressed YFP. We used a fluorescently conjugated α-bungarotoxin, an acetylcholine receptor antagonist, to observe the post-synaptic terminals. Quantification of the NMJ innervation in the IGHMBP2^{L362del} mutants indicate that the diaphragm does not have denervation, as previously observed in the *nmd^{2J}* model (Grohmann et al., 2004, Villalón et al., 2018) (**Figure 4a-c**). The IGHMBP2^{L362del} mutant morphology of individual synapses appear to be normal, similar in size and innervation to wildtype littermates (**Figure 4a-c**). However, for IGHMBP2^{C495del} mutants at 1 week of age compared with wildtype mice at 1 week of age, significant partial denervation is seen in the diaphragm **(Figure 4d-f).**

Figure 4. NMJs in the diaphragms of L362del and C495del mice.
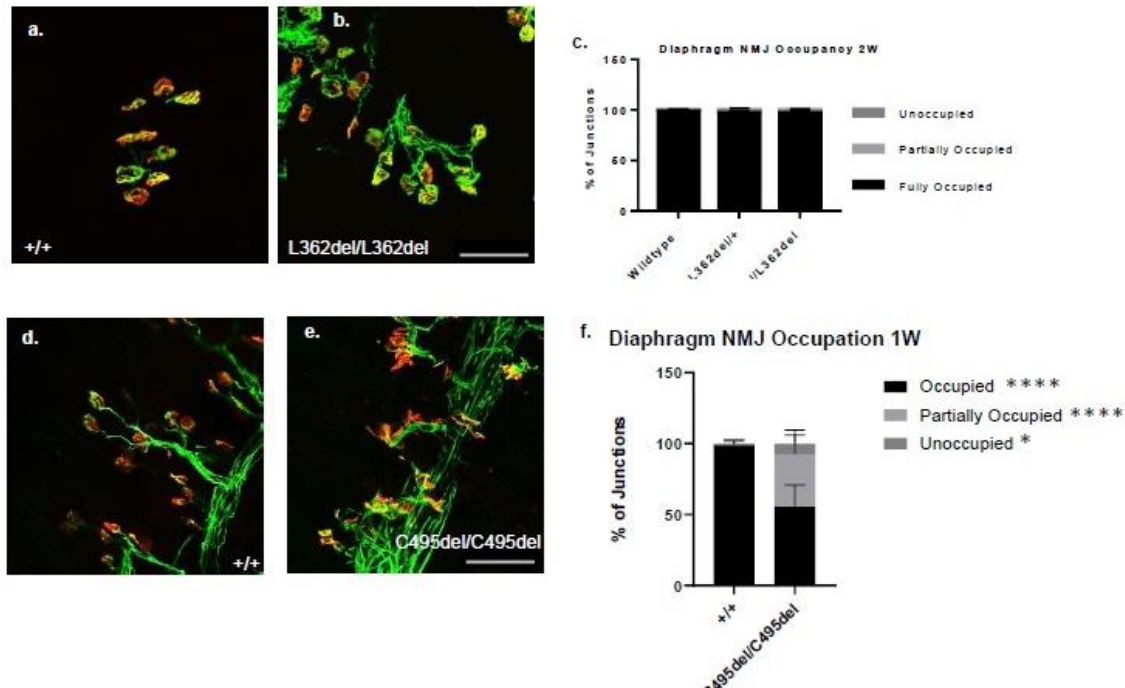
Figure 4. NMJs in the diaphragms of L362del and C495del mice. Representative images of diaphragmatic NMJ from the left dorsal region of the phrenic nerve in +/+ (a) and L362del mutant (b) at 2 weeks of age. Scale bar for (a,b,d,e) is 50μm. (c) Analysis of NMJ occupancy in 2W +/+, heterozygous and mutant L362del mice shows no difference in occupancy at the neuromuscular junction throughout the diaphragm. Representative images of diaphragmatic NMJ from the left dorsal region of the phrenic nerve in +/+ (d) and C495del mutant (e) at 1 week of age. (f) Analysis of NMJ occupancy in one-week old +/+ and C495del mutant mice shows no difference in occupancy at the neuromuscular junction throughout the diaphragm.

Because the diaphragm of IGHMBP2[L362del] mutants do not have clear morphologic NMJ deficits while IGHMBP2[C495del] mutants do, we assessed cross-sections of the phrenic nerve which innervates the diaphragm, as changes in overall myelinated axon count, axon diameter, or myelination may alter diaphragmatic function. For IGHMBP2[L362del] mutants at both 2 and 3 weeks of age there is no change in the overall myelinated axon count or diameter for either the right or the left phrenic nerve in the IGHMBP2[L362del] mutant compared to the wildtype (**Figure 5a-f**).

The phrenic nerves of IGHMBP2[C495del] mutants at one week of also do not show a reduction in axon counts or caliber (**Figure 5g-i).** However, overall nerve size is smaller in IGHMBP2[C495del] mutants and

myelin sheath thickness is thinner in IGHMBP2^{C495del} mutants suggesting possible myelination or perhaps

developmental defects **(Figure 5j,k).**

Figure 5. Phrenic nerve morphology in L362del and C495del mice.
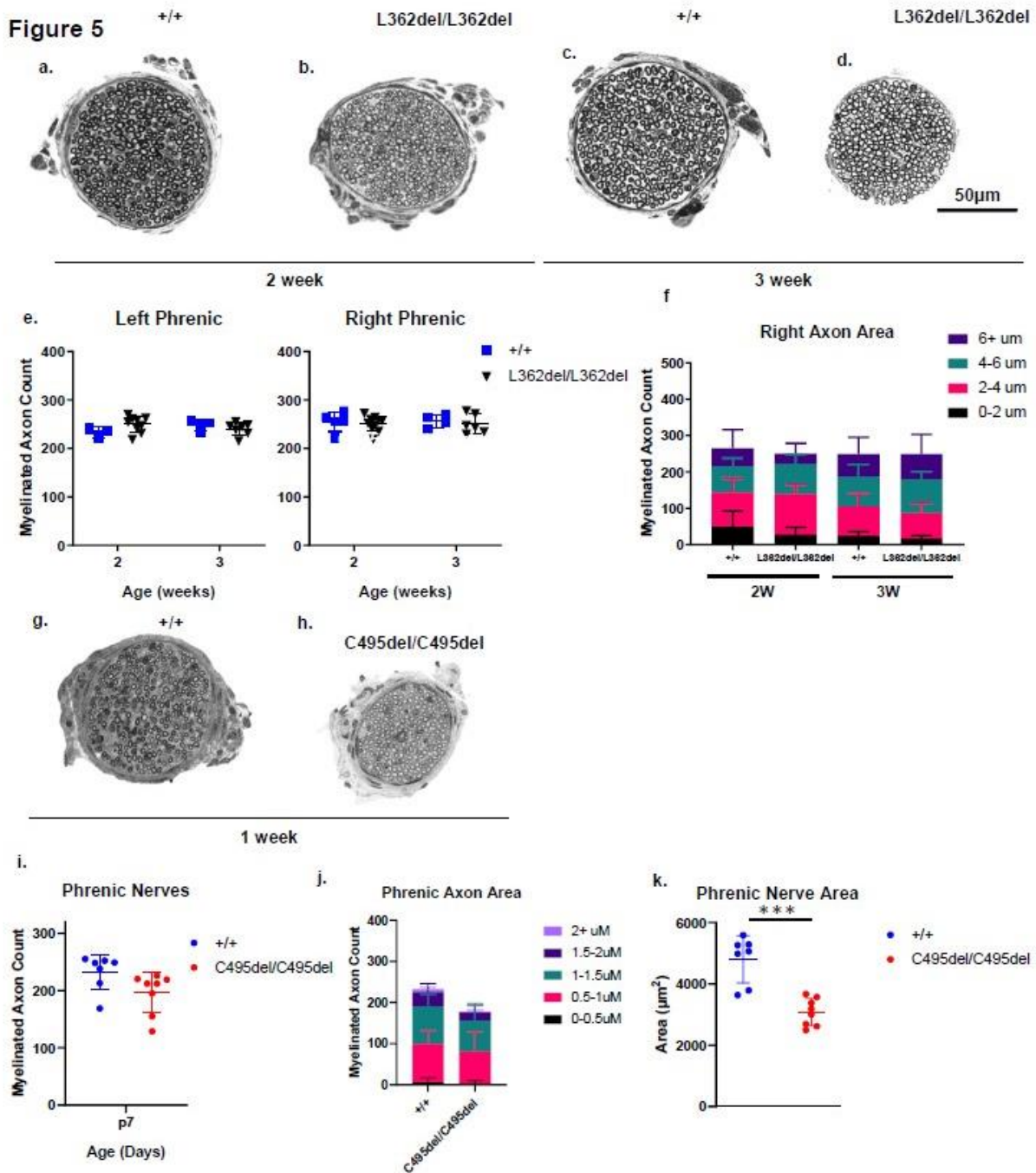
Figure 5. Phrenic nerve morphology in L362del and C495del mice. Dissection and assessment of myelinated axon counts in L362del mutant and +/+ mice show that at both two and three weeks right phrenic +/+ nerves (a,b) are comparable in size and morphology to L362del mutant (c,d). (e) Quantification of the left and right phrenic nerve show no significant myelinated axon count between the +/+ (2W Left: n=3, 253±16.6 ; 3W Left: n=3, 251±5.7; 2W Right: n=3, 264.6±22.9; 3W Right: n=4, 258.7±10.8) and L362del mutant mice (2W Left: n=6, 252.3±7.8 ; 3W Left: n=6, 243.2±8.3 ; 2W Right: n=, 262.7±8.24; 3W Right: n=4, 237.7±13.94) at either 2 or 3 weeks of age. (f) Analysis of the axonal area in the right phrenic nerve at 2 and 3 weeks shows no significant difference between +/+ and L362del mutants. Dissection and assessment of myelinated axon counts in C495del/C495del and +/+ mice show that at 1 week the phrenic nerves (g) are significantly different in size and morphology to the C495del mutant (h). (i) Quantification of the phrenic nerves (both left and right) do not show a significant myelinated axon count between the +/+ (n=7, 232±31.2) and C495del mutant mice (n=8, 196±35.2) at 1 week of age. (j) Analysis of the axonal area in the phrenic nerves at 1 week of age does not show a significant difference between +/+ and C495del mutants. (k) Analysis of the overall area in the phrenic nerves at 1 week of age does show a significant difference between +/+ and C495del/C495del.

2.2.4 IGHMBP2^{L362del} and IGHMBP2^{C495del} mutant mice display irregular breath rates

To detect if these neuronal and muscular defects cause respiratory distress in the IGHMBP2^{L362del} mutants and IGHMBP2^{C495del} mutants respectively, we utilized the PiezoSleep system. Both IGHMBP2^{L362del} mutants and IGHMBP2^{C495del} mutants show significant lower breath rates than wildtype mice at both p4 and p7 with a failure to increase their breath rate between timepoints unlike wildtype mice. Despite the IGHMBP2^{C495del} mutant mice more severe and neurogenic phenotype, there is not a significant difference in breath rate between IGHMBP2^{L362del} mutants and IGHMBP2^{C495del} mice **(Figure 6a)**. They both show qualitative signs of respiratory distress with occasional "sawtooth" waveforms and "couplets", suggesting an irregularity in diaphragmatic activation with potentially one side of the diaphragm contracting slightly before the other and/or a hiccupping phenotype **(Figure 6b)**.

Figure 6. L362del and C495del show signs of respiratory distress.
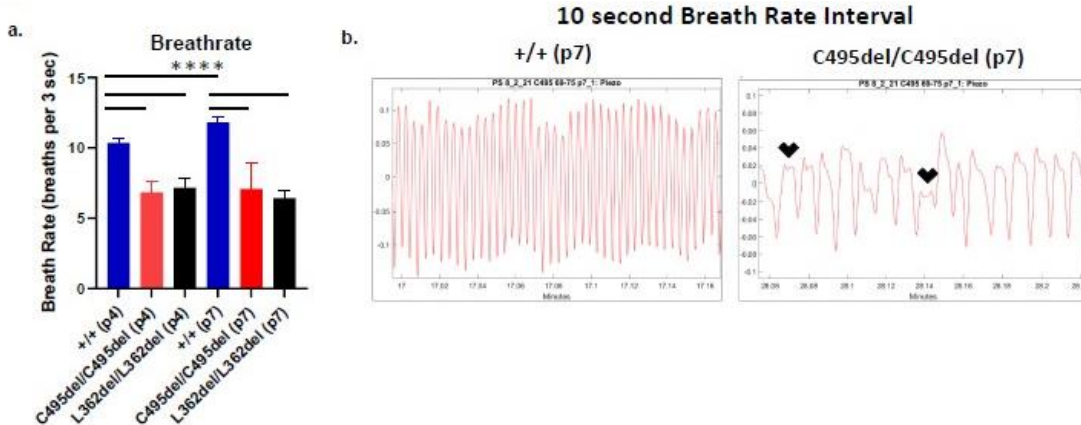
Figure 6. L362del and C495del show signs of respiratory distress. (a)L362del and C495del mutants have a lower breath rate than +/+ at p4 and p7 (all p<0.0001, ****). (b) Example of +/+ and C495del/C495del breathing pattern at p7 with +/+ having more rhythmic breathing compared to the "doublets" (indicated by black arrows) of the C495del/C495del.

2.2.5 IGHMBP2^{L362del} and IGHMBP2^{C495del} mutant mice display significant distal axonal degeneration

IGHMBP2^{L362del} exhibit overt changes in size and motor function by one to one and a half weeks, earlier than *nmd^{2J}*. To determine to what degree this motor deficit is driven by lower limb muscular atrophy, we assessed two lower hindlimb muscles from whole hindlimb cross-sections (**Figure 7a-c**): the medial gastrocnemius (MG), a fast-twitch muscle, (**Figure 7d-g**), and soleus (Sol) a slow-twitch muscle, (**Figure 7h-k**). When comparing the muscle fiber morphology and areas between wildtype, IGHMBP2^{L362del} mutants, and *nmd^{2J}* mutants at the two-week time point, the IGHMBP2^{L362del} mutants have smaller fiber size than *nmd^{2J}* mutants and wildtype siblings for both MG and Sol (**Figure 7g,k**). The MG and Sol of IGHMBP2^{C495del} mutant mice at one week of age have smaller muscle fibers compared to wildtypes at

one week of age **(Figure 7l-s).** Interestingly, no significant increases in central nuclei were seen in

IGHMBP2^{L362del} or IGHMBP2^{C495del} mutants.

Figure 7. L362del and C495del mutations cause muscular atrophy.
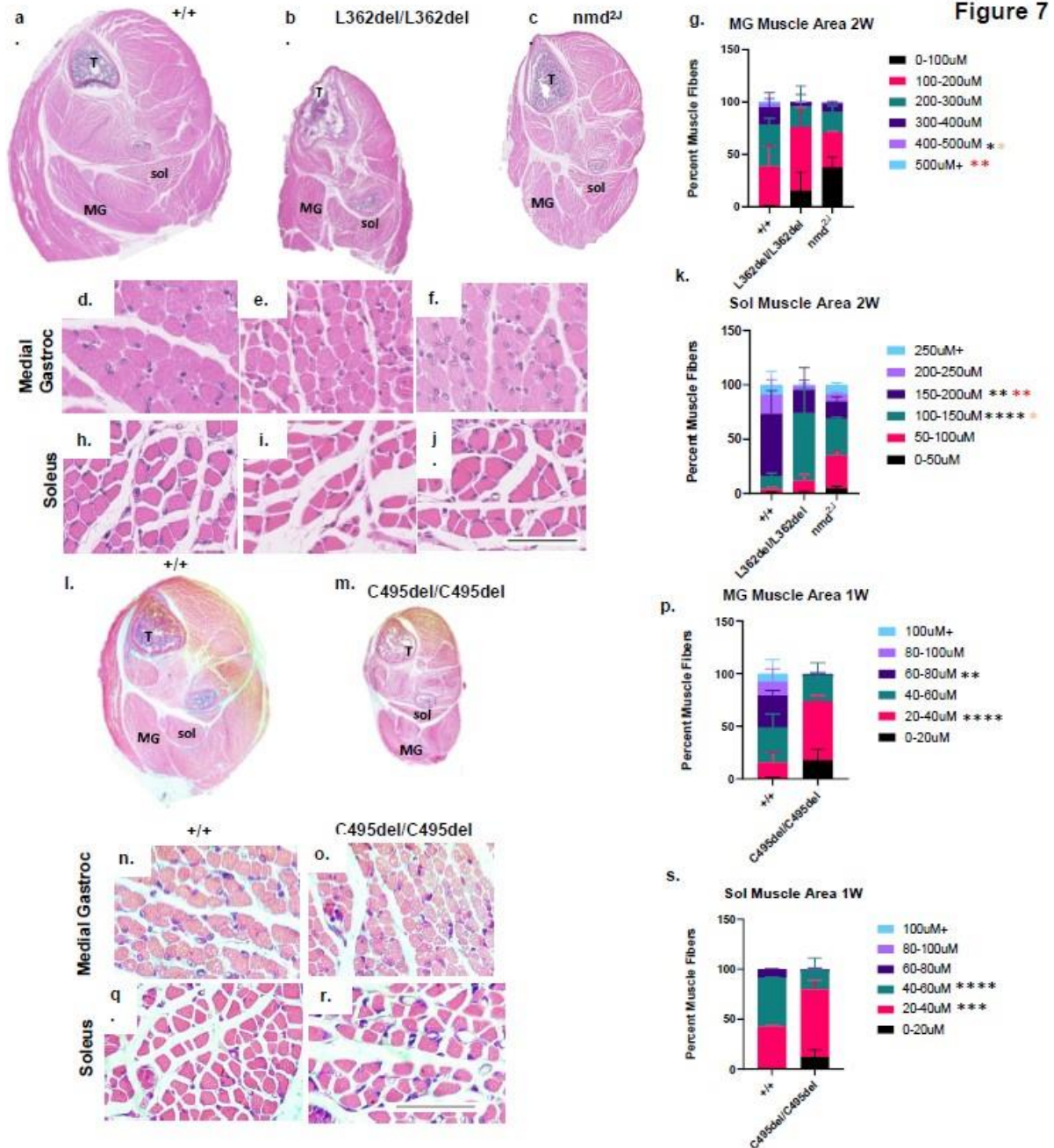
Figure 7. L362del and C495del mutations cause muscular atrophy. Histological analysis of hindlimb (hematoxillin-eosin staining). 14-day old +/+ (a), L362del/L362del (b), and nmd2J (c). L362del mutant is smaller overall compared to nmd2J and +/+. Images of medial gastrocnemius (MG) show larger fiber sizes in 14-day old +/+ (d) compared to reduced fiber size in both L362del mutant (e) and nmd2J (f). Analysis of MG muscle fiber (g) area (μm2) comparing +/+ (n=3), L362del mutant (n=6) and nmd2J (n=2). (Black asterisk, +/+ vs. L362del/L362del) (*100-200; p=0.02532), (Red asterisk, +/+ vs. nmd2J) (**0-100; p=0.0042), (Orange asterisk, L362del/L362del vs. nmd2J) (*100-200; p=0.0192). Two-way ANOVA, with post-hoc Tukey. Images of soleus a slow twitch muscle show fiber sizes in 14-day old +/+ (h) are more comparable n size to L362del mutant(i) and 2J(j). Scale bar is 800μm for whole hindlimb (a-c) and 50μm for MG and Soleus muscle image (d-j). (k) Analysis of soleus muscle fiber area (um2) comparing +/+ (n=3), em3/em3 (n=6) and 2J (n=2). (Black asterisk, +/+ vs. L362del/L362del) (****100-150; p<0.0001, **150-200; p=0.0022), (Red asterisk, +/+ vs. nmd2J) (**150-200; p=0.0023, (Orange asterisk, L362del/L362del vs. nmd2J)m (*100-150; p=0.0194). Two-way ANOVA, with post-hoc Tukey. 7-day old +/+ (l) and C495del/C495del (m). C495del/C495del is smaller overall compared to +/+. Images of medial gastrocnemius (MG) show larger fiber sizes in 7-day old +/+ (n) compared to reduced fiber size in C495del/C495del (o). Analysis of MG muscle fiber (p) area (μm2) comparing +/+ (n=3), C495del/C495del (n=3). (Black asterisk, +/+ vs. C495del/C495del) (****20-40; p<0.0001, **60-80; p=0.0018). Two-way ANOVA, with post-hoc Tukey. Images of soleus a slow twitch muscle show fiber sizes in 7-day old +/+ (q) are more comparable in size to C495del mutant(r). Scale bar is 800μm for whole hindlimb (l,m) and 50μm for MG and Soleus muscle image (n,o,q,r). (s) Analysis of soleus muscle fiber area (um2) comparing +/+ (n=2) and C495del/C495del (n=4). (Black asterisk, +/+ vs. C495del/C495del) (***20-40; p=0.0002, ****40-60; p<0.0001)

To determine if the reduced muscle fiber size is neurogenic in nature, NMJs from both muscles were assessed. IGHMBP2[L362del] mutants display significantly more denervation of the NMJs in both the MG and the Sol at 2 weeks compared to wildtype (**Figure 8a-f**). Also, at one week of age, notable NMJ denervation is also observed in IGHMBP2[C495del] mutants in both muscles compared to wildtype animals **(Figure 8g-l).** This indicates that denervation likely plays a role in the reduced muscle fiber size seen in both mutants.

Figure 8. L362del and C495del mutations cause loss of neuromuscular junctions.
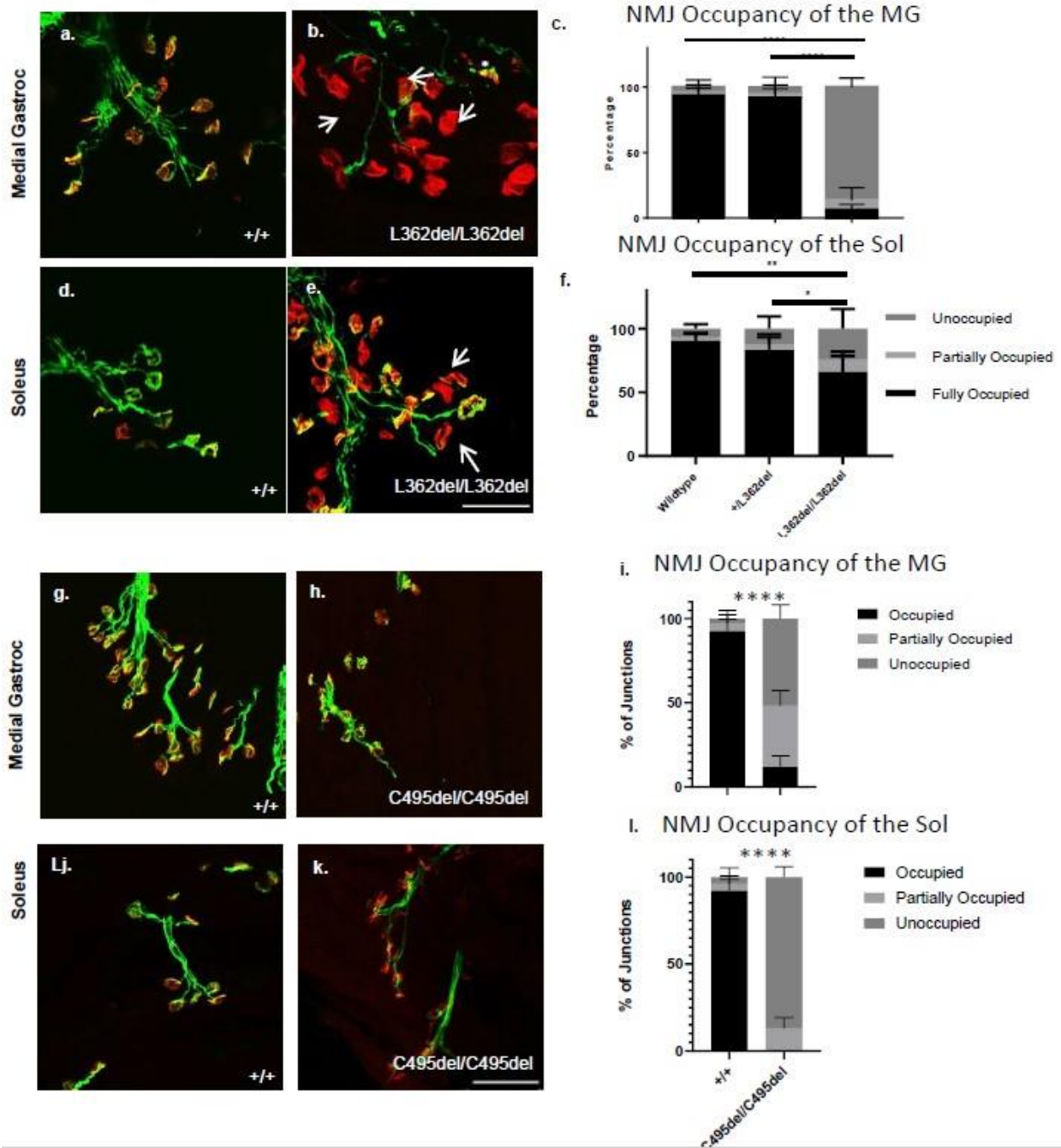
Figure 8. L362del and C495del mutations cause loss of neuromuscular junctions. Neuromuscular junction (NMJ) staining of MG muscle. 2-week old +/+ (a) and L362del/L362del (b). Tissues were stained for pre-synaptic vesicles(ant-SV2, green), neurofilaments (anti-neurofilament 2Hs, green) and acetylecholine receptors (a-bungarotoxin, red). Unoccupied (arrow) and partially occupied (asterisk) are highlighted. Scale bar, 50µm. (c) Occupancy of NMJs of MG muscle. Quantification of fully innervated, partially innervated and denervated junctions based on pre- and post-synaptic staining overlap. 2-week old +/+, heterozygous and mutant L362del mice (n=7, 16, and 6 respectively). Mutant L362del have significantly higher percentage of denervated NMJs (86.4±6.9%) compared to +/+ (4.0±5.4%, p<0.0001) or heterozygous mice (5.2±7.7%, p<0.0001). NMJs of soleus muscle in +/+ (d) compared to L362del (e). (f)Quantification of junction innervation of 2-week old +/+, heterozygous and mutant L362del mice (n=7, 14, and 6 respectively), showed that L362del mutants (24±15.5%) had significantly higher percentage of unoccupied junctions than +/+ (6.5±3.5%, p=0.003) or heterozygous (12.1±9.5%, p=0.02). Neuromuscular junction (NMJ) staining of MG muscle in 1-week old +/+ (g) and C495del/C495del (h). Tissues were stained for pre-synaptic vesicles (ant-SV2, green), neurofilaments (anti-neurofilament 2Hs, green) and acetylecholine receptors (a-bungarotoxin, red). Unoccupied (arrow) and partially occupied (asterisk) are highlighted. Scale bar, 50µm. (i) Occupancy of NMJs of MG muscle. Quantification of fully innervated, partially innervated and denervated junctions based on pre- and post-synaptic staining overlap. 1-week old +/+ and C495del/C495del mice (n=20 and n=12 respectively). C495del/C495del have significantly higher percentage of denervated NMJs (86.4±6.9%) compared to +/+ (4.0±5.4%, p<0.0001). NMJs of soleus muscle in +/+ (j) compared to C495del/C495del (k). (l) Quantification of junction innervation of 1-week old +/+ and C49del/C495del mice (n= 3 and 3 respectively), showed that C495del/C495del mice (24±15.5%) had significantly higher percentage of unoccupied junctions than +/+ (6.5±3.5%,

To further assess the extent of the degeneration, we assessed the more proximal femoral motor and sensory nerve branches. These were harvested from IGHMBP2[L362del] mutants, nmd2J mutants, and wildtype siblings at 2 weeks and IGHMBP2[C495del] mutants and their wildtype siblings at 1 week of age. Degeneration of the motor branch leaves the IGHMBP2[L362del] mutant mice with fewer myelinated axons than the wildtype littermates at 2 weeks old (**Figure 9a-c,k**). The sensory axons also have reduced numbers in the IGHMBP2[L362del] mutants, but no difference is observed in myelinated sensory axons of 2 week-old *nmd[2J]* compared to their wildtype littermates (**Figure 9f-h,k**). In IGHMBP2[C495del] mutants, the axon number of motor and sensory nerves are highly significantly impacted as well at 1 week-old compared to wildtype (**Figure 9d,e,i-k).**

27

Figure 9. L362del and C495del mutants exhibited increased peripheral motor and sensory axonal degeneration than nmd2J at 2 and 1 weeks of age.
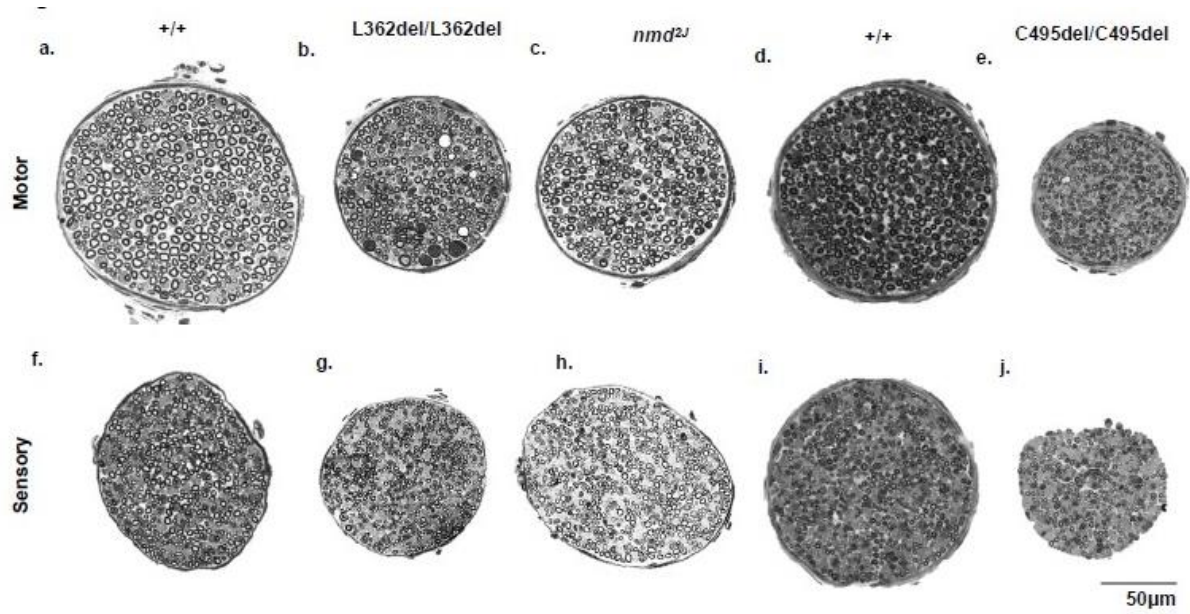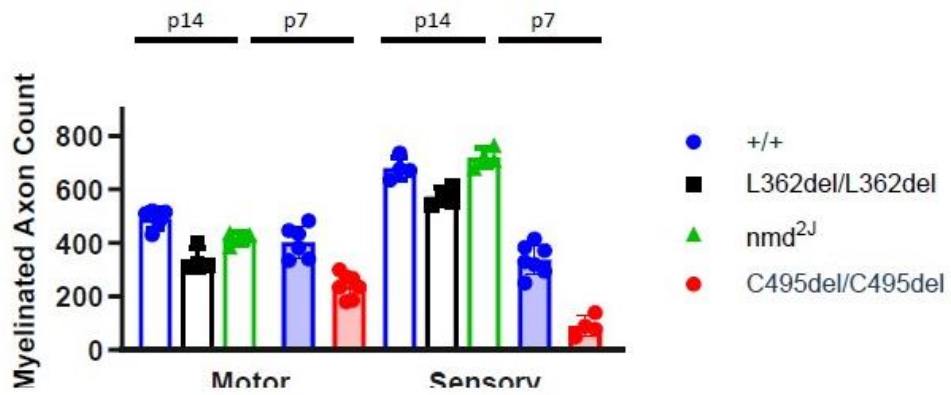
Figure 9. L362del and C495del mutants exhibited increased peripheral motor and sensory axonal degeneration than nmd2J at 2 and 1 weeks of age. Representative images of femoral motor branch nerve cross sections of p14 +/+ (a), L362del/L362del (b), and nmd2J (c), as well as femoral sensory branch nerve (f-h). Representative images of femoral motor branch nerve cross sections of p7 +/+ (d), C495del/C495del (b) as well as femoral sensory branch nerve (e,f). (k) Femoral motor myelinated axon counts for p14 L362del/L362del (n=4, 335.1±42.89) are significantly reduced (p=0.0002) compared to littermate +/+ (n=5, 490.5±37.94) , while nmd2J (n=4, 416.6±22.6) also show a reduction (p=0.0289)compared to +/+ it is less significant that L362del/L362del (p=0.0228). Comparison of myelinated axon counts for sensory found that L362del/L362 (n=4, 574±31.72) were again significantly reduced compared to both +/+ (n=4, 679.5±41.68, P=0.0070)and nmd2J (n=4, 718.4±35.73, P=0.0009), while nmd2J shows no difference compared to +/+ (p=0.335). Figure 10. C495del mutants exhibited increased peripheral motor and sensory axonal degeneration than +/+ at 1 week of age. (k) Femoral motor myelinated axon counts for p7 +/+ (n=6, 403.2±60.98) and C495del/C495del (n=7, 239.4±44.59) are significantly reduced (p=0.0002). Comparison of myelinated axon counts for sensory found that C495del mutants (n=4, 88.5±37.61) were again significantly reduced compared to both +/+ (n=8, 326.5±60.24, P<0.0001). (k) p7 C495del femoral motor axon counts are also significantly lower than p14 L362del (p=0.0428) and p14 nmd2J (p<0.0001). p7 C495del femoral sensory axon counts are also significantly lower than p14 L362del (p<0.0001).) and p14 nmd2J (p<0.0001). There is no significant difference between p14 and p7 +/+ femoral motor myelinated axon counts, but there is a significant difference between p14 and p7 +/+ femoral sensory myelinated axon counts (p<0.0001). This is likely due to the process of myelination during neonatal stages with more nerves becoming myelinated as the mice age.

2.2.6 Neonatal lethality in IGHMBP2 null mice

In the process of CRISPR-Cas9 mutagenesis targeting the IGHMBP2^{L362del} allele, non-homologous end joining (NHEJ) produced a large insertion and deletion founder. This mouse, *Ighmbp2^{em4}*(IGHMBP2-null) resulted in a pre-mature termination of IGHMBP2. Immunoblot analysis of the brain lysates showed that no full-length ~110kD IGHMBP2 protein was detected (**Figure 10a**). No *Ighmbp2* null mice are observed when checking the litters at 3 weeks of age in 7 litters of mice (**Figure 10b**, **Supplementary Table 1**). By checking for pups on the day of birth, using timed matings, the median lifespan of the *Ighmbp2^{null}* allele is found to be around 6-10 hours, with no homozygous mutant pups making it to an age older than one day (**Figure 10b**). Some neonates in the litters appeared cyanotic and died within a few hours of birth, while others were stillborn, or even born *en caul*. Preliminary characterization of this model indicates that at birth these mice are indistinguishable from their siblings in size and are not paralyzed (**Figure**

10c,d). Size similarities between mutants and siblings, as well as the motor functionality, suggested that

no gross developmental defects causing embryonic lethality are present. Confirmation with MicroCT

comparison of E18.5 wildtype and mutant null littermates also show no gross anatomical differences,

such as diaphragm hernia, cleft palate, or other developmental abnormalities that may be cause of

neonatal death (**Figure 10e**). Analysis of mRNA expression of *Ighmbp2* indicates no impact to the mRNA

levels in spinal cord extract of the null mutant mice (**Figure 10f**). Assessment of primarily motor neuron

genes, *ChAT* and *Chodl,* demonstrated that there were no expression changes detected either,

suggesting that there was no gross loss of motor neurons in the spinal cord (**Figure 10f**). The exact

cause of death is currently undetermined for this *Ighmbp2* null allele, but it is a valuable tool in

understanding the differences between reduced function and reduced levels of IGHMBP2 in *Ighmbp2-*

related diseases.

Figure 10. IGHMBP2 null mouse has decreased lifespan and normal body size.
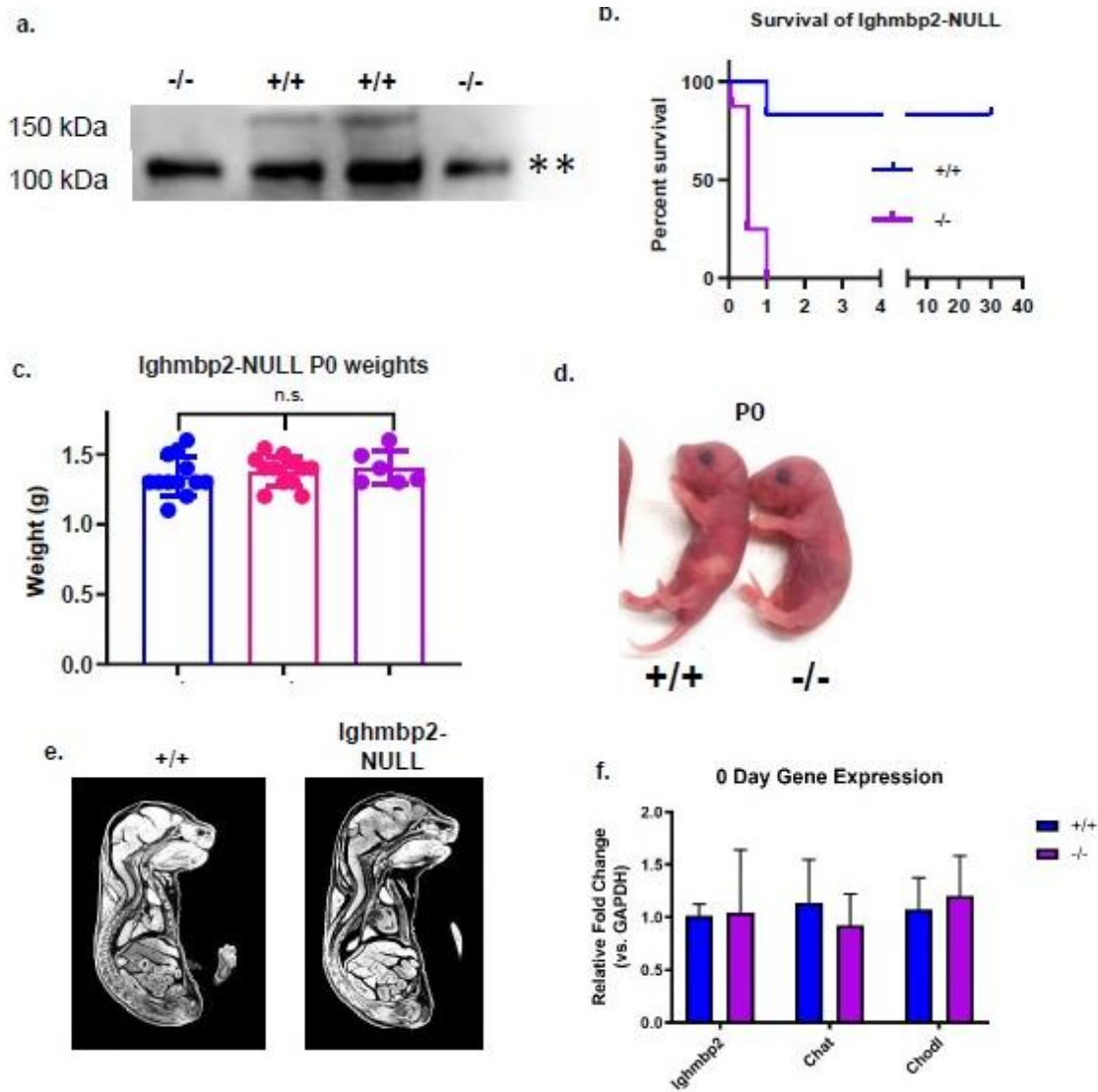
Figure 10. IGHMBP2 null mouse has decreased lifespan and normal body size. (a) Novel Ighmbp2 variant caused by an insertion and deletion through CRISPR-cas9 non-homologous end joining (c.1071_1083delinsGGTGGTGGTGGACTACTTTTT; p.357Asp>GlufsX383), nucleotide insertion highlighted in red with amino acid change below. (b) Mice homozygous for early termination (Ighmbp2em4/em4) have a significantly reduced lifespan (n=8; median lifespan 0.5days compared to +/+ littermates (n=18). Log-rank (Mantel-Cox) p<0.0001.(****). (c) However, mutant body size at birth (n=6, 1.4±0.1221g) was comparable to +/+ (n=12, 1.344±0.1413g) and heterozygous (n=12, 1.38±0.1084g) littermates. One-way ANOVA with Post-hoc tukey shows nosignificant differences between weights. (d) Null mice (em4/em4 mutants) were overtly normal and at E18.5 had no notable groos morphological defects when observed by MicroCT (e). (f) The P0 spinal cord gene expression in em4/em4 mutant and +/+ littermates shows no significant change in Ighmbp2, Chat, or Chodl , while immunoblot analysis (g) of whole brain lysate at P0 in em4/em4 and +/+ littermates shows no expression of full length IGHMBP2 in the em4/em4 mutants.

2.3 Discussion

Here we identified and characterized three new models with severe SMARD1-like phenotypes. The IGHMBP2[L362del] mutant mice demonstrate clear distal motor and sensory neuropathy defects with denervation pathology in the hindlimb muscles, leading to significant neurogenic muscular atrophy before 3 weeks of age. The *Ighmbp2*-null mice demonstrate that the gene is critical for viability, and show neo-natal lethality. The IGHMBP2[C495del] mice demonstrate a severe phenotype in between that of the IGHMBP2[L362del] and *Ighmbp2*-null mice. Our models expand the spectrum to better reflect the clinical spectrum observed in patients with various *IGHMBP2* recessive alleles. Not only can these models be used to determine the mechanism of *Ighmbp2*-associated diseases, but to assess future therapeutics in pre-clinical trials.

The *Ighmbp2*-null mice, like many of the most severe human patients, often appear overtly healthy immediately following birth, but quickly decline resulting in neo-natal lethality. Micro-CT assessment of our mice at E18.5 (**Figure 10e**) indicated that there were no gross morphological differences that may be contributing to early sudden death between IGHMBP2-null and wildtype littermates at this time point.

It is plausible that respiratory distress is arising in patients and mouse models even in the absence of observable neurological pathology due to functional deficits and not anatomy. The direct innervation status of the diaphragm or the phrenic nerve has not been assessed in human patients, as this would need to be assessed post-mortem. Recent work looking at the onset and progression in a number of SMARD1 patients found that onset of respiratory symptoms precede the onset of a diagnosable phrenic palsy by about one month, however respiratory interventions are taken with patients that cannot be taken with our mouse models[5]. Our findings in the null mouse model, as well as cases previously reported would suggest that *IGHMBP2* should be considered a candidate gene for SIDS cases.

Both IGHMBP2^{L362del} and IGHMBP2^{C495del} models show marked respiratory distress and significant muscle atrophy of key respiratory muscles and neurogenic defects. Morphological assessment of NMJ occupancy, phrenic nerve axon count, the critical respiratory muscles, diaphragm and intercostal, along with the breath rate assessment of the PiezoSleep system show an early onset of this respiratory distress phenotype. We argue that the earlier presentation of the muscular atrophy in respiratory muscles of the IGHMBP2^{L362del} model may be contributing to a respiratory distress phenotype, not previously observed in the less-severe *nmd^{2J}* model. Neurogenic atrophy of the hindlimb muscles and degeneration of distal motor and sensory axons are more pronounced at an earlier time-point than in the IGHMBP2^{L362del} and IGHMBP2^{C495del} models than the *nmd^{2J}* model (Grohmann et al., 2001, Villalón et al., 2018).

The creation and characterization of these novel mouse models will further expand the spectrum of available severe SMARD1-like mice leading to a better understanding of the importance of IGHMBP2 in neuronal survival, neonate respiratory distress, and the different pathomechanisms associated with various IGHMBP2 mutations. It will be important to understand the mechanisms involved with a reduction or lack of IGHMBP2 protein, as is the case with the *nmd^{2J}* and *Ighmbp2*-null mice, and models with hypomorphic IGHMBP2 protein, such as IGHMBP2^{L362del} and IGHMBP2^{C495del} models. A key difference in mechanisms to study between the IGHMBP2^{L362del} and IGHMBP2^{C495del} models are the IGHMBP2^{C495del}'s failure to thrive, gaining in no weight in it's ~7 day lifespan, and IGHMBP2^{C495del}'s phrenic phenotype. Understanding the role of IGHMBP2 in disease and development particularly the maintenance of the motor neuron and respiratory system will be vital for future therapeutics and diagnoses.

CHAPTER 3

Characterizing the Less Severe Side of the Spectrum of Disease associated with IGHMBP2

Clinically relevant mouse models of Charcot-Marie-Tooth Type 2S

Paige B. Martin[1,+], Sarah E. Holbrook[1,2,+], Amy N. Hicks[1], Timothy J. Hines[1], Laurent P. Bogdanik[1], Robert W. Burgess[1], *Gregory A. Cox[1],

1. The Jackson Laboratory, Bar Harbor, ME, USA

2. The University of Maine, Orono, ME, USA

+These authors contributed equally to the manuscript

Abstract

Charcot-Marie-Tooth disease is an inherited peripheral neuropathy that is clinically and genetically heterogenous. Mutations in *IGHMBP2*, a ubiquitously expressed DNA/RNA helicase, have been shown to cause the infantile motor neuron disease spinal muscular atrophy with respiratory distress type 1 (SMARD1), and, more recently, juvenile-onset Charcot-Marie-Tooth disease Type 2S (CMT2S). Using CRISPR-*cas9* mutagenesis we developed the first mouse models of CMT2S (p.Glu365del (E365del) and p.Tyr918Cys (Y918C)). E365del is the first-ever CMT2S mouse model and Y918C is the first human CMT2S allele knock-in model. Phenotypic characterization of the homozygous models found progressive peripheral motor and sensory axonal degeneration. Neuromuscular and locomotor assays indicate that both E365del and Y918C mice have motor deficits, while neurobehavioral characterization of sensory function found that E365del mutants have mechanical allodynia. Analysis of femoral motor and sensory nerves identified axonal degeneration, which does not impact nerve conduction velocities in E365del mice, but does in the Y918C model. Based on these results, the E365del mutant mouse, as well as the human allele knock-in, Y918C, represent mouse models with the hallmark phenotypes of CMT2S, which will be critical for understanding the pathogenic mechanisms of IGHMBP2. These mice will complement existing *Ighmbp2* alleles modeling SMARD1 to help understand the complex phenotypic and genotypic heterogeneity that is observed in patients with *IGHMBP2* variants.

3.1 Introduction

Charcot-Marie-Tooth disease (CMT) is comprised of a broad clinicogenetic spectrum of inherited peripheral neuropathies, impacting approximately 1 in 2,500 people(Skre, 1974). CMT is clinically segregated into two broad forms. Type 1 is characterized by demyelination and reduced nerve conduction velocity. Type 2 is characterized by axon loss and reduced action potential amplitudes. Additionally, there are intermediate forms which display both demyelination and axon loss. To date, over 80 genetic contributors to CMT have been identified, some of which are also known to contribute to motor neuron disease (MND) (Laurá et al., 2019; Martin et al., 2020; Timmerman et al., 2014; Yong et al., 2014). This overlap of inherited peripheral neuropathies (IPN) and MND has recently begun to be established, with genetic contributions involved in RNA metabolism, protein homeostasis, and axonal transport/maintenance being linked to both types of disease (Bennett et al., 2018; Gonzalez et al., 2014; James et al., 2006).

Variants in *IGHBMP2* have been identified in an axonal CMT, classified as CMT type 2S (Cottenie et al., 2014; Wagner, Huang, Tetreault, Majewski, Boycott, Bulman, Dyment, & McMillan, 2015). A mutation in *Ighmbp2* was first identified as the cause of the neuromuscular degeneration (*nmd*[2J]) mouse mutation (Cox et al., 1998a), and subsequently, variants in *IGHMBP2* were implicated in a severe infantile MND, spinal muscular atrophy with respiratory distress type 1 (SMARD1). IGHMBP2 is a ubiquitously-expressed DNA/RNA helicase that is putatively involved in RNA metabolism; its preferred substrate is GC-rich dsRNA, which it unwinds in a 5' to 3' direction (U. P. Guenther, Handoko, Laggerbauer, et al., 2009a). Growing evidence has shown that IGHMBP2 may also play a role in translation, as it has been found to associate with translational machinery and is predominantly located in the cytoplasm (U. P. Guenther, Handoko, Laggerbauer, et al., 2009b; Maddatu et al., 2004). Both CMT2S and SMARD1 are autosomal recessive with missense and/or truncating variants (Cottenie et al., 2014; Liu et al., 2017;

Wagner, Huang, Tetreault, Majewski, Boycott, Bulman, Dyment, McMillan, et al., 2015). While SMARD1

patients present within the first few months of life, CMT2S patients typically present after one year of

age without respiratory involvement (Cottenie et al., 2014; Liu et al., 2017; Wagner, Huang, Tetreault,

Majewski, Boycott, Bulman, Dyment, McMillan, et al., 2015).

To date, only the *nmd²ᴶ* mouse model, on both the C57BL/6J and the FVB/NJ backgrounds (Grohmann et

al., 2004; Shababi et al., 2019) and the *Ighmbp2*-D564N, on the FVB/NJ background (31), have been

described as SMARD1 models. Here we present work highlighting the generation and characterization of

the first CMT2S mouse model C57BL/6J-Ighmbp2*ᵉᵐ¹ᶜˣ*/Cx (E365del) and the first human CMT2S allele

knock-in model C57BL/6J-*Ighmbp2ᵉᵐ⁵ᶜˣ*/Cx (Y918C). Phenotypic and neurobehavioral assessment

indicates that the mice display progressive sensory and motor function deficits and axon degeneration.

These mice provide a critical resource for future pathomechanistic and pre-clinical validation work.

3.2 Results

3.2.1 CRISPR-*cas9* Induced *Ighmbp2*-E365del Mutation and Human Knock-in Allele *Ighmbp2*-Y918C

During the course of a CRISPR-*cas9* mutagenesis project to produce new alleles of *Ighmbp2* in mice, a

founder carrying a novel deletion in exon 8 (c.1093_1095del; p.Glu365del), within the helicase domain

of *Ighmbp2*, was identified (**Figure 11a**). This variant is predicted to delete a single amino acid while

maintaining the reading frame, but does not significantly impact transcript levels of *Ighmbp2* (**Figure

11b**).

3.2.2 *Ighmbp2*-E365del homozygous mice have functional sensory and motor deficits.

Initial characterization of the homozygous E365del mutants found that mice presented as thin, wasted,

and with paresis of the hind quarters, first notable by 2-3 months of age, and progressing over time

(**Figure 11c**). While the mice have an overt hindlimb muscular atrophy, this does not impact their overall

survival (**Figure 11d**), but does result in reduced body weight over time in the mutant mice (**Figure 11e,f**). Extensive characterization of E365del homozygous mutants indicated progressive muscular wasting and motor deficits, similar to *IGHMBP2*-associated CMT2S patients (Vadla et al., 2023, Guenther et al., 2009, Scheiper et al., 2018, Shababi et al., 2018). To validate the E365del mutant as a CMT2S disease model, we analyzed clinically relevant phenotypes. Mice were tested through a battery of neurobehavioral and physiological assessments at separate timepoints to assess sensation (von Frey, adhesive removal, hot plate), muscle strength and motor function (grip strength, rotarod, voluntary running wheel), and peripheral nerve function and morphology (nerve conduction velocity, nerve histology) (**Supp. Figure 2**).

Figure 11. CRISPR-cas9 induced E365del IGHMBP2 variant.
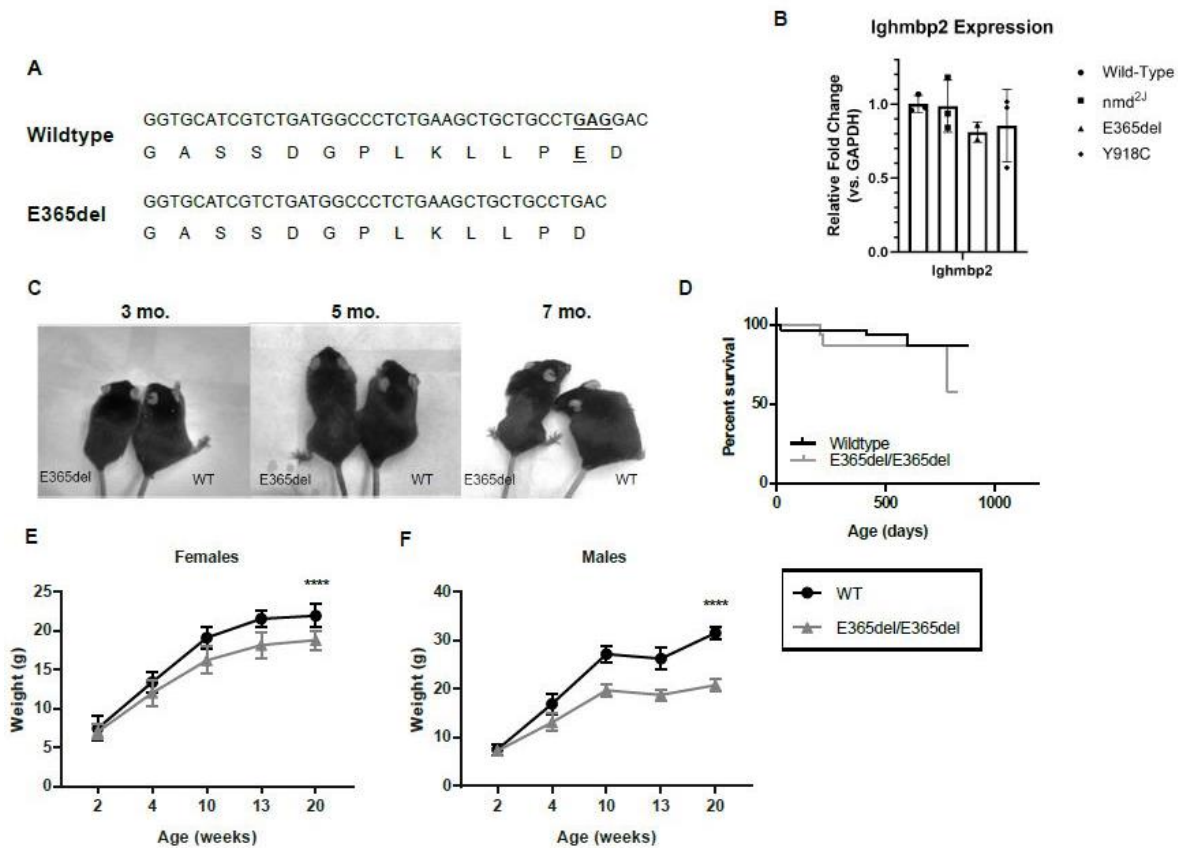
Figure 11. CRISPR-cas9 induced E365del IGHMBP2 variant. (a) Schematic of the variant in the Ighmbp2em1 strain (c. 1093_1095del; p.Glu365del) three nucleotide deletion underlined in the wildtype allele. (b) Ighmbp2 mRNA expression in 2 week-old wildtype, nmd2J, E365del and Y918C homozygous mutant spinal cords normalized to GAPDH (n=3 WT, n=2 E365del, n=3 nmd2J, n=3 Y918C). (c) Comparison of homozygous (HOM) and wildtype (WT) littermates at 3, 5, and 7 months indicates a progressive wasting of the muscles in the hindlimbs and waist, which is most remarkable at 7 months of age. (d) Survival curve of wildtype mice and E365del homozygous showed no significant difference between the two (n=33 Wildtype, n=26 Homozygous, p=0.4704; Log-Rank, Mantel-Cox test). (e-f) Homozygous E365del mice had significantly reduced body weight, evident by 10 weeks of age (p <0.0001) in females and by 4 weeks of age in males (p<0.0001). Mean body weights ± SD are shown for homozygous and wildtype littermates (n=4-15 mice per time point).

CMT2S patients exhibit a distal sensory loss that spreads proximally as the disease progresses (Cottenie et al., 2014; Liu et al., 2017; Wagner, Huang, Tetreault, Majewski, Boycott, Bulman, Dyment, & McMillan, 2015). To determine if homozygous mice had sensory deficits, we used the von Frey assay to test for mechano-sensitivity, and hot plate to test for thermonociception. Homozygous mutant mice exhibited an increase in sensitivity to mechanical force (allodynia) compared to wildtype mice apparent by 12 weeks of age (**Figure 12a**). There is a somewhat reduced thermo-sensitivity between genotypes when all timepoints are grouped together, but does not appear at each timepoint respectively (**Figure 12b**).

As patients of CMT2S present with both sensory and motor phenotypes, we also used an assay to test for sensorimotor deficits. The adhesive removal test uses a sticker placed on the mouse's forehead between the eyes and tests sensation and dexterity by measuring the time it takes to remove the adhesive. Homozygous mutant mice take longer to remove the adhesive compared to their wildtype littermates (**Figure 12c**).

CMT2S patients miss critical developmental motor milestones and may need walking aids in order to be ambulatory, due to locomotor deficits (Cottenie et al., 2014; Wagner, Huang, Tetreault, Majewski,

Boycott, Bulman, Dyment, & McMillan, 2015). Therefore, we analyzed locomotor performance of the

E65del homozygous mice. Homozygous mice exhibited reduced performance on the accelerating

rotarod, a test of muscular endurance, balance, and motor coordination (**Figure 12d**). We additionally

tested motor endurance and function with a voluntary running wheel. Female homozygous mice had a

slower overall speed during the dark cycle period (when mice are active) than their wildtype littermates,

while male mice, overall less active regardless of genotype, exhibited no difference (**Figure 12e**).

Figure 12. E365del homozygous mice model sensory and motor deficits.
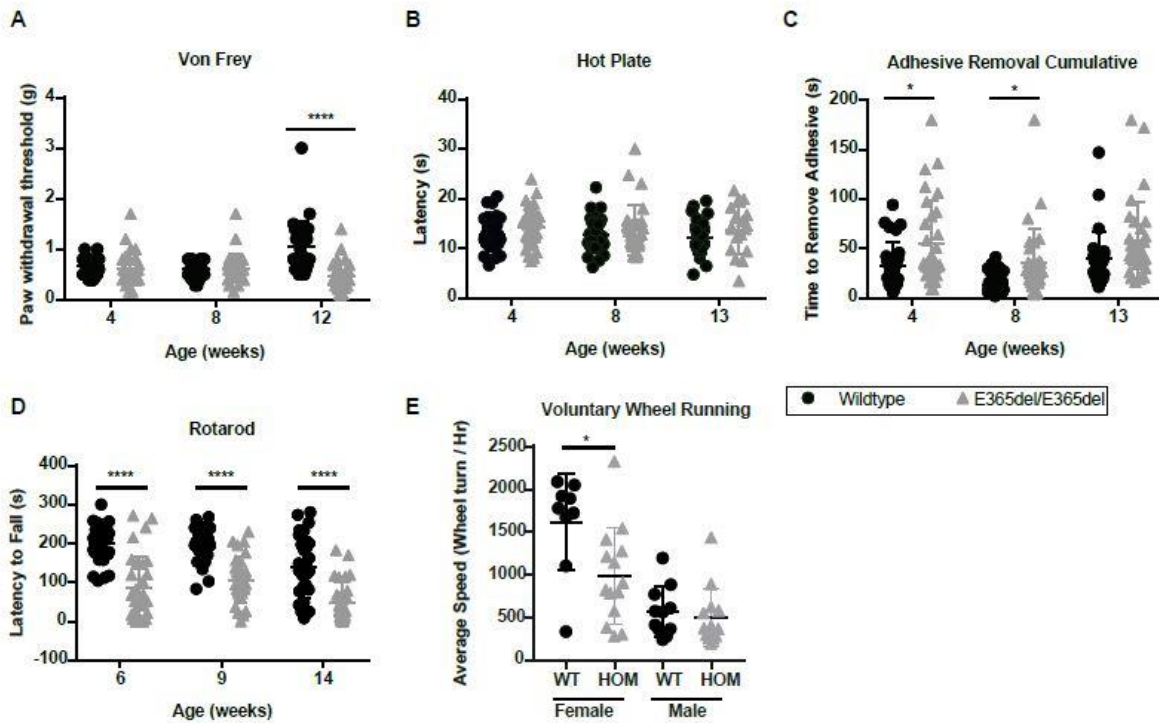
Figure 12. E365del homozygous mice model sensory and motor deficits. (a) von Frey assessment indicated that homozygous mice had significant (p<0.0001) hypersensitivity to mechanical allodynia. Homozygous sensitivity was (0.47±0.3g, n=30) evident by 12 weeks of age compared to wildtype (1.0±0.5g, n=30) littermates, which was not apparent at 4 or 8 weeks of age in wildtype (0.665±0.184, n=26; 0.610±0.174, n=26) or homozygous (0.619±0.314, n=30; 0.624±0.289, n=30). Individual threshold data points with mean and SD are plotted. (b) Hot plate assay was utilized to test for deficits in thermo-nociception. Homozygous mice show a genotype dependent sensitivity across the tested time-points (p=0.0193). Individual latency times with mean and SD are plotted. (c) Adhesive removal assay used for sensorimotor deficits indicated that homozygous mice took significantly longer to remove the sticker from the forehead across the tested time-points (p<0.0001). At 4 and 8 weeks of age this difference was pronounced (p=0.0162, p=0.0226), however by 13 weeks of age there was no significant difference (p=0.0889). Individual removal times with mean and SD are plotted. (d) Motor performance on a rotarod was measured by latency to fall and indicated significant deficits in homozygous mice evident by 6 weeks of age (p<0.0001). Individual latency times with mean and SD are plotted. (e) Motor performance and endurance was tested with voluntary running wheel. Average speed (total wheel rotations in dark cycle / time of dark cycle (12h) at 15 weeks of age. Wildtype females (n=9. 1621±561.8) ran significantly faster than homozygous female littermates (n=14.

3.2.3 Progressive degeneration of femoral sensory and motor myelinated axons and neuromuscular junctions in E365del homozygous mice

To determine if the sensory and motor phenotypes described above are indeed neurogenic, as observed in CMT2S patients, we assessed the function and morphology of peripheral nerves. For this, we analyzed the femoral sensory and motor nerves from the mice after undergoing the neurobehavioral assessments, cohorts of which are outlined in **Supp. Figure 2**. Degeneration of myelinated sensory axons was apparent by 4 weeks of age, with about 50% loss by 20 weeks of age (**Figures 13a,b**). Motor axon degeneration was apparent by 10 weeks of age, with an approximately 30% reduction by 20 weeks of age (**Figures 13c,d**). The neurodegeneration in the femoral sensory nerves impacted all axon calibers except for a small population of axons larger than 6 ⬜m (**Figures 13e**). The neurodegeneration in the femoral motor nerves significantly impacted axon calibers between 2-8 ⬜m, but not the smallest axons between 0-2 ⬜m and those 8 ⬜m+ (**Figures 13f**). An assay of nerve function was consistent with an

entirely axonal neuropathy, as nerve conduction velocities (NCV) were not different between

homozygous mice and wildtypes littermates (**Figure 13g**).

Figure 13. E365del homozygous mutants displayed progressive degeneration of femoral motor and
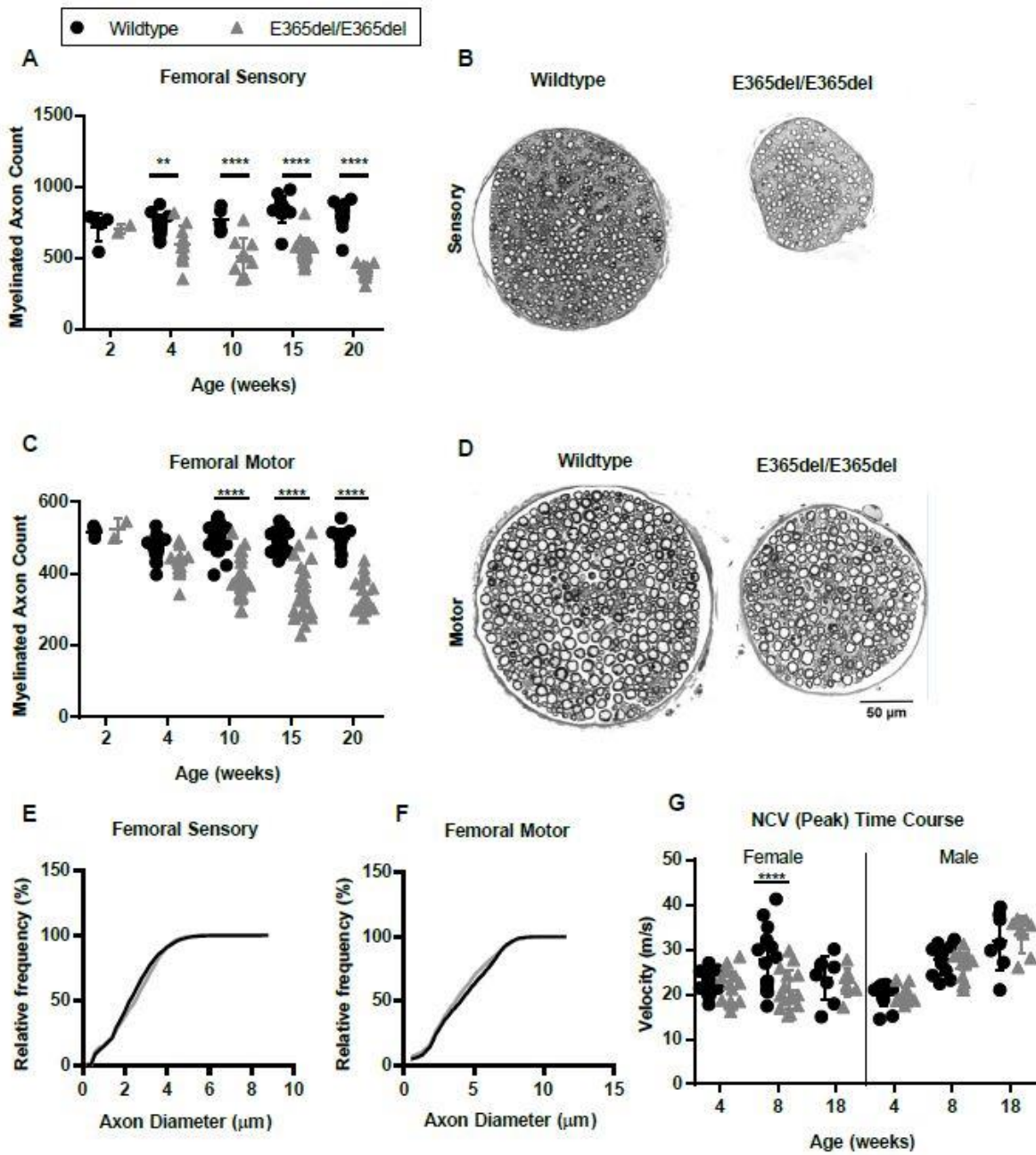
sensory axons.

Figure 13. E365del homozygous mutants displayed progressive degeneration of femoral motor and sensory axons. (a) Quantification of myelinated axons in the femoral sensory branch at five time points between 2 and 20 weeks indicates a significant loss evident by 4 weeks of age (p=0.0083) with about a 50% overall reduction in the homozygous sensory axons (404±50, n=11) compared to wildtype (794±96, n=12) by 20 weeks of age. (b) Cross-section of the wildtype femoral sensory branch is larger with more myelinated axons than the homozygous sensory branch at 20 weeks of age. (c) Quantification of myelinated axons in the femoral motor branch at five time points between 2 and 20 weeks indicates a significant loss evident by 10 weeks of age (p=0.0001) with about a 31% overall reduction in the homozygous motor axons (342.3±47, n=16) compared to wildtype (496±28.3, n=15) by 20 weeks of age. (d) Cross-section of femoral motor branch for wildtype indicated a significantly larger overall size with more myelinated axons. (e) Axon diameters of the femoral sensory nerves were analyzed via the Sidak's multiple comparison's test, and found that in bin sizes 0-2um, 2-4uM, and 4-6uM, there were significantly fewer axons in homozygotes than wildtype mice. (0-2uM, +/+=103.5±22.53, E365del/E365del=55.82±20.65, p=0.0177, 2-4uM, +/+=455.3±109.5, E365del/E365del=196±66.67, p=>0.0001, 4-6uM, +/+=225.2±37.87, E365del/E365del=147.5±23.93,p=>0.0001). +/+, n=12, E365del/E365del, n=12) (f) Axon diameters of the femoral motor nerves were analyzed via the Sidak's multiple comparison's test, and found that in bin sizes 2-4uM, 4-6uM, and 6-8uM there were significantly fewer axons in homozygotes than wildtype mice. (2-4uM, +/+=146.2±31.43, E365del/E365del=102.9±25.69, p=<0.0001, 4-6uM, +/+=131.8±12.69, E365del/E365del=100.5±9.585, p=>0.0026, 6-8uM, +/+=133.6±16.17, E365del/E365del=70.19±29.48,p=<0.0001). +/+, n=13, E365del/E365del, n=16) (g) Nerve conduction velocity was significantly reduced in only female mice at 8 weeks of age (p<0.0001), but by 18 weeks of age NCV was not significantly reduced in either male or female mice.

To determine if there is a dose-dependent effect of the phenotype based upon the number of mutant alleles the animal is carrying, the same analyses were performed in parallel in heterozygous E365del mice (**Supp.Figure 2, cohort 1**). No differences from controls were identified (**Supp. Figure 3**) indicating that the phenotypes described in homozygous E365del animals were completely recessive. This is consistent with heterozygous carriers of *IGHMBP2*/CMT2S alleles being asymptomatic.

Since CMT2S causes a distal loss of motor and sensory axons, we examined the neuromuscular junctions (NMJs) of homozygous and wildtype mice. In the gastrocnemius muscle of 15 week old wildtype mice,

43

each muscle fiber is contacted by a motor nerve terminal, which completely overlaps the post-synaptic

acetylcholine receptors (**Figure 14a,b**). However, in the homozygous E365del mice, the pre-synaptic

terminal is often absent, with regions of post-synaptic receptors present without complete innervation

of the junction (**Figure 14c-f**). When the percent of completely denervated junctions was quantified we

observed a significant and progressive loss of innervation evident by 8 weeks of age (**Figure 14g, Supp.**

Figure 4).

Figure 14. Neuromuscular junction degeneration in the E365del homozygous mice.
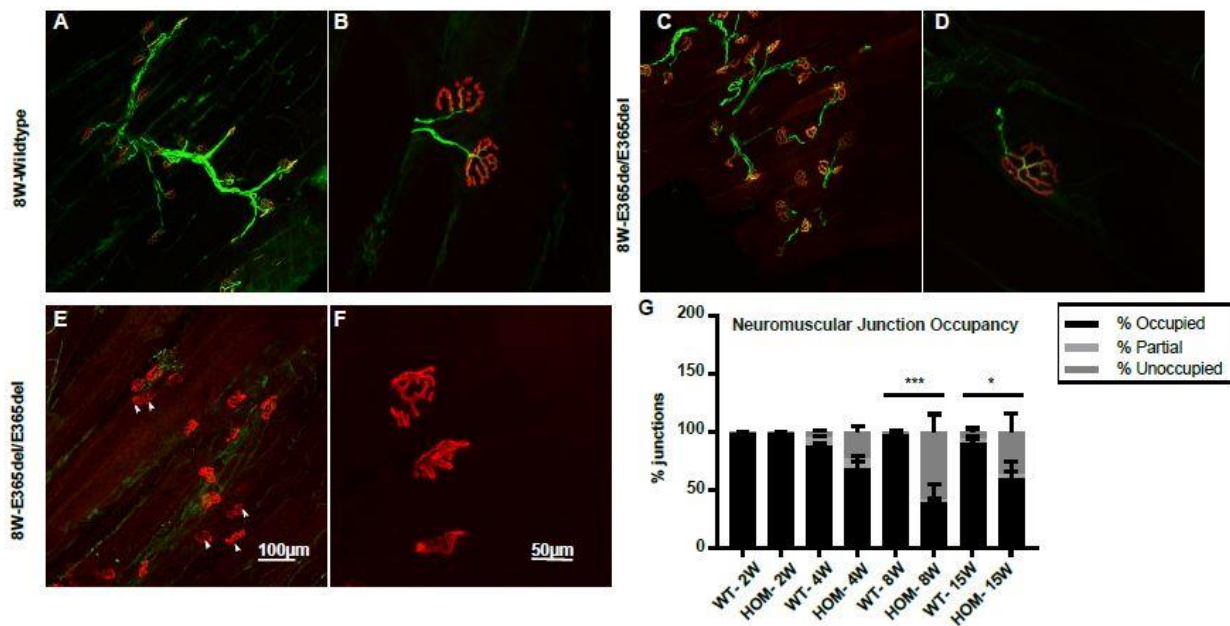
Figure 14. Neuromuscular junction degeneration in the E365del homozygous mice. (a-b)
Neuromuscular junctions (NMJs) of medial gastrocnemius muscle from 15 week old wildtype mice.
Tissues were stained for pre-synaptic vesicles (anti-SV2, green), neurofilaments (anti-neurofilament
2H3, green) and acetylcholine receptor (α-bungarotoxin, red). (a), low magnification and (b), high
magnification (c-d) Homozygous mice have exhibited a spectrum of phenotypes with some areas had
many innervated NMJs, (e-f) while other homozygous mice had many denervated NMJs highlighted
with white arrows. (g) NMJs were quantified as occupied, partially occupied or unoccupied. The
percent of junctions that were unoccupied was significantly different in homozygous compared to
wildtype evident by 8 weeks of age (p=0.0006) (n=3-20 per time point). Scale bar in (e) applies to (a) ,
(c), scale bar in (f), applies to (b), (d).

NMJ loss is more severe than the femoral motor nerve axon loss. The deficits at the neuromuscular junction are more pronounced than the femoral motor axon loss. This discrepancy could be explained by the lag time between NMJ degeneration and the resulting axon degeneration, and suggests a dying-back mechanism is occurring.

3.2.4 Muscular weakness and atrophy in E365del homozygous mice

As the neuromuscular junctions were significantly denervated by 8 weeks of age, we analyzed the impact on the distal hindlimb muscles. Muscular strength of the limbs was tested using a standard grip strength assay, analogous to grip strength measures utilized in human patients, which is reduced in CMT2S patients (Villalón et al., 2018). To tease apart the contribution of the fore- and hind-limbs to the phenotype, we examined the strength of the forelimbs alone, as well as all limbs combined. At all time-points tested, homozygous mice exhibited a reduction in all-paw grip strength compared to wildtype littermates, for both male and female mice (**Figure 15a**). However, we found that the reduction was more pronounced in the all-paw grip than the forepaws alone (**Supp. Figure 5A**), suggesting that IGHMBP2 E365del variant impacts the hindlimbs more than the forelimbs. Likewise, an assessment of lower limb muscular strength, isometric force-frequency curves, found progressive muscular weakness with age (**Supp. Figure 6**).

Analysis of the histology of the medial gastrocnemius (MG) shows regions of atrophic fibers indicative of neurogenic atrophy in the homozygous MG compared to uniform fibers in the wildtype muscle (**Figure 15b,c, Supp. Figure 5b**). Muscle weights of triceps surae (MG, lateral gastrocnemius, and soleus) also show significant differences in muscle weight to body weight ratios by at least 4 weeks in males **(Figure 15d)**. This muscle atrophy was widespread, as indicated by an overall smaller hindlimb cross-section size (**Supp. Figure 5c**).

Figure 15. E365del mice show muscle weakness and neurogenic atrophy. (
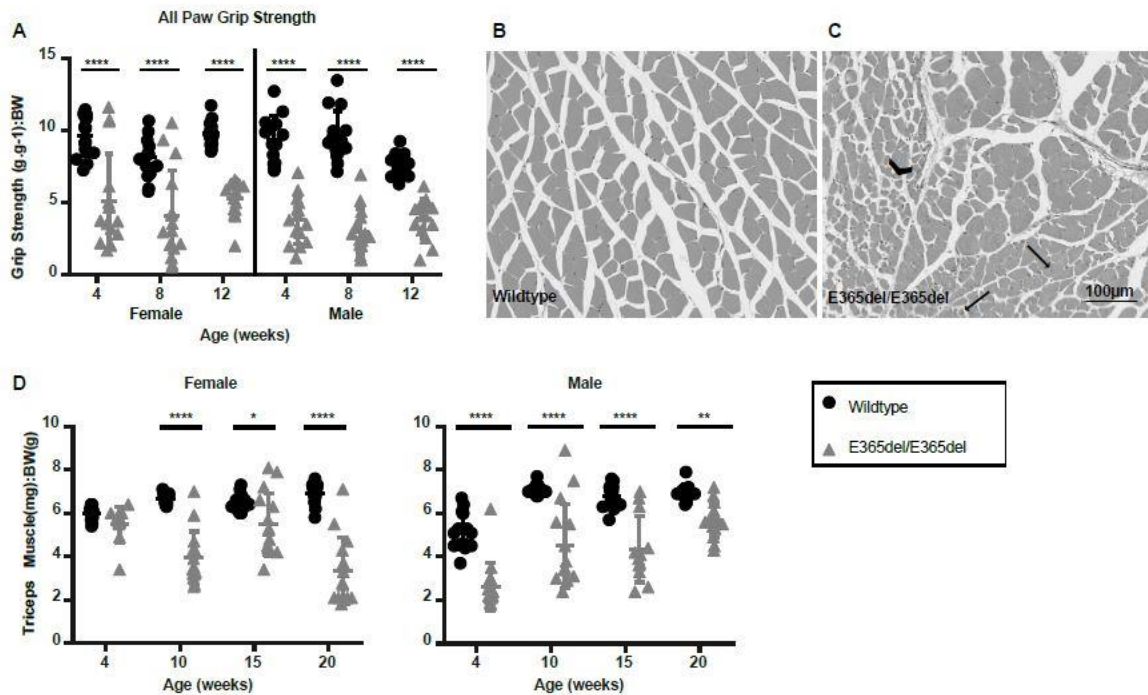
Figure 15. E365del mice show muscle weakness and neurogenic atrophy. (a) All paw grip strength assessment indicated that homozygous mice were weaker than wildtype at all time points (p<0.0001) for both female and male. Individual data points with mean and SD shown. (b) 8 week of age wildtype medial gastrocnemius (MG) cross-section stained with hematoxylin and eosin. (c) Homozygous MG cross-section shows regions of atrophied alongside regions of larger area fibers highlighted with an arrow head, with few central nuclei fibers highlighted by black arrows. (d) Both female and male homozygous mice exhibited a difference in the triceps muscle to body weight ratio, evident by 10 weeks of age (p<0.0001) in females and 4 weeks of age in male (p<0.0001). Individual data points with mean and SD shown.

Previous work has shown that cardiac muscle, as well as skeletal muscle, can be impacted by variants in

Ighmbp2 (Maddatu et al., 2004). In order to determine if the CMT2S model has phenotypes of dilated

cardiomyopathy, we assessed heart rate, EKG parameters, and heart size. None of the assessed

measures were indicative of cardiac dysfunction or abnormal phenotype due to the E365del variant

(**Supp. Figure 7**). Additionally, we determined that neuronal expression of wildtype *Ighmbp2* using a

transgene driven by the rat neuron-specific enolase 2 (NSE Tg) promoter in the E365del homozygous

mice makes them indistinguishable from wildtype animals (**Supp. Figure 8A-E**). Unlike the previously

characterized neuron-specific rescue in the SMARD1 mouse model (nmd^{2J}) using this same transgene (Maddatu et al., 2005), neuron-rescued E365del homozygous mice did not show signs of secondary skeletal or cardiac myopathies (**Supp. Figure 8F**).

3.2.5 CMT2S Patient allele IGHMBP2-Y920C validated in mouse model

While the E365del homozygous mouse recapitulates many of the clinical features observed in CMT2S patients, this is not a variant that has yet been observed in the patient population. Therefore, to further broaden the spectrum of CMT models available, we generated a human allele knock-in (human: c.2759A>G, p.Tyr920Cys; mouse c.2753A>G, p. Tyr918Cys). The patient carrying this homozygous variant is described as presenting with a juvenile-onset CMT with mild motor and sensory deficits (Yuan et al., 2017).

Similar to our E365del homozygous mice, our mouse model Y918C, modelled after the p.Tyr920Cys human variant, also presents with mild hindlimb wasting (**Figure 16a**), decreased body weight in males and females (**Figure 16b,c**) and deficits in motor function, apparent by inverted wire hang testing starting at 3 weeks of age (**Figure 16d**). Like both the human CMT2S patients and the E365del mouse model, the Y918C mouse model does not significantly impact lifespan to at least 8 months of age (**Figure 16e**).

Figure 16. Y918C mice displayed decreased body weight and motor deficits.
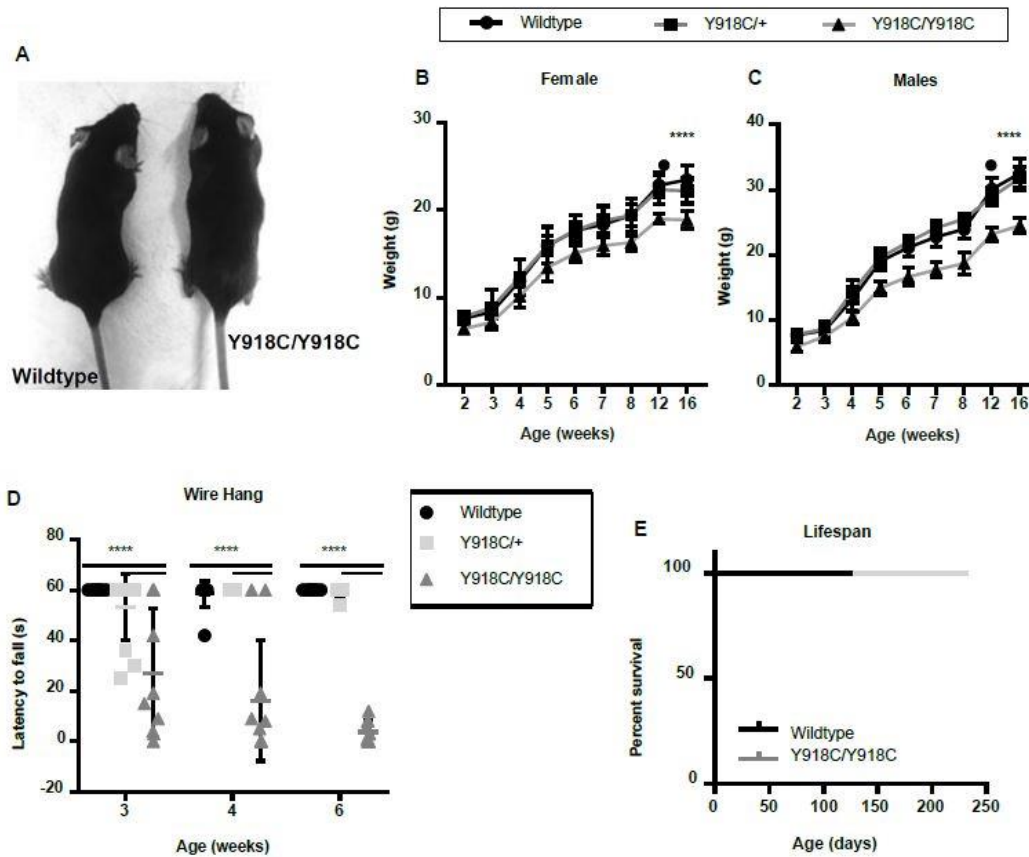
Figure 16. Y918C mice displayed decreased body weight and motor deficits. (a) Comparison of wildtype (WT) and homozygous (HOM) Y918C littermates body morphology at 2 months shows a progressive wasting of the muscles in the hindlimbs and waist in the mutants. (b) Homozygous Y918C mice had significantly reduced body weight, evident by 4 weeks of age (p <0.0001) in females and (c) by 5 weeks of age in males (p<0.0001). Mean body weights ± SD are shown for homozygous, heterozygous, and wildtype littermates (n=4-15 mice per time point). (d) Homozygous Y918C (n=10) mice displayed deficits in motor function and endurance as tested by the inverted wire hang assay evident by 3 weeks of age compared to wildtype (n=12) and heterozygous (n=13) littermates (p<0.0001). (e) Survival curve of wildtype mice and Y918C heterozygous and homozygous showed no significant difference between (n=12 Wildtype, n=29 Heterozygous, n=11 Homozygous, p=0.999; Log-Rank, Mantel-Cox test).

To determine if the sensory and motor axonal degeneration that is present in the E365del model were also observable in the Y918C model, we assessed the morphology and functional properties of the peripheral nerves. At 8 weeks of age we observed degeneration of myelinated axons in homozygous mice, with an approximately 13% overall reduction in the sensory branch and a 34% overall reduction in

the motor branch of the femoral nerve (**Figure 17a-c**). At 16 weeks, there is an approximately 21%

reduction in the sensory branch and a 32% reduction in the motor branch, showing that most of the

neuron death has occurred by 8 weeks and plateaus thereafter (**Figure 17d-e**). Another difference is

that, unlike the E365del, NCV testing found a decrease in velocity of the homozygous and heterozygous

mice compared to wildtype littermates (**Figure 17h**), consistent with the human patient (Yuan et al.,

2017).

 NMJs were quantified as occupied, partially occupied, or unoccupied. The percent of junctions that

were unoccupied was significantly different in homozygous compared to wildtype mice at 16 weeks of

age (n=5-7 per timepoint , p=<0.0001) (**Figure 17i)**.

Though characterized in less detail, the Y918C mice show a slightly more severe CMT2S phenotype

compared to the E365del mice. They have smaller hindlimbs, smaller motor neuron axon diameters,

and less occupied NMJs with approximately 30% fewer occupied NMJs at the 16-week timepoint

compared to the E365del mice (p=0.0043). However, E365del mice shows significantly more axonal loss

in both motor and sensory nerves compared to Y918C (**Figures 13a,c, 17b-e**). As the first precise human

CMT2S allele knock-in, these mice provide both construct and face validity for subsequent preclinical

studies. Axonal degeneration and muscular atrophy findings were comparable to the E365del model at

a similar time-point; however, at 8 weeks of age Y918C homozygous mice show a clear decrease in NCV,

as observed in the CMT2S patient (Preibisch et al., 2009). Interestingly, although Y918C and E365del

mice indicate a purely recessive phenotype for almost all measures tested, Y918C heterozygous mice

also show an intermediate decrease in NCV (**Figure 17h**). Though decreased motor axon diameter may

account for a decrease in NCV in Y918C homozygous mice, there is no significant difference between

Y918C heterozygous mice and wildtype mice femoral axon caliber **(Figure 17f,g)** or myelin g-ratios

(Figure 17j) to account for this decrease in NCV. E365del also shows a decrease in axon caliber, but show

no NCV phenotype. However, for NCVs, the sciatic nerve was measured which is composed of a

multitude of nerve types while the femoral motor nerve, is a small subset of motor neurons which may

also contribute to the discrepancy we see in NCVs between the Y918C homozygotes, heterozygotes, and

wildtypes as well as the differences we see between Y918C and E365del. Such findings may indicate a

clinically subthreshold reduction in conduction velocity, which may be present but untested in carriers.

To further support this, heterozygous mice with an *Ighmbp2*-knock-out allele (IMPC) show deficits in

vertical rearing activity (https://www.mousephenotype.org/data/genes/MGI:99954). Additional testing

of *IGHMBP2* variant carriers for susceptibility of mild CMT or neuromuscular disease phenotypes is

needed.

Figure 17. Y918C mice displayed degeneration of femoral motor and sensory axons.
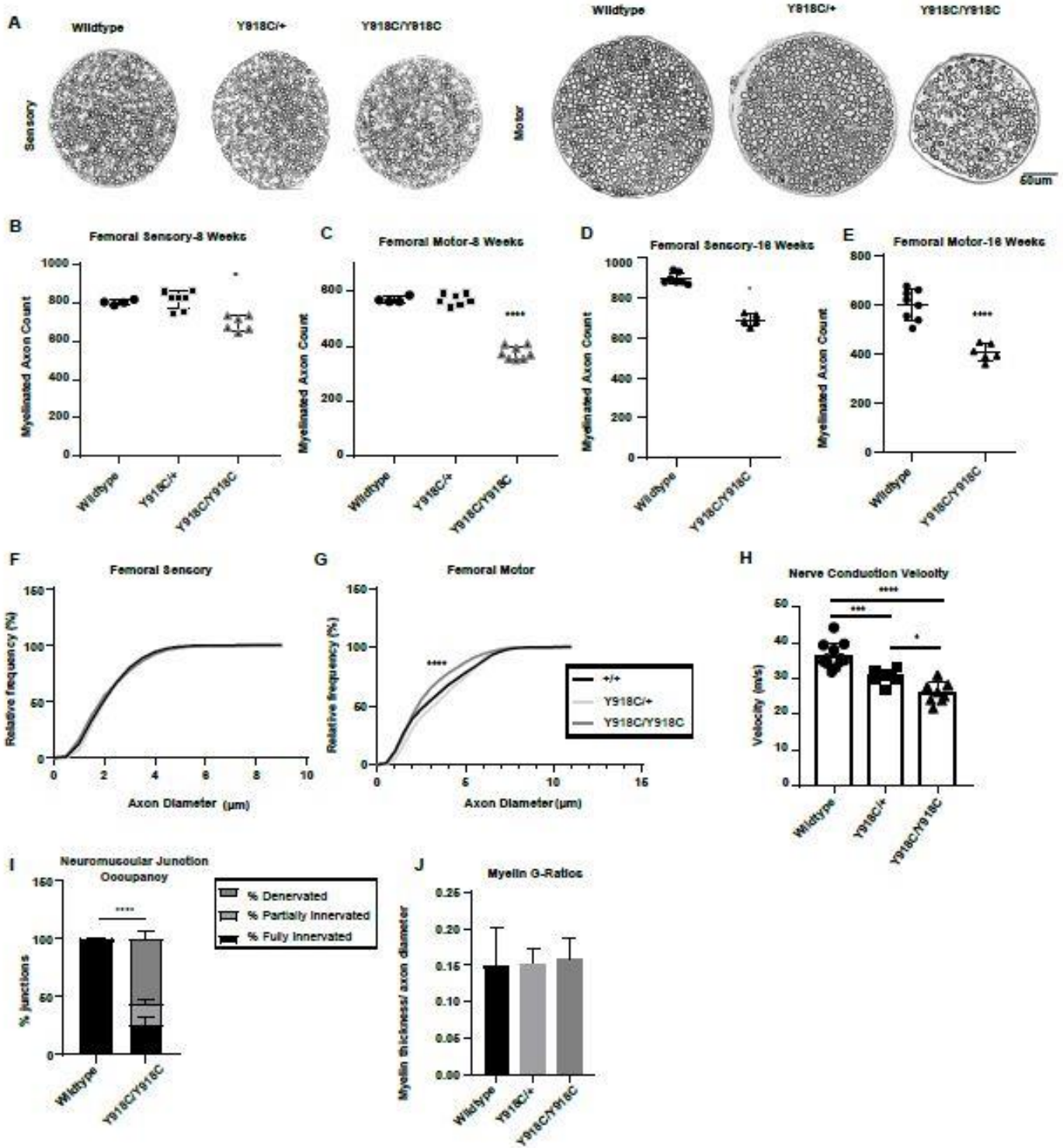
Figure 17. Y918C mice displayed degeneration of femoral motor and sensory axons. (a) Cross-sections of the wildtype, heterozygous and homozygous femoral sensory and motor branches at 8 weeks of age. (b) Quantification of myelinated axons in the femoral sensory branch indicates a significant difference (p=0.015) in the homozygous sensory axons (693±38.3, n=6) compared to wildtype (802±12.3, n=4) or heterozygous (816±46, n=7) at 8 weeks of age. (c) Quantification of myelinated axons in the femoral motor branch indicates significant (p<0.0001) degeneration in the homozygous axons (376±23.9, n=8) compared to wildtype (570±10.9, n=4) or heterozygous (569±20.7, n=7) at 8 weeks of age. (d) Quantification of myelinated axons in the femoral sensory branch indicates a significant difference (p=0.015) in the homozygous sensory axons (706.7±39.9, n=15) compared to wildtype (881.6±34.2, n=12) at 16 weeks of age. € Quantification of myelinated axons in the femoral motor branch indicates significant (p<0.0001) degeneration in the homozygous axons (404.8±34, n=6) compared to wildtype (597.9±62.33, n=8) at 16 weeks of age. (f) Axon diameters of the femoral sensory nerves were analyzed via the Tukey's multiple comparison's test, and found that in bin sizes 2-4uM, there were significantly fewer axons in homozygotes than wildtype and heterozygote mice respectively (p=0.0486, p=0.0351). (2-4uM, +/+=632.1±46.11, Y918C/+=578.1±109.7, Y918C/Y918C=470.7±33.08, +/+, n=7, Y918C/+, n=7, Y918C/Y918C, n=3) (g) Axon diameters of the femoral motor nerves were analyzed via the Tukey's multiple comparison's test, and found that in bin sizes 4-6uM and 6-8uM, there were significantly fewer axons in homozygotes than wildtype and heterozygote mice respectively (4-6uM:p=0.0063, p=<0.0001; 6-8uM:p=0.0053, p=0.0001). (4-6uM, +/+=147.5±16.83, Y918C/+=161.5±7.969, Y918C/Y918C=96±5.727, 6-8uM, +/+=116.5±23.49, Y918C/+=142.7±10.33, Y918C/Y918C=50.83±14.15, +/+, n=8, Y918C/+, n=6, Y918C/Y918C, n=6) (h) Nerve conduction velocity was significantly reduced in homozygous (n=8, 25.9±2.9, p<0.0001) and heterozygous (n=8, 30.5±1.9, p=0.0007) mice compared to wildtype littermates (n=12, 36.3±3.4), with heterozygous showing an intermediate phenotype, at 8 weeks of age. (i) NMJs were quantified as occupied, partially occupied or unoccupied. The percent of junctions that were unoccupied was significantly different in homozygous compared to wildtype evident by 16 weeks of age (p=0.0001) (n=5-7 per time point). (j) G-ratios (ratio of myelin thickness to axon diameter) of homozygous (0.159±0.076, n=7), heterozygous(0.153±0.049, n=6), and wildtype(0.150±0.086, n=3) showed no significant difference.

3.3 Discussion

Here we have characterized the first animal models of CMT2S. As with the human patients, the variants are recessive and causative of juvenile-onset distal axonopathy with deficits in locomotor and sensory function. The mice demonstrate progressive axonal degeneration in both the peripheral motor and sensory nerves. Like the patients, these models have a relatively unaffected lifespan, and no indications of respiratory distress. Furthermore, clinically-relevant assays show that mutant mice have deficits in mechano- and thermal sensation, as well as muscular strength and endurance. Based on the phenotypic

similarities, these variants are valid models of CMT2S for use in future mechanistic and preclinical studies.

The phenotypic variability observed across the *IGHMBP2*-associated disease spectrum remains poorly understood. Research examining the stability and function of patient variants suggests that both SMARD1 and CMT2S are caused by loss-of-function alleles (U. P. Guenther, Handoko, Varon, et al., 2009a; U.-P. Guenther et al., 2009). Variant heterogeneity alone cannot account for the phenotypic differences noted in patients, as patients with identical allelic combinations have presented with severity on both ends of the spectrum (U. P. Guenther, Handoko, Varon, et al., 2009b; Hamilton et al., 2015; Joseph et al., 2009). Some work suggests that there is a possible correlation between protein expression level, helicase activity and disease severity, as a gradient of expression seems correlative with phenotype severity (U. P. Guenther, Handoko, Varon, et al., 2009a). This spectrum can be observed in the mouse models of *Ighmbp2*, as homozygous null mice die at birth (data not shown and

https://www.mousephenotype.org/data/genes/MGI:99954), and *nmd*[2J], which has a unique variant impacting splicing of *Ighmbp2* which results in only ~20% wildtype protein expressed, live a median lifespan of 91.5 days (Cox et al., 1998b; Grohmann et al., 2004). Our models E365del and Y918C are both phenotypically less severe, suggestive of a hypomorphic protein, similar to that predicted in many of the patient alleles (U. P. Guenther, Handoko, Laggerbauer, et al., 2009b). The E365del variant falls within helicase domain 1C, while Y918C falls within the C terminus domain, a region that has been found to increase RNA-binding affinity (Lim et al., 2012). Both regions are critical for the enzymatic function of the helicase. An additional hypothesis in phenotypic heterogeneity is derived from work in mouse models, as well as findings in siblings, which suggests that genetic background variants can impact phenotypic severity (Cox et al., 1998a; Joseph et al., 2009; Shababi et al., 2019). Future work will look to leverage our new CMT2S mouse models in identifying susceptibility to known genetic modifiers of *Ighmbp2*-associated neuromuscular disease as well as gene therapy treatment strategies.

Previous work with the *nmd[2J]* model by our group indicated that rescuing the motor neuron disease, either through neuron-specific *Ighmbp2* expression, or genetic modification, unmasked a cardiomyopathy (Maddatu et al., 2004, 2005). We did not observe cardiac phenotypes in the E365del mice, but whether that reflects the reduced severity of the mutation compared to *nmd[2J]*, or if there is an allelic difference in the disease mechanism, is uncertain. The basis for the cardiomyopathy in the *nmd[2J]* mice is unclear, and it is unknown if SMARD1 and CMT2S patients are susceptible to cardiac dysfunction. This will be an important consideration as gene therapies and other treatment strategies are developed (Nizzardo et al., 2015; Shababi et al., 2016).

These models, though similar behaviorally and overtly, show nuanced differences at the histological and electrophysiological level further demonstrating a need to not only expand the range of *IGHMBP2* models to display the full spectrum of human disease associated with *IGHMBP2*, but the importance of mutation location in phenotypically similar disease models. Future work with these models can help to determine if previously tested gene therapies in SMARD1 models would be equally effective in these less severe mouse models (Nizzardo et al., 2015; Shababi et al., 2016). Determining the therapeutic window will be critical, as many patients are identified after significant motor and sensory function deficits and degeneration have begun. These mice show we can model the entire phenotypic spectrum of *IGHMBP2*-related diseases and will allow greater resolution to examine the pathomechanisms involved.

Finger, Histopathology Core, Rick Maser, Rebecca Boumil and Genetic Engineering Technologies, Rachel

Sands and the Microscopy Core, and the Neurobehavioral Phenotyping Service.

Conflicts of Interest

The authors have no conflicts to report.

CHAPTER 4

Gene Therapy in Mild and Severe IGHMBP2 Neuromuscular Disease Mouse Models

Single stranded P546.AAV9-Ighmbp2 and CBA.AAV9-Ighmbp2 vectors show marked motor improvement in a severe SMARD1 and CMT2S mouse models

Sarah Holbrook[1,2], Amy Hicks[1], Andrea Sierra Delgado[3], Shibi Lithke[3],Timothy Hines[1], Gregory Cox[1,2], Kathrin Meyer[3]

1. The Jackson Laboratory, Bar Harbor, ME 04609;

2. The University of Maine, Orono, ME 04460; 3Nationwide Children's Hospital, Columbus, OH 43205

Abstract: Spinal Muscular Atrophy with Respiratory Distress Type 1 (SMARD1) and Charcot-Marie-Tooth Disease Type 2S (CMT2S) are rare neuromuscular degenerative diseases caused by recessive deleterious mutations in Ighmbp2. Both diseases are marked by alpha-motor neuron death leading to neural degeneration and distal muscular atrophy. CMT2S has a later onset of symptoms starting around young adulthood while SMARD1 is characterized by respiratory distress between 6 weeks to 6 months of age and accelerated neuromuscular degeneration typically leading to death before 6 years of age. The monoallelic and recessive nature of these diseases make SMARD1 and CMT2S prime candidates for gene therapy. We tested two different ssAAV9.IGHMBP2 viral vectors utilizing two Ighmbp2 mouse models developed in our lab. The mouse model, C57Bl/6J-nmdCxem3 (hereafter referred to as L362del), is a severe SMARD1 mouse model based on a previously extinct mouse model, CBA-nmd1J, and the C57Bl/6J-nmdCxem5 (hereafter referred to as Y918C), is a CMT2S mouse model based on the human mutation, Y920C. One vector expressed IGHMBP2 via a truncated Methyl CpG island promoter (hereafter referred to as P546.IGHMBP2). The other vector expressed IGHMBP2 via a CMV enhancer Chicken Beta Actin promoter (hereafter referred to as CBA.IGHMBP2) (Powers et al., 2023). Intracerebral ventricular injections (ICV) of one of the vectors were performed on postnatal day one mice mimicking pre-onset therapeutic intervention. We saw a significant increase in movement, muscle, and nerves assays in both vectors in both models as well as a significantly increased lifespan. However, we saw better recovery from L362del mice injected with P546.IGHMBP2.

4.1 Introduction:

Deleterious mutations in Immunoglobulin H mu Binding Protein 2 (Ighmbp2) cause a spectrum of neuromuscular degenerative disease. IGHMBP2 is a low processivity helicase that is lowly expressed throughout the body. The role of IGHMBP2 is not well known, but previous studies suggest it is involved in translation and ribosomes (Guenther et al, 2009).

The disease most commonly associated with Ighmbp2 is Spinal Muscular Atrophy with Respiratory Distress type 1 (SMARD1) which is characterized by early onset distal neuropathy (typically seen within 6 weeks to 6 months of age) followed by diaphragmatic paralysis. This necessitates the need for these young patients to be mechanically ventilated and wheelchair bound. On the less severe side of the spectrum of disease is Charcot-Marie-Tooth disease type 2S (CMT2S) characterized by motor and sensory defects typically arising in young adulthood. On the most severe side of the spectrum are reported cases of infants dying of Sudden Infant Death Syndrome (SIDS). These patients were retroactively identified as having mutations in Ighmbp2 after the parents had children diagnosed with SMARD1 (Kim et al, 2019, Grohmann et al, 2003).

SMARD1 and CMT2S, due to their monoallelic recessive natures, are great candidates for gene therapy. Previous success has been seen in the less severe mouse model, nmd-2J with better success via intracerebroventricular injections than intravenous injections at early timepoints via a CBA.IGHMBP2 single stranded Adeno-Associated Viruses of Serotype 9 (ssAAV9) (Nizzardo et al, 2015, Shababi et al, 2018). Past studies using transgenic models of mice expressing wildtype Ighmbp2 in specific tissues reveal that mutant IGHMBP2 impacts the nerves more than the muscles with Eno2 promoter (nerve specific) -Ighmbp2 mice living longer and less muscular atrophy than Ttn promoter (muscle specific) – Ighmbp2 mice. Mice expressing both transgenes did better than either promoter alone suggesting that although the nerves are the most impacted tissues, IGHMBP2s role in the muscle is a contributing factor

to disease pathogenesis (Maddatu et al, 2004). This suggests that for therapeutic studies, nerve, muscle, and cardiac tissue should be monitored.

We used three different ssAAV9 vectors. One empty vector as a negative control (EV), one vector containing human Ighmbp2 expressed via a Chicken Beta Actin promoter with a CMV enhancer (CBA.IGHMBP2 hereafter), and one vector containing human Ighmbp2 expressed by a truncated Methyl CpG Island promoter (P546.IGHMBP2 hereafter) respectively. P546.IGHMBP2 expresses IGHMBP2 close to endogenous levels found in the muscle and nervous tissue. CBA.IGHMBP2 expresses at higher levels than endogenous levels (Powers et al., 2023).

To replicate human trials where a spectrum of patients with SMARD1 to CMT2S symptoms would be present, we wanted to test a spectrum of mice on both ends of phenotypic severity. The historical nmd-2J mouse model has been used before, but genetically is not similar to most human patients. It has splicing defect where it produces less wildtype protein representing ~3% of human population. Helicase mutations creating functionally impacted IGHMBP2 protein or unstable truncated protein are far more prevalent in the human population. C57Bl/6J-nmdCxem3 (hereafter referred to as L362del) is a more severe model of SMARD1 than nmd-2J with a lifespan of ~19 days versus 3 months and more severe neuromuscular degeneration in the hindlimbs and intercostal tissue (Holbrook et al, 2024). This mouse has a L362del mutation located in exon 8 of the helicase domain. The C57Bl/6J-nmdCxem5 (hereafter referred to as Y918C) is a milder CMT2S mouse model based on the human mutation, Y920C. It is much milder than other documented Ighmbp2 mouse models with an overt display of muscle weakness appearing around 4 – 6 weeks of age and no impact on lifespan (Martin et al, 2023). These mouse models were utilized in this gene therapy trial to simulate mid and pre-onset therapeutic intervention respectively. Due to the nature of the ssAAV9, mice injected with a single stranded vector will not begin producing RNA or protein for at least a week (Gray et al, 2009). The L362del model begins to show a

significant neuromuscular degeneration phenotype at ~4 days old (Holbrook et al, 2024). Though a self-complimentary or scAAV9 vector would be preferable, its size constraints (2.2kb) vs that of the ssAAV9 that can hold twice the gene size (Raj et al, 2011). With Ighmbp2 being ~3kb, without adding a promoter, a scAAV9 version of an Igmhbp2 vector is not possible for the time being.

4.2 RESULTS

Both CBA.IGMHBP2 and P546.IGMHBP2 show significant motor improvement and quality of life in severe SMARD1 mouse model, with P546.IGMHBP2 showing the best overall improvement:

For this pilot trial of 8 weeks, most AAV9-P546-Ighmbp2 and AAV9-CBA-Ighmbp2 treated L362del animals survived to the 8-week timepoint with two P546.IGMHBP2 animals dying at ~3 weeks and one CBA.IGMHBP2 animal dying at ~3 weeks. Empty vector animals were not statistically different from non-treated L362del animals. No negative impacts were seen in +/+ animals for lifespan in any group (**Figure 18a**).

In general, CBA.IGMHBP2 and P546.IGMHBP2 were statistically significantly different from +/+ animals starting at 1.5 weeks when non-treated L362del animals also diverged from +/+ animals. At 2.5 weeks, the CBA.IGMHBP2 and P546.IGMHBP2 treated animals are statistically different from both the +/+ animals and the non-treated L362del and empty vector animals (**Figure 18b,c**). General body condition is significantly improved in CBA.IGMHBP2 and P546.IGMHBP2 L362del animals with no signs of hindlimb clasping, paralysis, or grooming deficits.

Figure 18. CBA.IGHMBP2 and P546.IGHMBP2 treatments increase lifespan and bodyweight in L362del mice.
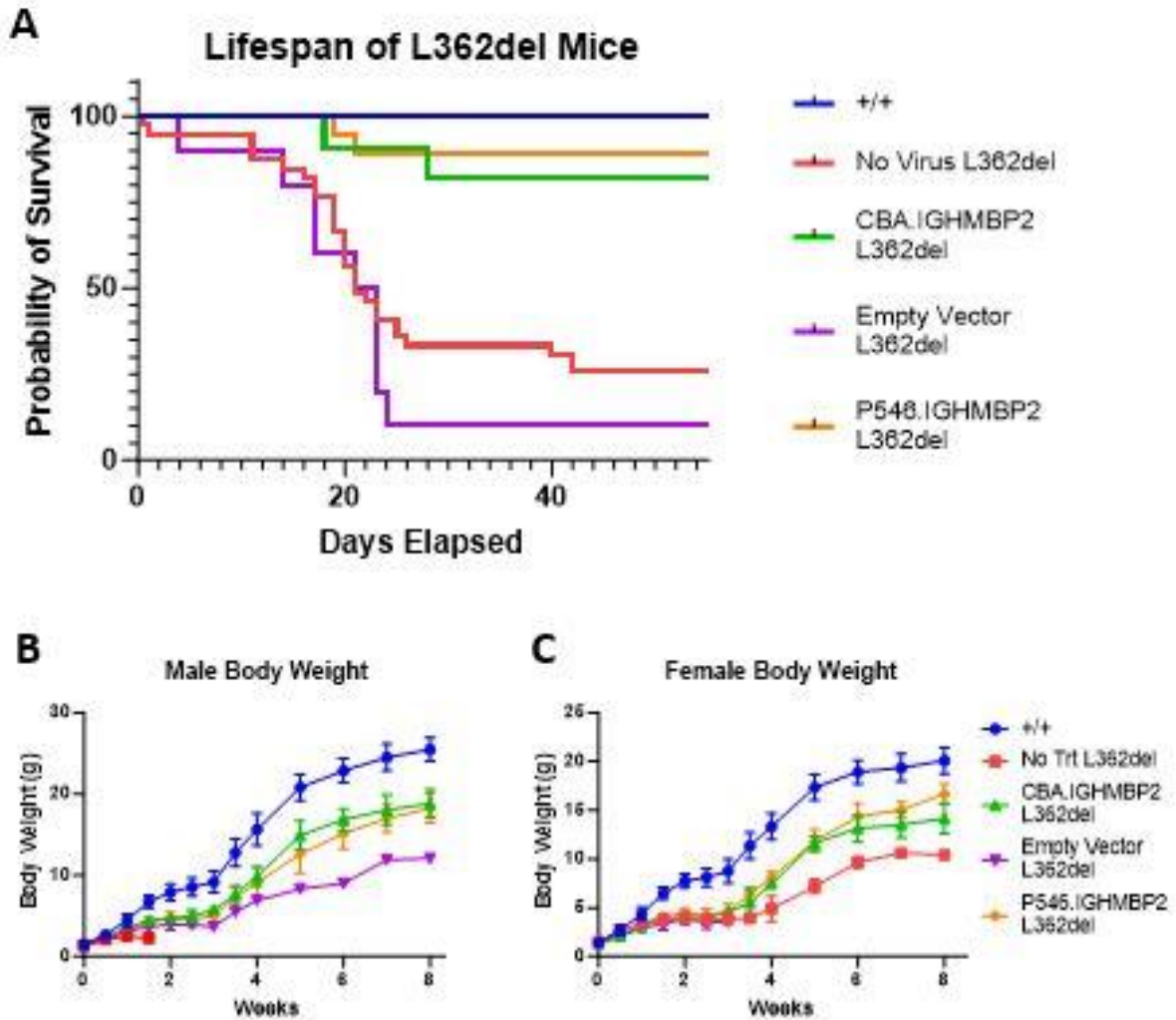
Figure 18. CBA.IGHMBP2 and P546.IGHMBP2 treatments increase lifespan and bodyweight in L362del mice. (a) Treated mice live significantly longer than non treated and empty vector treated L362del mice; +/+ (N=15), No Treatment L362del (N=39), CBA.IGHMBP2 L362del (N=11), Empty Vector L362del (N=10), P546.IGHMBP2 L362del (N=18). (b)Treated male L362del mice weight significantly more than untreated or empty vector treated L362del mice, but are still significantly smaller than +/+ mice. All L362del mice, treated or otherwise are significantly different from +/+ by 1 week of age. (Empty Vector: p=0.0029)(P546.IGHMBP2: p=0.0005)(CBA.IGHMBP2: p=0.0052). At 3 weeks of age, CBA.IGHMBP2 is significantly bigger than empty vector L362del (p=0.0244) and P546.IGHMBP2 is trending at p=0.0841. At week 4, 6 of the 7 empty vector treated mice have passed away leading to an inability to perform stats. However, due to CBS.IGHMBP2 and P546.IGHMBP2 mice never being significantly different from each other and the one remaining empty vector mouse being ~6grams less than the treated mice at week 8, it is safe to assume that the P546.IGHMBP2 treatment is also effective in increasing body weight in L362del mice. +/+ (N=15), No Treatment L362del (N=1), CBA.IGHMBP2 L362del (N=8), Empty Vector L362del (N=7), P546.IGHMBP2 L362del (N=8). (c) Treated female L362del mice weight significantly more than untreated or empty vector treated L362del mice, but are still significantly smaller than +/+ mice. All L362del mice are significantly different from +/+ at 1.5 weeks of age (p<0.0001). At 3.5 weeks of age, P546.IGHMBP2 treated mice are significantly larger than untreated L362del mice (p<0.0001). CBA.IGHMBP2 and CBA.IGHMBP2 mice are never significantly different from each other. The CBA.IGHMBP2 treated mice are significantly different from untreated L362del mice at 4 weeks of age (p=0.0341). +/+ (N=15), No Treatment L362del (N=7), CBA.IGHMBP2 L362del (N=5), Empty Vector L362del (N=4), P546.IGHMBP2 L362del (N=9).

L362del mice also showed a significant increase in strength. Mice, starting at 3 weeks and measured weekly until 8 weeks, were inverted on a wiregrid for 60 seconds to measure endurance and limb strength of all 4 limbs. Empty vector L362del animals and non-treated L362del animals that make it past the typical 3 week lifespan are never able to grasp the wiregrid and thus cannot perform the wirehang for any amount of time. P546.IGMHBP2 animals are not statistically different from +/+ animals while CBA.IGMHBP2 animals show much more variance with all CBA.IGMHBP2 L362del animals having drops in hanging wire performance during the trial period. At the end of the 8 week trial, some CBA.IGMHBP2 L362del animals regained the ability to wire hang for the full 60 seconds while others did not. (**Figure 19**).

Figure 19. L362del mice treated with P546.IGHMBP2 show no significant difference in latency to fall compared to +/+ while CBA.IGHMBP2 treated mice show variability.
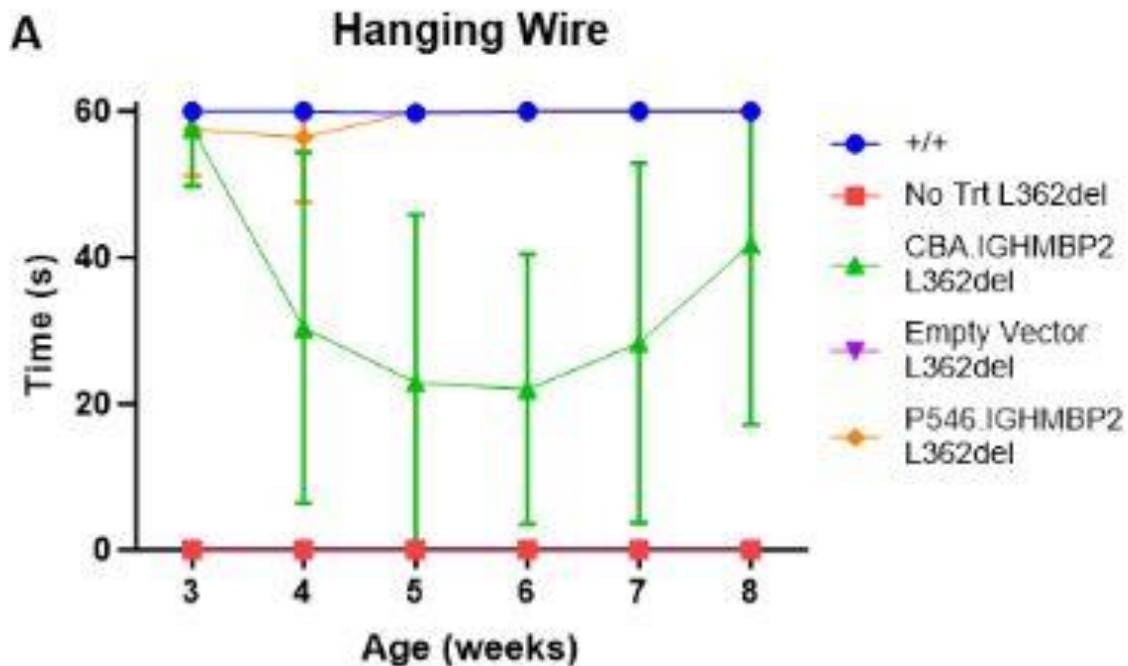
Figure 19. L362del mice treated with P546.IGHMBP2 show no significant difference in latency to fall compared to +/+ while CBA.IGHMBP2 treated mice show variability. Empty vector (N=3) or untreated (N=1) L362del mice that survived past the typical ~3 week lifespan were unable to wirehang. P546.IGHMBP2 treated (N=16) L362del mice showed no significant difference from +/+ (N=15) mice while CBA.IGHMBP2 mice show no significant difference in latency to fall at 3 weeks (p=0.85) but gradually show a decreased ability at week 4 (median= 30.36s+/-24s, p=0.0144) while 10 out of the 11 mice were unable to wirehang for the full 60 seconds at week 6. However, by week 8, some mice regained the ability to wirehang while others still struggled.

In SMARD1, the most impacted muscles are those of the distal limbs and those associated with respiratory function. For our study, we focused on the medial gastrocnemius (MG) and soleus (Sol) in the calf and the intercostal (Int) muscles. The MG was chosen due to its high density of "fast twitch" fibers associated with bursts of use while the Sol was chosen due to its high density of "slow twitch" fibers associated with endurance. For muscle areas of the MG, we see that the all muscle groups are significantly different from each other including the no virus and empty vector L362del mice (**Figure 20a,b**). From largest to smallest fiber areas are, +/+, P546.IGHMBP2, CBA.IGHMBP2, no virus, and empty

vector. In the MG, we see that the P546.IGHMBP2 mice have very few small fibers and overlap with the

+/+ animals until the 500uM^2 mark where it quickly plateaus with almost 100% of fibers being

1,300uM^2 and larger while the CBA.IGHMBP2 animals still show the wide range of fiber sizes showing a

middling effect between the non-treated mice and the +/+ animals. In the soleus, we see a similar

pattern as the fibers in the MG, however, the P546.IGHMBP2 treated mice are not significantly different

from +/+ mice (**Figure 20a,c**). Also, ~10% of the CBA.IGHMBP2 fibers are larger than any of those seen in

the +/+ mice indicating some significant hypertrophy in these mice. This same pattern is found in the

intercostal muscles with similar spectrums of fiber sizes found in each group and with a less extreme

disparity in size differences (**Supp. Figure 9**). In the Sol, we see a similar pattern of muscle sizes and

variance except for the CBA.IGHMBP2 mice. They still have a plateauing effect showing a greater

number of smaller and larger fibers than the +/+, but some of the larger fibers exceed the sizes seen in

the +/+ mice. This bimodal pattern of small and large fibers suggests that there may still be neurogenic

muscular atrophy in these animals with some more atrophied and hypertrophied cells than seen in the

+/+ or P546.IGHMBP2 animals.

Figure 20. The Medial Gastrocnemius (MG) and Soleus (Sol) of CBA.IGHMBP2 and P546.IGHMBP2 treated L362del mice are significantly larger than non-treated L362del mice, but not as large as +/+ mice.
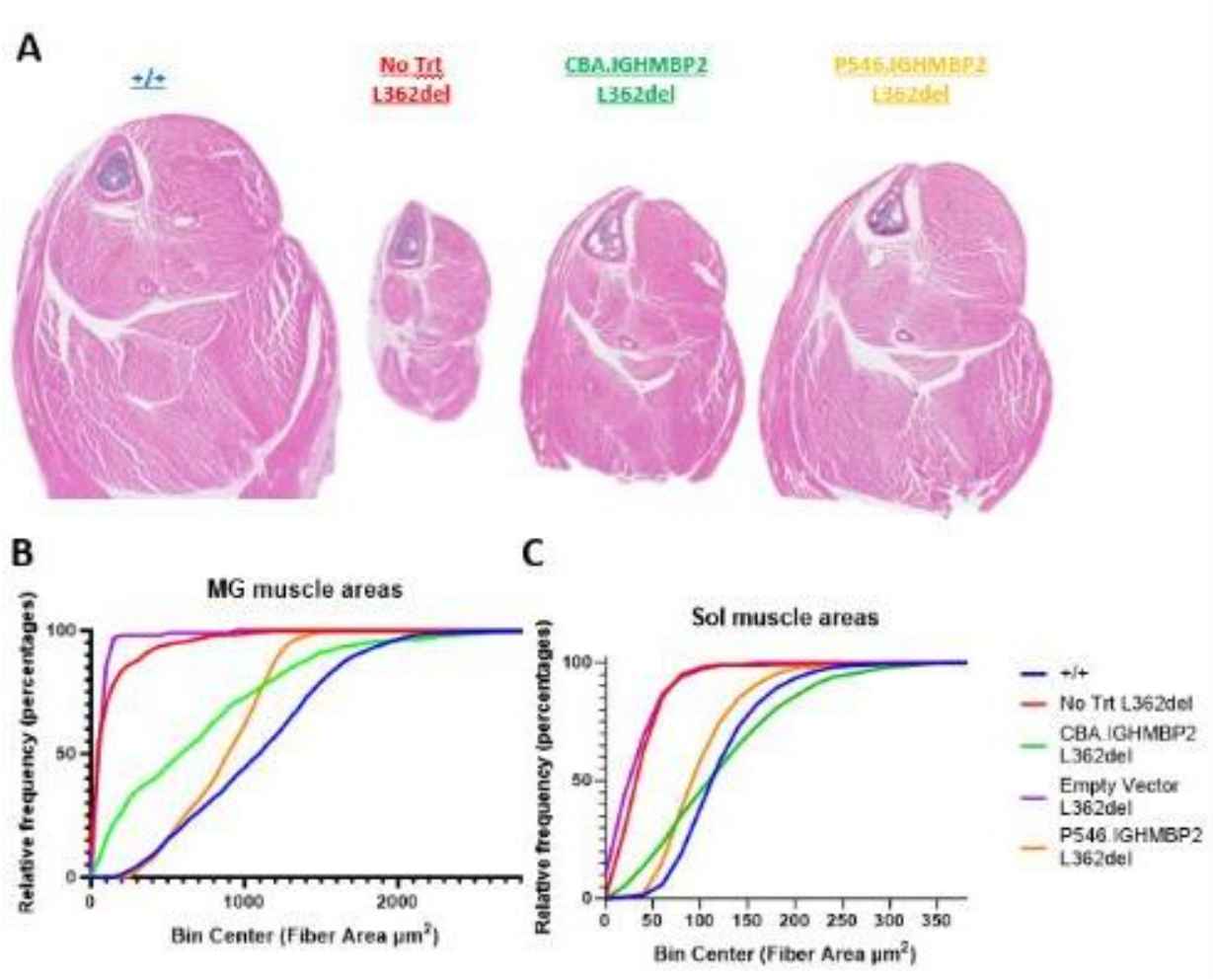
Figure 20. The Medial Gastrocnemius (MG) and Soleus (Sol) of CBA.IGHMBP2 and P546.IGHMBP2 treated L362del mice are significantly larger than non-treated L362del mice, but not as large as +/+ mice. (a) At 8 weeks of age, cross sections of the hindlimb show that CBA.IGHMBP2 and P546.IGHMBP2 L362del mice are much larger and overtly healthier than those of the untreated L362del mice. (b) The cumulative frequency of the MG shows all groups are significantly different from each other except for the empty vector vs untreated L362del mice (KS test, p=0.428). +/+ vs CBA.IGHMBP2 (p<0.0001). +/+ vs P546.IGHMBP2 (p<0.0001). P546.IGHMBP2 vs CBA.IGHMBP2 (p=0.0005). Means: +/+ = 1109 +/- 509, Untreated L362del = 142μm +/- 199, CBA.IGHMBP2 = 719μm +/-595, Empty Vector L362del = 91μm +/-101, P546.IGHMBP2= 886μm +/-300) (c) The cumulative frequency of the Sol shows all groups are significantly different from each other except for the CBA.IGHMBP2 vs P546.IGHMBP2 mice (KS test, p=0.2154) +/+ vs P546.IGHMBP2 is not significant (p=0.3865). +/+ vs CBA.IGHMBP2 (p<0.0001). Untreated L362del vs Empty Vector L362del (p=0.0212). Means: +/+ = 130μm +/-48 , Untreated L362del = 47μm +/-31 , CBA.IGHMBP2 = 129μm +/-73, Empty Vector L362del = 40μm +/-30, P546.IGHMBP2= 109μm +/-41).

To determine if axon loss and degeneration may account for the deficits we see in the hindlimb muscles, we extracted the femoral motor (FM) (**Figure 21a**) and femoral sensory (FS) nerves (**Figure 21b**) and counted the myelinated axons in each for each group. For the FM nerve, the average number of axons for +/+ mice is 580 +/- 27 axons. For untreated L362dels, the average is 333 +/- 14 axons. For P546.IGHMBP2 L362dels, 507 +/- 42 axons. For CBA.IGHMBP2 L362dels, the average is 517 +/- 44 axons. There is a significant difference between all groups except for the P546.IGHMBP2 and CBA.IGHMBP2 groups from each other (**Figure 21c**). As for the FS, there is no significant difference between the +/+s, P546.IGHMBP2 L362dels, and CBA.IGHMBP2 L362dels while they are all significantly different from the untreated L362dels. +/+s have an average axon count of 803 +/- 132 axons. Untreated L362dels have an average of 425 +/- 4 axons. P546 L362dels are 753 +/- 104 axons. CB L362dels are 805 +/- 93 axons (**Figure 21d**).

Figure 21. The Femoral Motor (FM) and Femoral Sensory (FS) Nerves show significant improvement in CBA.IGHMBP2 and P546.IGHMBP2 animals.
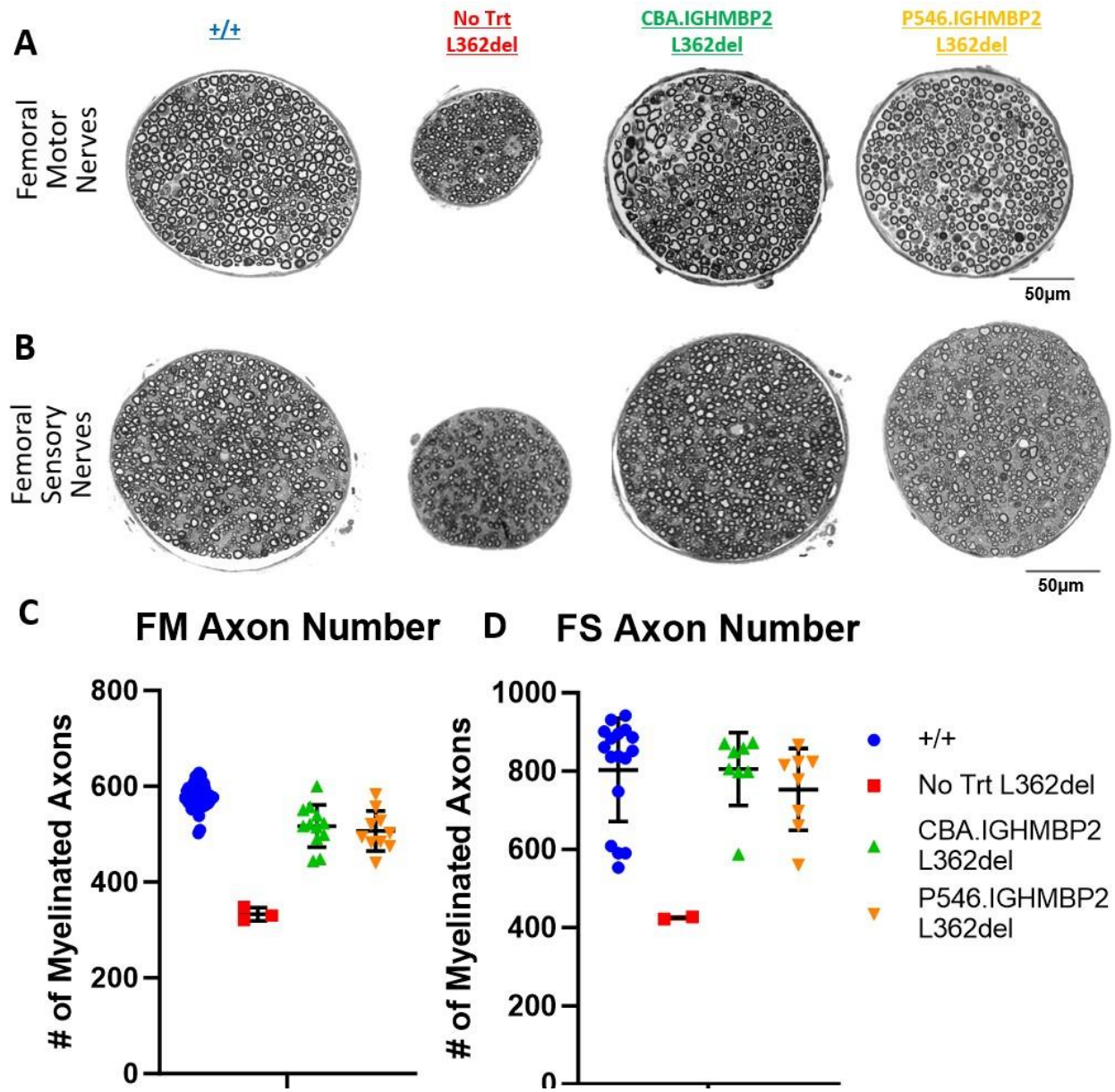
Figure 21. The Femoral Motor (FM) and Femoral Sensory (FS) Nerves show significant improvement in CBA.IGHMBP2 and P546.IGHMBP2 animals. (a) Cross sections of the FM show that CBA.IGHMBP2 and P546.IGHMBP2 treated animals are overtly more similar to +/+ mice than untreated L362del mice. (b) Cross sections of the FS show that CBA.IGHMBP2 and P546.IGHMBP2 treated animals are overtly more similar to +/+ mice than untreated L362del mice. (c) Quantification of the FM nerve show a significant myelinated axon count difference between all groups (p<0.0001) except for CBA.IGHMBP2 and P546.IGHMBP2 animals (p=0.883). +/+ Means: +/+ (N=45, 580+/-27), Untreated L362del (N=3, 333+/-14), CBA.IGHMBP2 (N=12, 517+/-44), P546.IGHMBP2 (N=507, +/-42). (d) Quantification of the FS nerve show no significant myelinated axon count difference between +/+, CBA.IGHMBP2, and P546.IGHMBP2 animals. The +/+, CBA.IGHMBP2, and P546.IGHMBP2 mice are all significantly different from the untreated L362del mice (+/+: p=0.0007; CBA.IGHMBP2: p=.0013; P546.IGHMBP2: p=0.006). Means: +/+ (N=17, 803+/-132), Untreated L362del (N=2, 425+/-4), CBA.IGHMBP2 (N=8, 805+/-93), P546.IGHMBP2 (N=8, 753+/-104).

Though there is a small deficit in the FM nerves of the CBA.IGHMBP2 mice which may account for some of the bimodal muscle fiber distribution in the MG, a similar number of axons is seen in the P546.IGHMBP2 nerves as well. This suggests that there may be a deficit associated with the neural muscular junctions (NMJs). To determine this, we performed NMJ staining on the MG and Sol. Though not as severe as non-treated L362del animals, CBA.IGMHBP2 and P546.IGMHBP2 animals showed significant full and partial denervation in the MG compared to the +/+ with CBA.IGMHBP2 having significantly more denervation than P546.IGMHBP2 in the soleus and medial gastrocnemius. In the soleus, the P546.IGHMBP2 are not significantly different from +/+ (**Supp. Figure 10a,b**). Upon closer inspection of the NMJs of the P546.IGHMBP2 mice and CBA.IGHMBP2 mice respectively, the morphology of the NMJs is also significantly different. While the NMJs of the P546.IGHMBP2 mice look like those of the +/+, the CBA.IGHMBP2 NMJs show stretched out NMJs with instances of sprouting (**Supp. Figure 10c**).

For nerve conduction velocities, we see that the treated L362del mice are not significantly different from the untreated mutants and all groups are significantly different from the +/+s. This suggests that even though there is an improved axon count to the femoral nerves of the hindlimb, there may be more

damage to the sciatic nerve, the nerve that an NCV directly tests, upstream of the femoral nerves (**Supp. Figure 11**).

In regards to the L362del mice, both vectors prove incredibly effective for improving lifespan, body condition, and neuromuscular health. P546.IGHMBP2 mice perform better than CBA.IGHMBP2 and show better muscle and NMJ health.

4.2.1 CBA.IGMHBP2 and P546.IGMHBP2 show improved motor and quality of life improvements in CMT2S mouse model with both viruses not statistically different from each other

The severe SMARD1 mouse model, L362del, shows great promise when treated with either vector at p1. However, due to the severity of their phenotype and the delay of the onset of the vector due to their single stranded nature, by the time the ssAAV9 vectors are producing wildtype IGHMBP2, the mice are already beginning to show neuromuscular deficits thus modeling a mid-onset scenario or therapeutic intervention. The other model of mice we tested the ssAAV9 vectors on are of the much milder neuromuscular disease, CMT2S, which shows a later onset of disease in both humans and mice. Our model, Y918C, has an approximate onset of neuromuscular deficits around 6 weeks of age and has no impact on lifespan (Martin et al, 2023). By performing p1 ICV injections on these animals, they model a pre-onset or "best case" scenario of therapeutic treatment.

Due to the later onset of disease in the Y918C mice, the trial lasted for 16 weeks to study potential improvements. Body weights between affected Y918C animals and WT animals do not show a statistical significance in females but do in males (**Figure 22a,b**). The results suggest that both CBA.IGMHBP2 and P546.IGMHBP2 are trending to be in between WT and non-treated Y918C animals similar to what is seen in the L362del animals, though not nearly as small. Though there is not an impact on lifespan in Y918C animals and body weight is not very different between +/+ and non-treated Y918C animals, there are significant overt body condition differences. Non-treated Y918C animals will have

narrower lower bodies with very little ability to move their hind legs with them typically contracting

against the body over time as the muscles atrophy. This often leads to them dragging their lower bodies.

However, general body condition is improved significantly in CBA.IGMHBP2 and P546.IGMHBP2 Y918C

animals with no signs of hindlimb clasping, paralysis, hindlimb contracture, or grooming deficits.

Figure 22. Untreated and empty vector Y918C males are smaller than +/+.
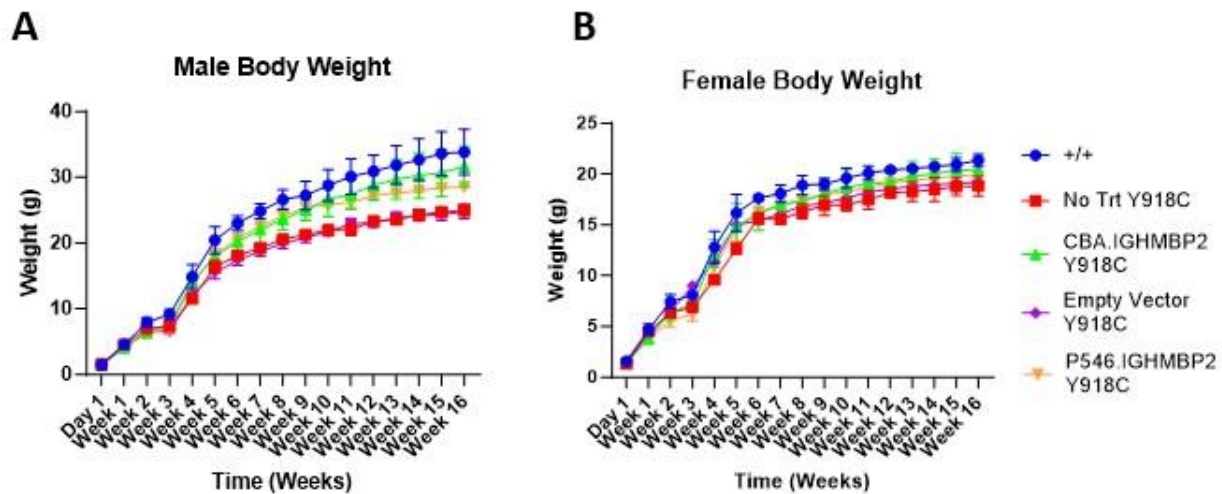
Figure 22. Untreated and empty vector Y918C males are smaller than +/+. (a) Untreated male and empty vector Y918C mice weight significantly less than +/+, while CBA.IGHMBP2 and P546.IGHMBP2 mice are not significantly different from any other groups. +/+ (N=6), No Treatment Y918C (N=5), CBA.IGHMBP2 Y918C (N=2), Empty Vector Y918C (N=6), P546.IGHMBP2 Y918C (N=3). (b) All female groups are not significantly different from each other. +/+ (N=3), No Treatment Y918C (N=3), CBA.IGHMBP2 Y918C (N=4), Empty Vector Y918C (N=5), P546.IGHMBP2 Y918C (N=5).

Mice, starting at 3 weeks and measured weekly until 16 weeks, were inverted on a wiregrid for

60 seconds to measure endurance and limb strength of all 4 limbs. Both P546.IGMHBP2 and

CBA.IGMHBP2 treated Y918C/Y918C animals were able to consistently wire hang for 60 secs throughout

the 3 week to 16 week portion of the study with no statistical difference between WT, CBA.IGMHBP2,

and P546.IGMHBP2. (**Figure 23**).

Figure 23. There are no significant differences in latency to fall between +/+, CBA.IGHMBP2, and

P546.IGHMBP2 Y918C mice.
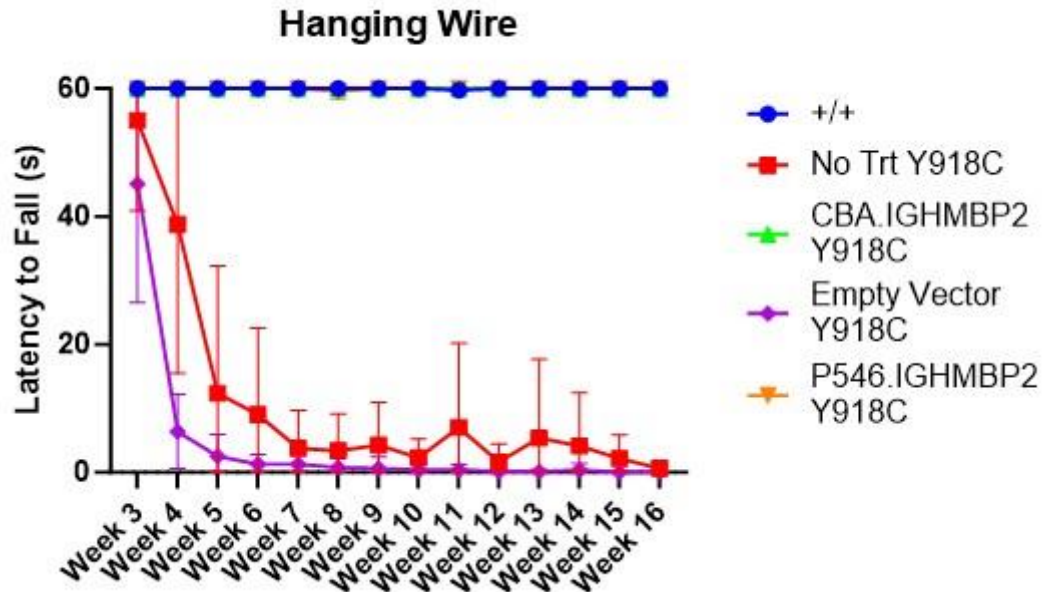
Figure 23. There are no significant differences in latency to fall between +/+, CBA.IGHMBP2, and P546.IGHMBP2 Y918C mice. There is no significant difference between +/+(N=9), CBA.IGHMBP2(N=6), and P546.IGHMBP2(N=8). There is a significant difference between untreated Y918C (N=8) and empty vector Y918C (N=8) at week 4 (p=0.0314) with empty vector mice falling sooner.

The MG and Sol of CBA.IGHMBP2 and P546.IGHMBP2 treated animals are not distinguishable from

those of +/+ animals while significantly different from the empty vector and non-treated Y918C controls

(**Figure 24**). This also holds up for FM and FS axon count (**Figure 25**) and NMJ occupancy **(Supp. Figure**

12a,b). However, there are significant differences seen in nerve conduction velocity (**Supp. Figure 12c**).

The P546.IGHMBP2 promoter is significantly different from the +/+ mice but not from the untreated

Y918C mice. The CBA.IGHMBP2 mice are not significantly different from +/+ or untreated Y918C mice.

Interestingly, both the P546.IGHMBP2 and CBA.IGHMBP2 mice are significantly different from the empty

vector treated Y918C mice. Though the untreated Y918C and empty vector Y918C mice are not

statistically significant from each other, the difference suggested by the two treated groups leans

towards the empty vector Y918C mice being slightly worse than the untreated Y918C mice. This coupled

with the wirehang data where the empty vector Y918C mice show overt muscle weakness earlier than

the untreated Y918C mice suggests that ICV injections may cause early trauma and neuromuscular

degeneration as compared to a mouse that has not gone through a surgery, anesthetization, etc. The

NCVs may also suggest that the treated Y918C mice still have some form of nerve damage in the sciatic

nerve, but that the consequences of such are not seen in the downstream femoral nerves.

Figure 24. Medial Gastrocs (MG) and Soleus' (Sol) of CBA.IGHMBP2 and P546.IGHMBP2 treated Y918C mice are not significantly different from +/+.
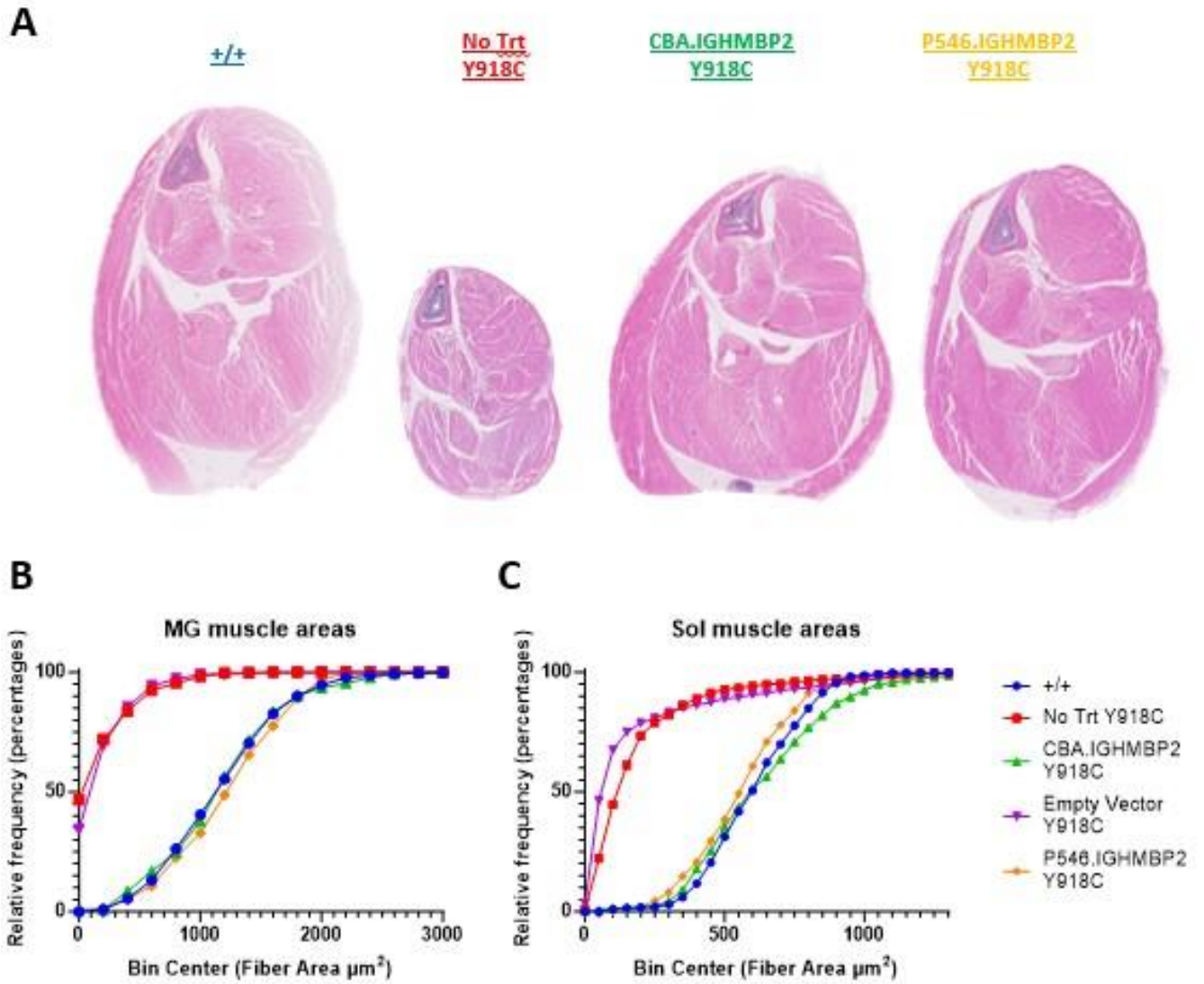
Figure 24. Medial Gastrocs (MG) and Soleus' (Sol) of CBA.IGHMBP2 and P546.IGHMBP2 treated Y918C mice are not significantly different from +/+. (a) At 16 weeks of age, cross sections of the hindlimb show that CBA.IGHMBP2 and P546.IGHMBP2 Y918C mice are much larger and overtly healthier than those of the untreated Y918C mice. (b) The cumulative frequency of the MG shows that +/+, CBA.IGHMBP2, and P546.IGHMBP2 mice are not significantly different from each other. Untreated and empty vector Y918C are not significantly different form each other. Means: +/+ = 1246μm +/-498 , Untreated Y918C = 238μm +/-277 , CBA.IGHMBP2 = 1243μm +/-536, Empty Vector Y918C = 253μm +/-254, P546.IGHMBP2= 1302μm +/-472). (c) The cumulative frequency of the Sol shows that +/+, CBA.IGHMBP2, and P546.IGHMBP2 mice are not significantly different from each other. Untreated and empty vector Y918C are not significantly different form each other. Means: +/+ = 625μm +/-181 , Untreated Y918C = 211μm +/-221 , CBA.IGHMBP2 = 653μm +/-247, Empty Vector Y918C = 195μm +/-276, P546.IGHMBP2= 586μm +/-205).

Figure 25. The Femoral Motor (FM) and Femoral Sensory (FS) Nerve axon counts show no significant difference between +/+, CBA.IGHMBP2, and P546.IGHMBP2 Y918C mice.
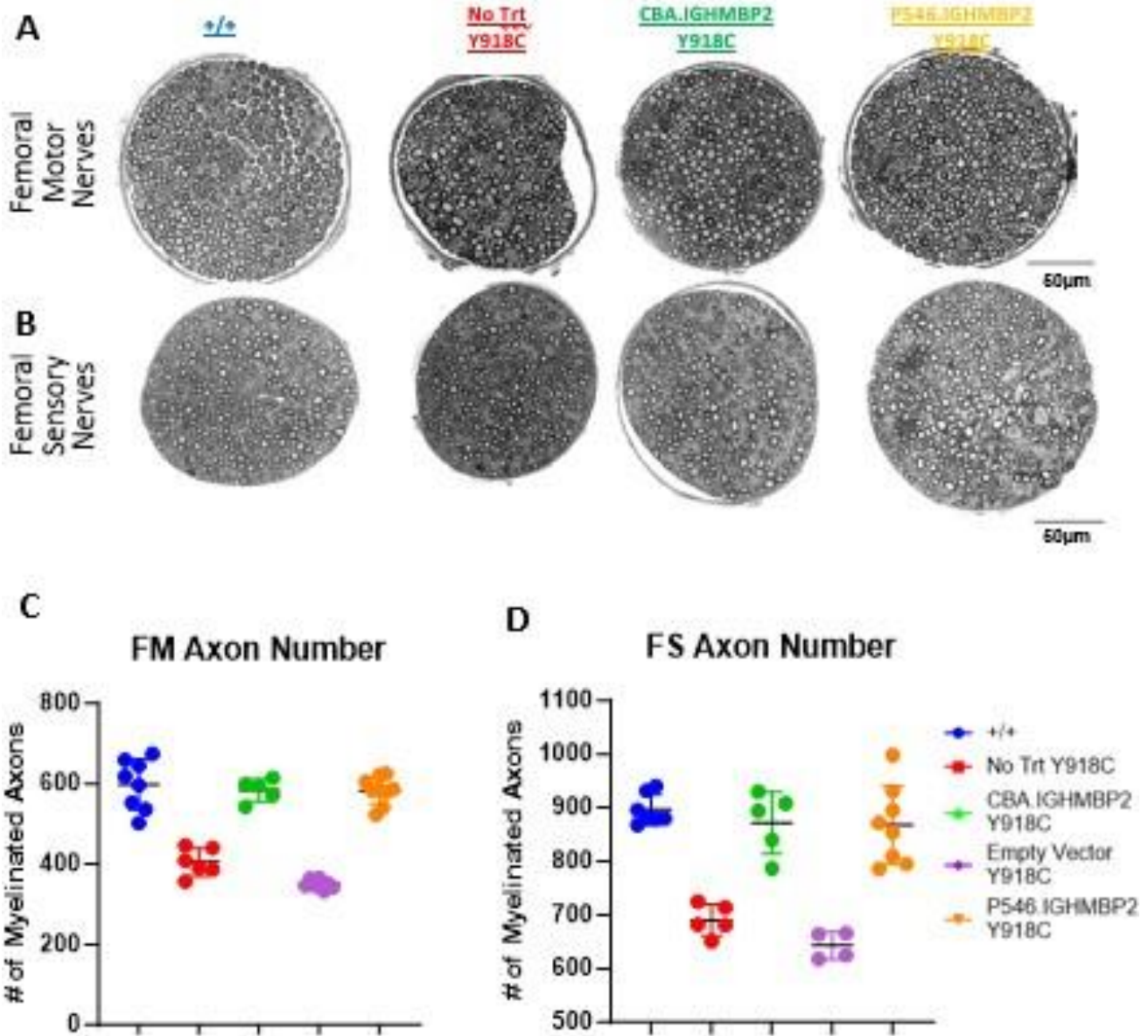
Figure 25. The Femoral Motor (FM) and Femoral Sensory (FS) Nerve axon counts show no significant difference between +/+, CBA.IGHMBP2, and P546.IGHMBP2 Y918C mice. (a) Cross sections of the FM show that CBA.IGHMBP2 and P546.IGHMBP2 treated animals are overtly more similar to +/+ mice than untreated Y918C mice. (b) Cross sections of the FS show that CBA.IGHMBP2 and P546.IGHMBP2 treated animals are overtly more similar to +/+ mice than untreated Y918C mice. (c) Quantification of the FM nerve show a significant myelinated axon count show no significant difference between +/+, CBA.IGHMBP2, and P546.IGHMBP2 mice. Untreated and empty vector Y918C mice are not significantly different from each other. Means: +/+ (N=8, 598+/-62), Untreated Y918C (N=6, 404+/-134), CBA.IGHMBP2 (N=5, 584+/-28), Empty Vector Y918C (N=8, 351+/-11),   P546.IGHMBP2 (N=9, 583 +/-34). (d) Quantification of the FS nerve show no significant myelinated axon count difference between +/+, CBA.IGHMBP2, and P546.IGHMBP2 animals. Means: +/+ (N=7, 897+/-28), Untreated Y918C (N=5,

4.3 Discussion:

From the trial data documenting longitudinal and end-of-life assays of neuromuscular health, it can be

observed that both vectors in both mouse models show significant improvement in all assays. However,

neither vector was able to completely rescue the SMARD1 phenotype in L362del mice still having lower

than normal femoral motor axon counts, lower neuromuscular junction [NMJ] occupancy, and lower

body weight than wild type mice. Due to the severity of the L362del mutation, the virus does not

activate (~1-2 week post injection) which is mid-onset. To study the impacts of a best case scenario, pre-

onset, we injected the same vectors in the less severe CMT2S model, C57Bl/6J-nmdCxY918C (hereafter

referred to as Y918C), which begins to show signs of paralysis between weeks 4 and 6. In this CMT2S

model, CBA.IGMHBP2 and P546.IGMHBP2 almost completely recover the phenotype except in the NCVs.

The CMT2S mouse model also show more does not show statistical variance between CBA.IGHMBP2 and

P546.IGHMBP2 treatment. Though the P546.IGHMBP2 has better overall results than the CBA.IGHMBP2

vector in the SMARD1 mice, the CBA.IGHMBP2 vector shows potential for regeneration of the nerves. In

the wirehang assay, the CBA.IGHMBP2 show the ability to comeback from a lack in strength and regain

it. The NMJs collected at 8 weeks show sign of sprouting and regeneration suggesting that though

nerves may start to deteriorate, the CBA.IGHMBP2 vector allows the nerves to grow back and

reinnervate the muscle. To determine the full potential of either virus, post-onset injections of the

CMT2S models are required to see if potential sprouting of the nerves may be seen even when most of the damage to the nerves has already been done.

Gene therapy trial studies that use an array of mouse models that better represent the spectrum of human patients along with a range of vectors and therapeutics are vital to growing the research space of therapies, especially for rare diseases. Using a holistic approach to study longitudinal with end of life assays and all aspects of the disease, in our case, from nerve to muscle, creates a clearer picture of the strength, weaknesses, and nuances of each therapy and will determine the best approach to human trials.

CHAPTER 5

Determining Disease Mechanisms in IGHMBP2 and NEMF Associated Diseases

IGHMBP2 and NEMF associated diseases share similar pathomechanisms

Sarah E. Holbrook[1,2,], Amy N. Hicks[1], Paige B. Martin[1], Jennifer E Stauffer[1], David G Schroeder[1], *Gregory A. Cox[1,2],

1. The Jackson Laboratory, Bar Harbor, ME, USA

2. The University of Maine, Orono, ME, USA

*Corresponding author:

The University of Maine, 168 College Ave., Orono, ME, USA

Telephone: 207-581-3071

Email: gregory.a.cox@maine.edu

Abstract

When deleterious mutations occur in IGHMBP2 or NEMF, they create a spectrum of neuromuscular diseases causing a range of symptoms such as muscular atrophy, neural degeneration, and shorter lifespans. Though they differ in some regards such as NEMF associated diseases having cognitive impacts and some IGHMBP2 associated diseases being heavily linked to respiratory distress, the mouse models of said diseases are overtly similar. Both genes are also associated with translation and ribosomes. Delving past overt phenotype, bulk RNAseq of the spinal cords of said mice also show significantly similar genetic profiles. The most prominent pathway seen in both diseased IGHMBP2 and NEMF mouse spinal cords is the RIG-I Like Receptor (RLR) pathway. The RLR pathway is an innate immune pathway that sense viral RNA causing an interferon response and eventual death of the infected cell(s). This suggests that deleterious mutations in IGHMBP2 and NEMF may cause a toxic build-up of RNA thus leading to the RLR response. Through extensive phenotyping of key RLR knock-outs in a IGHMBP2 disease model, it is seen that the RLR pathway may have a protective effect. Breeding of IGHMBP2 and NEMF models together also show that IGMHBP2 and NEMF have an indirect impact on each other in certain allelic combinations. Understanding the impact of the RLR pathway in neuromuscular disease as well as the relationship between IGHMBP2 and NEMF are vital steps in characterizing possible multigenetic diseases. This may also lead to new potential diagnoses and tests as well as therapeutics.

5.1 Introduction

The genetics of many rare diseases are found through clinicians documenting the inheritance of degeneration in a family, often consanguineous, and the inheritability of said condition throughout generations (Allouba et al., 2023; Fareed et al., 2017; Shawky et al., 2013). Through these studies, genes such as MYL2 and CSRP3 have been found to be the culprit in the disease (Allouba et al., 2023). With increased efficiency for whole exome and even genome sequencing including the introns, more deleterious mutations are being found every year (eClinicalMedicine, 2023). However, as it is with most traits such as eye color, rare diseases too can be multigenetic and faceted. Multiple genes lead to a similar phenotype, such as Charcot Marie Tooth Disease type 1 with *PMP22* and *MPZ* (Martin et al., 2023b). One gene can lead to a spectrum of phenotypes such as IGHMBP2 (Martin et al., 2023a, Grohmann et al., 1999; Grohmann et al., 2001, Grohmann et la., 2004; Schottmann et al., 2015) and, mutations in multiple genes can compound together and create a phenotype themselves that would have been seen if patients only had a mutation in one gene. Researchers are finding more and more digenic causes for disease such a skeletal muscle myopathy resulting from a mutation in *TTN* and *SRPK3* (Töpf et al., 2024), a version of Leigh Spectrum syndrome resulting from the digenic inheritance of deleterious copies of mitochondrial complex I genes and DNAJC30 (Blickhäuser et al., 2024), and two unrelated patients with deleterious variants in *TIA1* and *SQSTM1* resulting in distal myopathies (Bermejo-Guerrer et al., 2023). Cases such as these are important not only for diagnosis of rare diseases, but understanding the underlying mechanisms of said diseases. They allow for the differentiation of minute differences between diseases such as Leigh Spectrum syndrome primary Leber hereditary optic neuropathy (LHON) with LHON being isolated to the optic system and Leigh Spectrum syndrome being associated with widespread neuropathy of the body (Blickhäuser et al., 2024) though having mutations in similar sets of genes.

Understanding the relationships between these genes, diseases, and development also expose potential

therapeutic targets. Being able to target one pathway to remedy multiple associated diseases vs

monogenic gene therapies targeting one genetic category of diseases has a greater success of achieving

funding and reaching more patients.

Our lab has created multiple mouse models for various neuromuscular diseases. Our Nuclear Export

Mediated Factor (NEMF) mutant mice (Martin et al., 2020) (**Figure 26)** and our Immunoglobulin H mu

Binding Protein 2 (IGHMBP2) mutant mice (Martin et al., 2023a) (**Figure 27**) show similar spectrums and

phenotypes of mice. Besides overt phenotypic similarities of neurogenic muscular atrophy and neural

degeneration, we have recently found significant genetic and respiratory similarities and differences in

these mouse models.

Figure 26. Spectrum of Diseases: *Nemf* **Mouse Models**

Spectrum of Disease: NEMF *Mouse Models*

Strain Name	Lifespan	Human Equivalent
NEMF-null D106*	~11 days	Severe Motor Neuron disease
NEMF- R85Q (Human mutation), R86S	~3 week	Severe Motor Neuron disease
NEMF- CMT2S I98T (Human Mutation), R487G	~ Little or no impact	Mild Motor Neuron disease
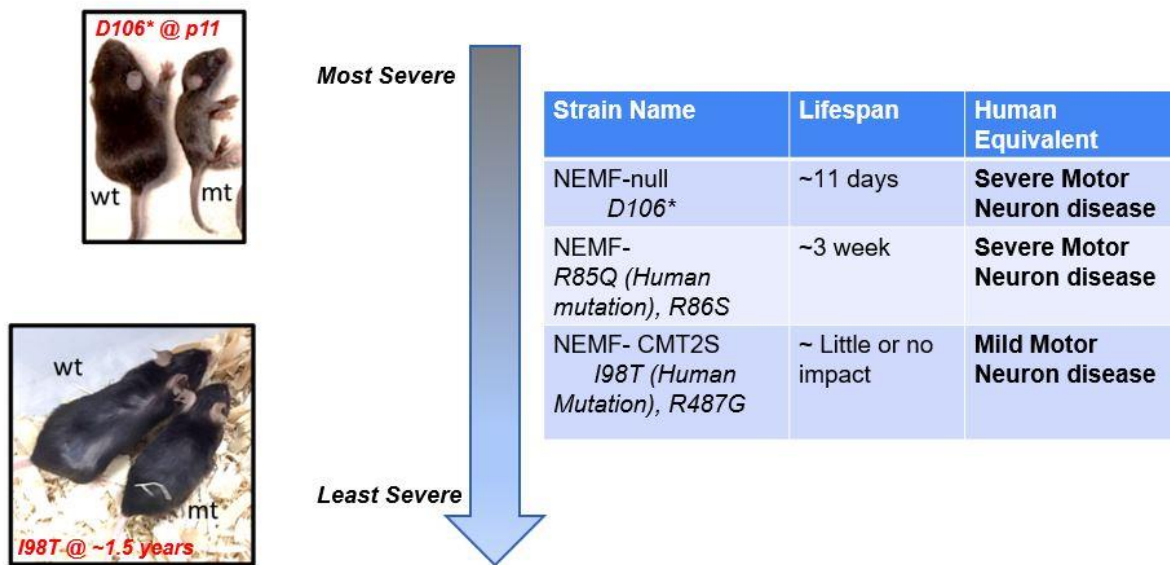
Figure 27. Spectrum of Diseases: *Ighmbp2* Mouse Models

Spectrum of Disease: IGHMBP2 *Mouse Models*

Strain Name	Lifespan	Human Equivalent
Ighmbp2-null EM4 (early stop codon)	A few hours after birth	**Sudden Infant Death Syndrome (SIDS)**
Ighmbp2- EM6 C495del (Human Mutation)	~1 week	**Less severe SIDS/ very severe SMARD1**
Ighmbp2-EM3 E362del	~3 weeks	**Severe Spinal Muscular Atrophy with Respiratory Distress (SMARD1)**
Ighmbp2- nmd^2J/2J Splicing mutation in intron 4	~3 months	**SMARD1**
Ighmbp2- CMT2S EM1, EM5 (Human mutation)	~ Little or no impact	**Charcot-Marie-Tooth Syndrome Type 2S (CMT2S)**

5.2 Results

5.2.1 Bulk RNAseq of the Spinal cords of IGHMBP2 and NEMF mice show significant overlap

An essential aspect of disease characterization is understanding the molecular causes of the disease.

Through previous research using transgenic mice (Maddatu et al., 2004), we know that the nerves are

primarily impacted in IGHMBP2 associated diseases, particularly the alpha motor neurons. Through past

characterization of NEMF mouse models, we also know the motor neurons are greatly impacted (Martin

et al., 2020). We collected lumbar spinal cords from 2 week old IGHMBP2.E365del (Martin et al., 2023a),

NEMF.I98T (Martin et al., 2020), and C57Bl/6J controls. Using stringent parameters of significance to

find only the most highly differentiated expressed genes (Fold Change(FC) >1 and FDR<1E-10), we found

a significant overlap in overexpressed genes in the IGHMBP2 and NEMF mice. (**Figure 28).** Within the

overlap of genes, through STRING analysis (Szklarczyk et al., 2019), we found that several interferon

pathways were overexpressed, most notably, the RIG-I Like Receptor (RLR) pathway (**Figure 28).**

Figure 28. Bulk RNAseq of lumbar spinal cords of 2 week old IGHMBP2.E365del, NEMF.I98T, and

C57Bl/6J controls show great overlap.

9330175E14Rik	Cd180	Eif2ak2	Gm4955	Ifit2	Lgals9	Oasl2	Rtp4	Trem2
AF251705	Cd22	Epsti1	Gpnmb	Ifit3	Ly6a	Parp12	S100a6	Trim12c
AI607873	Cd274	F830016B08Rik	H2-D1	Ifitm3	Ly86	Parp14	S1pr3	Trim25
Apol9a	Cd52	Fcgr2b	H2-K1	Igtp	Ly9	Parp9	Samd9l	Trim30a
Arl4d	Cd68	Fcgr3	H2-Q6	Iigp1	Lyz2	Phf11d	Serpina3n	Trim30d
B2m	Clec7a	Flnc	H2-Q7	Irf7	Mnda	Pik3ap1	Sgk1	Trim34a
Bst2	Csf2rb	Fyb	Herc6	Irf8	Mpeg1	Pld4	Slc15a3	Tyrobp
C1qa	Csf3r	Gbp2	Hk2	Irf9	Tap1	Mx1	Plek	Slfn2	Usp18
C1qb	Cst7	Gbp3	Hspa1b	Irgm1	Mx2	Ppl	Slfn8	Vim
C1qc	Ctss	Gbp5	I830012O16Rik	Irgm2	Myo1f	Psmb8	Slfn9	Xaf1
C3	Cxcl10	Gbp6	Ifi204	Isg15	NA	Ptprc	Sp110	Zbp1
C3ar1	Cxcl9	Gbp7	Ifi27	Itgax	Nlrc5	Ptx3	Stat1	Zc3hav1
C4b	Cybb	Gm12250	Ifi27l2a	Itgb2	Oas1a	Pydc4	Tgtp1	
Capn3	Ddx58	Gm1966	Ifi44	Lag3	Oas1b	Pyhin1	Tgtp2	
Ccl12	Ddx60	Gm26870	Ifi47	Laptm5	Oas1g	Rasal3	Timp1	
Ccl5	Dock2	Gm4841	Ifih1	Lgals3	Oas2	Rnf213	Tlr2	
Cd109	Dtx3l	Gm4951	Ifit1	Lgals3bp	Oasl1	Rsad2	Tor3a	

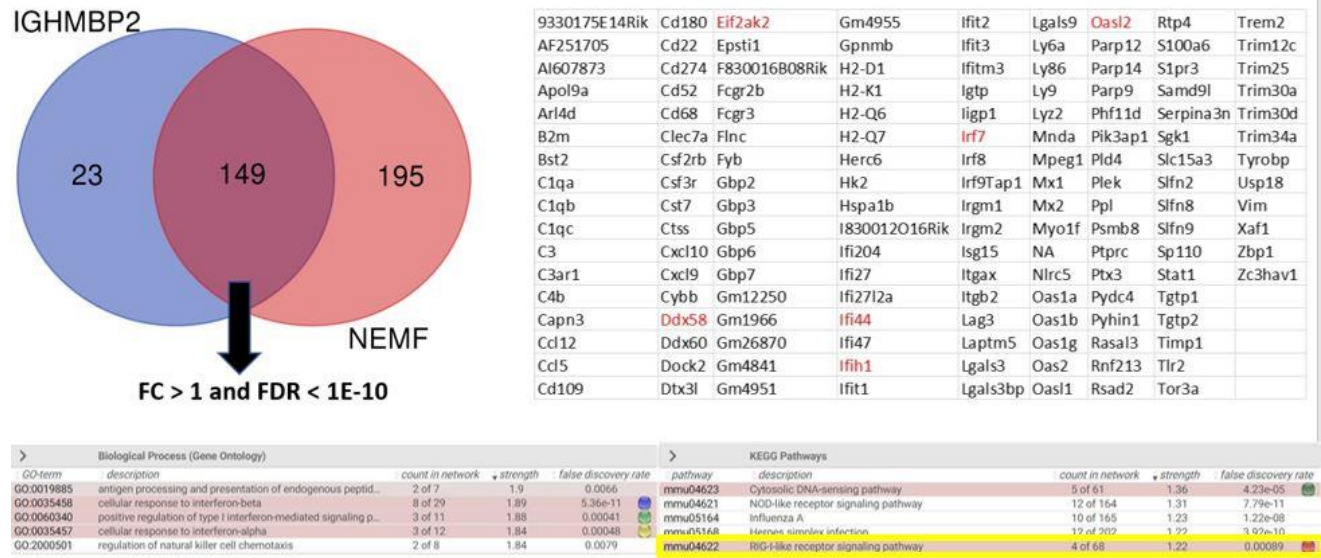|	Biological Process (Gene Ontology)					KEGG Pathways			
GO-term	description	count in network	strength	false discovery rate	pathway	description	count in network	strength	false discovery rate
GO:0019885	antigen processing and presentation of endogenous peptid...	2 of 7	1.9	0.0066	mmu04623	Cytosolic DNA-sensing pathway	5 of 61	1.36	4.23e-05
GO:0035458	cellular response to interferon-beta	8 of 29	1.89	5.36e-11	mmu04621	NOD-like receptor signaling pathway	12 of 164	1.31	7.79e-11
GO:0060340	positive regulation of type I interferon-mediated signaling p...	3 of 11	1.88	0.00041	mmu05164	Influenza A	10 of 165	1.23	1.22e-08
GO:0035457	cellular response to interferon-alpha	3 of 12	1.84	0.00048	mmu05168	Herpes simplex infection	12 of 202	1.22	3.92e-10
GO:2000501	regulation of natural killer cell chemotaxis	2 of 8	1.84	0.0079	mmu04622	RIG-I-like receptor signaling pathway	4 of 68	1.22	0.00089

Figure 28. Bulk RNAseq of lumbar spinal cords of 2 week old IGHMBP2.E365del, NEMF.I98T, and C57Bl/6J controls show great overlap. (a) Using stringent parameters of significance to find only the most highly differentiated expressed genes (Fold Change(FC) >1 and FDR<1E-10). Genes in overlap shown in table with key RLR pathway genes highlighted in red.(b) String analysis of genetic overlap reveals several generic immune system pathways and the RLR pathway are highly represented in dataset.

5.2.2 The RLR pathway impacts neural muscular degeneration in IGHMBP2 and NEMF mice

The RLR pathway is an immune system pathway that detects viral dsRNA and causes a cascade of Type I interferons and other genes to eliminate infection (Quicke at al., 2019; Zhu et al., 2014). Along with an interferon response that alarms the rest of the body of infection releasing interferon sensitive response elements and NF-kB, it proceeds to shutdown translation and eventually causes apoptosis of the infected cells. (**Supp. Fig. 13).** This cessation of translation and apoptosis provides a possible hypothesis of disease mechanism for IGHMBP2 and NEMF models. IGHMBP2 and NEMF have been associated with translation with IGHMBP2 most likely unwinding a small RNA substrates, perhaps tRNAs (de Planell-Saguer et al., 2009), due to its low processivity (Lim et al., 2012) and NEMF being associated with stalled ribosomes (Martin et al.,2020b, Shao et al., 2015) . If IGHMBP2 and NEMF are impacted, so would

translation. This may lead to a build-up of RNAs that cannot be processed causing the RLR pathway to wrongfully detect said RNAs as foreign.

To determine if the RLR pathway was being expressed in the motor neurons and thus potentially a cause of death or is being expressed by surrounding cells responding to the dying motor neurons, we conducted RNAscope on the spinal cords of IGHMBP2 mice. Through RNAscope, we tagged the RNA of three key genes in the RLR pathway, RIG-I, MDA5, and Oasl2. We determined that the RLR pathway is being expressed in the chat positive motor neurons. However, we also detected an unknown cell type(s) that also highly expresses the RLR pathway (**Figure 29).**

Figure 29. RNAscope of key RLR genes overlap with lumbar spinal motor neurons.
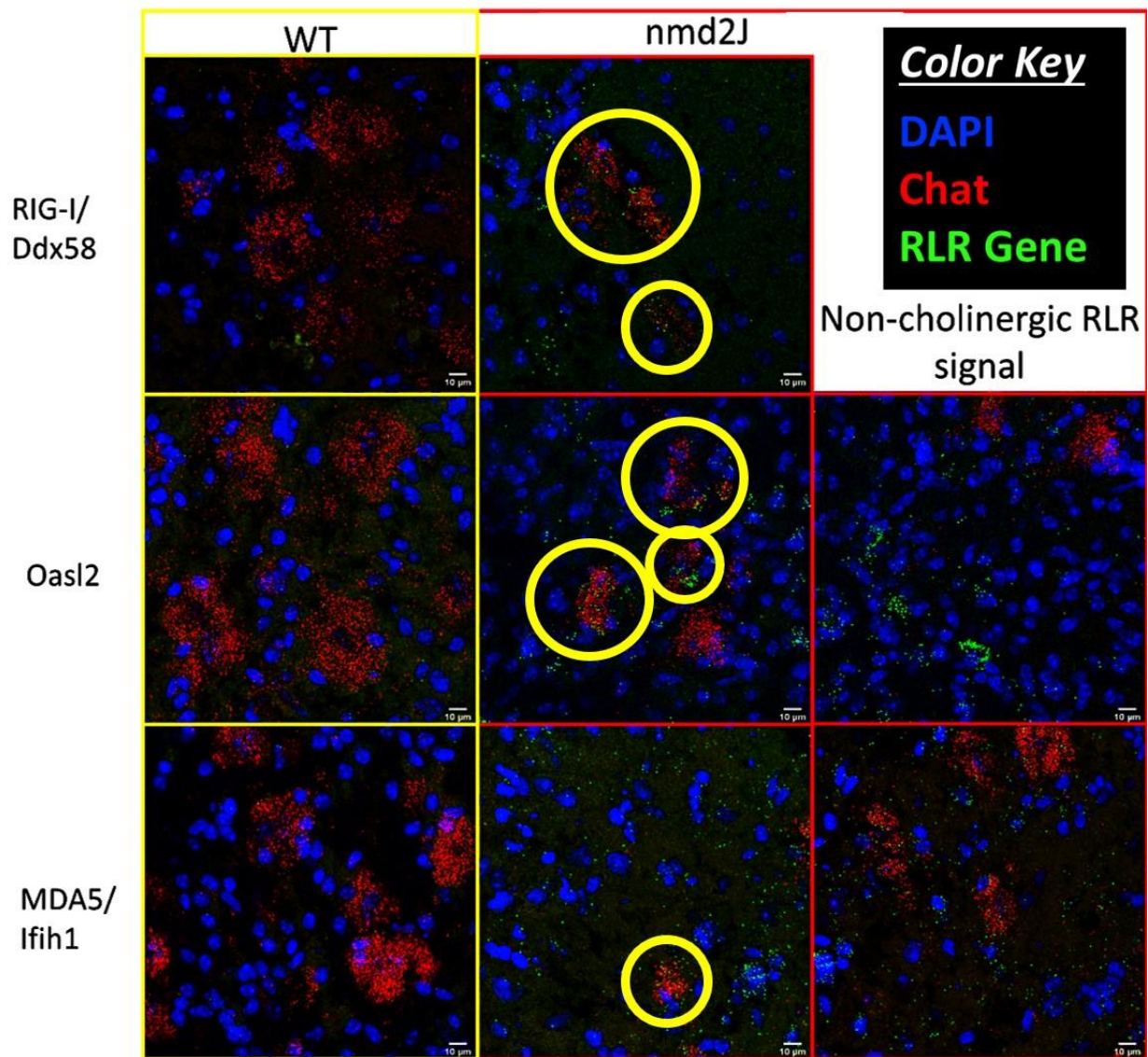
Figure 29. RNAscope of key RLR genes overlap with lumbar spinal motor neurons. Using RNAscope to tag the RNA of DDx58, Oasl2, and Ifih1 in the green channel, ChaT in red for the motor neurons, and DAPI in blue, the RLR pathay is shown to be highly expressed in the motor neurons as well as an unknown cell group(s). Yellow circles show overlap of RLR and CHaT signal, green circles show RLR expression in unknown cell type.

To determine if the RLR pathway impacts a neuromuscular phenotype, we knocked out key genes in the

RLR pathway in nmd2J mice to determine if they impacted the phenotype. We hypothesized that

knocking out the RLR pathway would have an ameliorative effect if it was the death mechanism.

However, we have seen that when we knock out most genes, there is no impact on lifespan. Two genes

had a detrimental impact; Oasl2 and Ifih1 (**Figure 30**). Oasl2 enables 2'-5'-oligoadenylate synthetase

activity and double-stranded RNA binding activity an acts upstream of IL27. Ifih1, or MDA5, is a key RNA

sensor and helicase in the RLR pathway that detects short double stranded RNAs (Quicke et al., 2019).

Figure 30. KO of key RLR genes in IGHMBP2 model, nmd2J, show limited impact on phenotype.
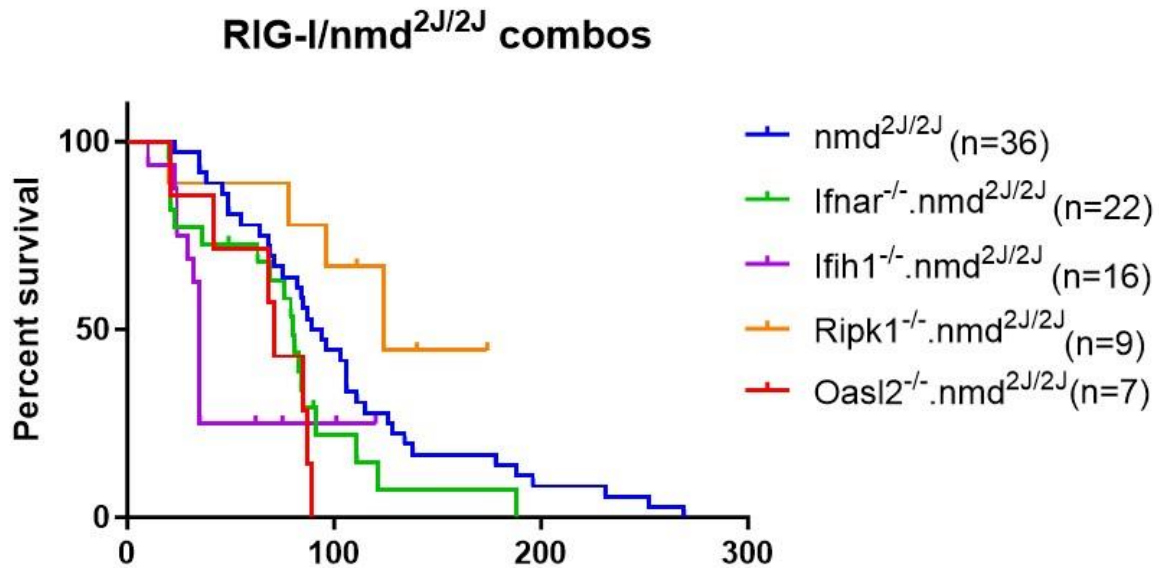
Figure 30. KO of key RLR genes in IGHMBP2 model, nmd2J, show limited impact on phenotype. Both KOs of Ifih1 and Oasl2 respectively show a significant detrimental impact on lifespan suggesting that these genes may play a protective role in IGHMBP2 associated neuromuscular disease. Kaplan-Meier test: (nmd2J vs Ifih1: p=0.0037; nmd2J vs Oasl2: p=0.0223).

5.2.3 IGHMBP2 and NEMF indirectly impact each other

IGHMBP2 and NEMF are similar in phenotype and gene expression in mouse models. From

immunoprecipitation assays, we know that IGHMBP2 and NEMF do not directly bind together, but have

both been precipitated in ribosome precipitation assays (de Planell-Saguer et al., 2009; Pisareva et al.,

2011; Shao et al., 2013). To determine if they may impact each other indirectly through similar pathways

and mechanisms, we bred mice to be heterozygous for mutations in IGHMBP2 and NEMF. Due to

IGHMBP2 and NEMF's recessive natures in neuromuscular disease, mice do not show a heterozygous

phenotype. However, when we used various combinations of IGHMBP2 and NEMF alleles, we see severe

neuromuscular disease phenotypes (**Figure 31).** The combinations required to see a neuromuscular

phenotype are a hypomorphic NEMF protein combined with either depleted levels of IGHMBP2 via the

IGHMBP2 null or a hypomorphic IGMHBP2 protein. A phenotype is not seen if you deplete NEMF via the

NEMF null (**Supp. Figure 14**). This suggests that mutated NEMF has a sub threshold toxic gain of effect

perhaps causing stalling or antagonistic binding of the ribosomes and that IGHMBP2 is rate limiting. We

also see that the phrenics of the IGHMBP2 x NEMF cross more closely resemble that of the IGHMBP2

mice than that of the NEMF further suggesting that IGHMBP2 is driving the neuromuscular disease

phenotype (**Figure 32).**

Figure 31. Lifespans of IGHMBP2 x NEMF crosses. (a) IGHMBP2-EM4 x NEMF-R85Q
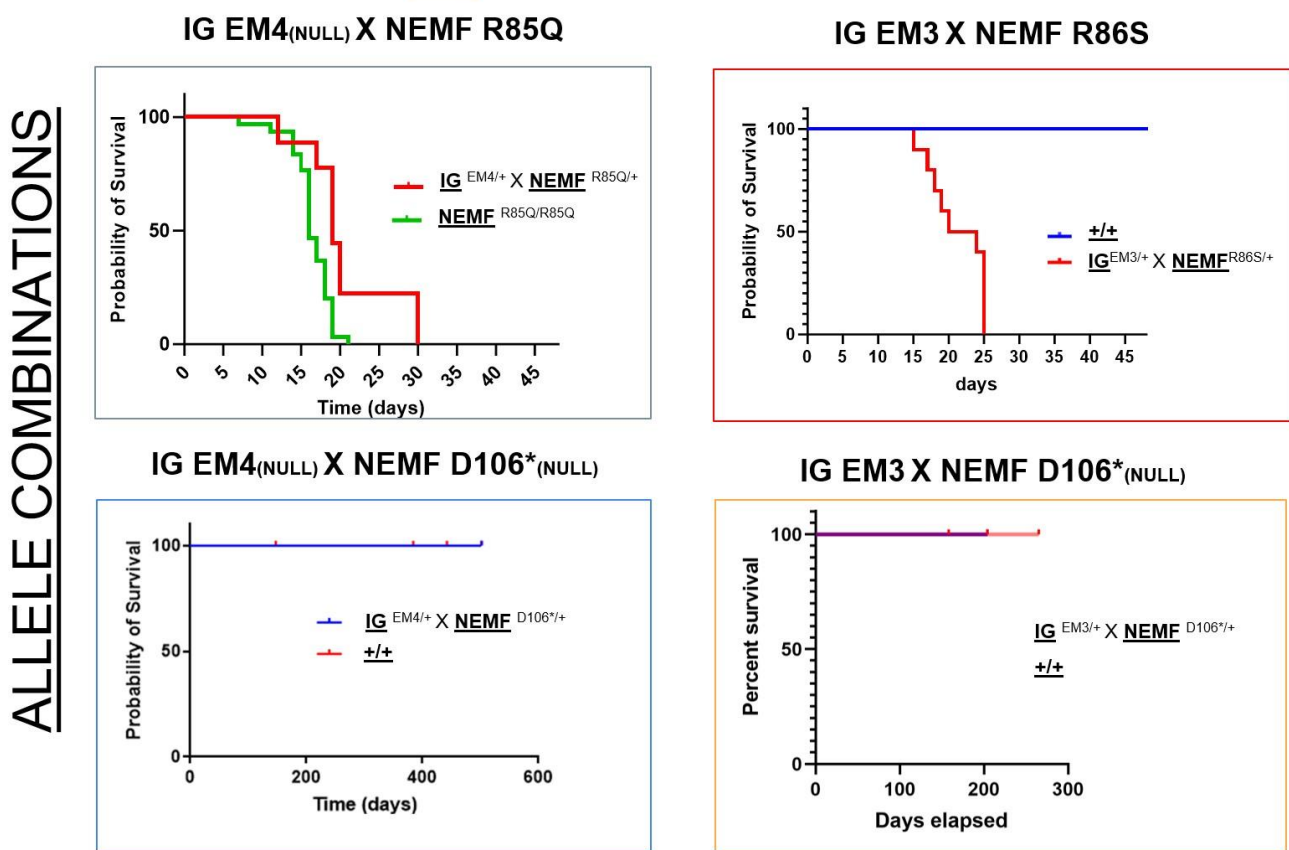
Figure 31. Lifespans of IGHMBP2 x NEMF crosses. (a) IGHMBP2-EM4 x NEMF-R85Q. There is a significant difference between NEMF-R85Q/R85Q (N=30) mice with a median lifespan of 16 days and double HET (N=19) mice with a median lifespan of 19 days (p=0.0026 Mattel-Cox test). (b) IGHMBP2-EM3 x NEMF-R86S. There is a significant difference between +/+ (N=4) and double HET (N=10) mice with a median survival of 22 days (p=0.0029 Mantel-Cox test).   (c) IGHMBP2-EM4 x NEMF-D106*. There is no significant difference in lifespan between +/+ (N=6) and double HET (N=5) mice. (d) IGHMBP2-EM3 x NEMF-D106*. There is no significant difference in lifespan between +/+ (N=6) and double HET (N=4) mice.

Figure 32. Phrenic nerves of IGHMBP2 x NEMF crosses.

Phrenic Axon Counts at 2 weeks
(unless stated otherwise underneath)
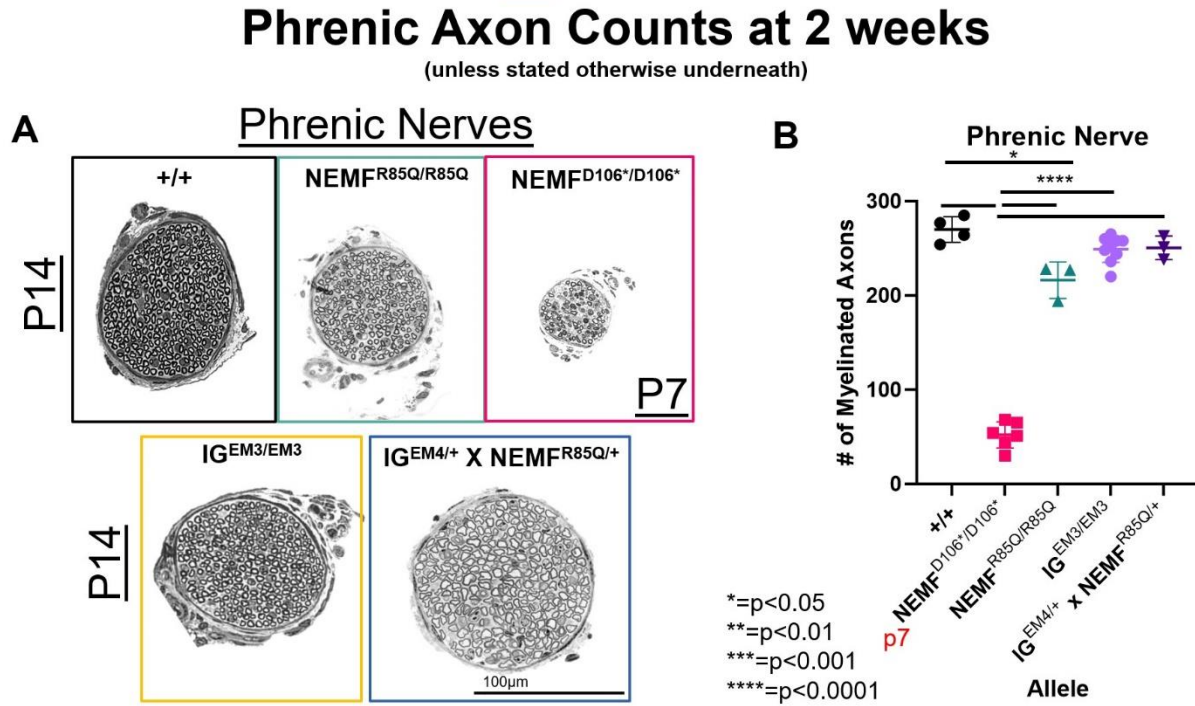
Figure 32. Phrenic nerves of IGHMBP2 x NEMF crosses. (a) Cross sections of the phrenic nerves of NEMF, IGHBP2, and IGMHBP2 x NEMF crosses. (b) Axon counts of NEMF mice are significantly less than those of +/+, IGHMBP2-EM3/EM3, or IGHMBP2-EM4/+ x NEMF-R85Q/+. NEMF-R85Q/R85Q is not singificantly different from IGHMBP2-EM3/EM3 or IGHMBP2-EM4/+ x NEMF-R85Q/+. Axon counts of +/+, IGHMBP2-EM3, or IGHMBP2-EM4/+ x NEMF-R85Q/+ show no significant different from each other. (+/+ vs NEMF-R85Q/R85Q: p=0.0112) (NEMF-D106*/D106* is significantly different from all other groups with p<0.0001). +/+ (N=4), NEMF-D106*/D106* (N=6), NEMF-R85Q/R85Q (N=3), IGHMBP2-EM3/EM3 (N=8), IGHMBP2-EM4/+ x NEMF-R85Q/+ (N=3).

5.3 Discussion

These results illustrate a novel grouping of neuromuscular diseases associated with the RLR pathway.

Though this study focused on inherited motor neuronopathies and their association with the RLR

pathway, Japanese Encephalitis Virus (JEV) and Chandipura, viral disease that cause paralysis, have also

been associated with the RLR pathway and more recently have shown that the RLR pathway (Soung et

al., 2018; Manocha et al., 2014) is highly upregulated in the motor neurons (Bhaskar et al., 2021). In the

case of these viruses, upon infection, it is found that motor neurons quickly die in a RIG-I-dependent

fashion via transcription factors pIRF-3 and pIRF-7 (Bhaskar et al., 2021). These viral diseases, along with the data we have shown above, suggest the RLR pathway may play a major role in motor neuron death in certain genetic and viral diseases. Due to the nature of the RLR pathway causing the cessation of translation and apoptosis, particularly through the RNAseL branch of the RLR pathway, it is possible that it causes the death of the motor neurons. However, with the KO of Ifih1 causing a decrease in lifespan of the nmd-2J mouse model mutants, the RLR pathway may prove protective of a secondary mechanism. qPCR of the Ifih1 mice is necessary to determine if the RLR pathway is still highly upregulated. If it is not, RNAseq of these KO mice may reveal the true cause of the disease mechanism. If the RLR pathway is still highly upregulated, then this may reveal a complex relationship between the different branches of the RLR pathway that may be agonistic or antagonistic with other branches in the case of IGHMBP2 and NEFM associated disease.

Further studies of how the RLR pathway interacts with motor neurons is key to pinpointing the disease mechanism and potential therapies. Though JEV, Chandipura, NEMF, and IGHMBP2 share similarities, future experiments are needed to elaborate the potential role of glial cells (as seen in JEV and Chandipura) and if certain therapeutics may assist with both genetic and viral motor neuron degeneration or if they must be approached differently due to the nature of the induction of the RLR pathway in the motor neurons.

Acknowledgements

Conflicts of Interest

The authors have no conflicts to report.

BIBLIOGRAPHY

Allouba, M., Walsh, R., Afify, A., Hosny, M., Halawa, S., Galal, A., Fathy, M., Theotokis, P. I., Boraey, A., Ellithy, A., Buchan, R., Govind, R., Whiffin, N., Anwer, S., ElGuindy, A., Ware, J. S., Barton, P. J. R., Yacoub, M., & Aguib, Y. (2023). Ethnicity, consanguinity, and genetic architecture of hypertrophic cardiomyopathy. European Heart Journal, 44(48), 5146-5158. https://doi.org/10.1093/eurheartj/ehad372

Bhaskar M, Mukherjee S, Basu A. Involvement of RIG-I Pathway in Neurotropic Virus-Induced Acute Flaccid Paralysis and Subsequent Spinal Motor Neuron Death. mBio. 2021 Dec 21;12(6):e0271221. doi: 10.1128/mBio.02712-21. Epub 2021 Nov 16. PMID: 34781742; PMCID: PMC8593677.

Bennett, C. L., Dastidar, S. G., Ling, S. C., Malik, B., Ashe, T., Wadhwa, M., Miller, D. B., Lee, C., Mitchell, M. B., van Es, M. A., Grunseich, C., Chen, Y., Sopher, B. L., Greensmith, L., Cleveland, D. W., & La Spada, A. R. (2018). Senataxin mutations elicit motor neuron degeneration phenotypes and yield TDP-43 mislocalization in ALS4 mice and human patients. *Acta Neuropathologica*, *136*(3), 425–443. https://doi.org/10.1007/s00401-018-1852-9

Bermejo-Guerrero L, de Fuenmayor Fernández-de la Hoz CP, González-Quereda L, Segarra-Casas A, Nedkova V, Gallano P, Martín-Jiménez P, Hernández-Laín A, Olivé M, Arteche-López A, Domínguez-González C. Distal myopathy due to digenic inheritance of TIA1 and SQSTM1 variants in two unrelated Spanish patients. Neuromuscul Disord. 2023 Dec;33(12):983-987. doi: 10.1016/j.nmd.2023.10.016. Epub 2023 Oct 30. PMID: 38016875.

Blickhäuser B, Stenton SL, Neuhofer CM, Floride E, Nesbitt V, Fratter C, Koch J, Kauffmann B, Catarino C, Schlieben LD, Kopajtich R, Carelli V, Sadun AA, McFarland R, Fang F, La Morgia C, Paquay S, Nassogne MC, Ghezzi D, Lamperti C, Wortmann S, Poulton J, Klopstock T, Prokisch H. Digenic Leigh syndrome on the background of the m.11778G>A Leber hereditary optic neuropathy variant. Brain. 2024 Mar 13:awae057. doi: 10.1093/brain/awae057. Epub ahead of print. PMID: 38478578.

Bogdanik, L. P., Sleigh, J. N., Tian, C., Samuels, M. E., Bedard, K., Seburn, K. L., & Burgess, R. W. (2013). Loss of the E3 ubiquitin ligase LRSAM1 sensitizes peripheral axons to degeneration in a mouse model of Charcot-Marie-Tooth disease. *Disease Models & Mechanisms*, *6*(3), 780–792. https://doi.org/10.1242/dmm.010942

Campuzano O, Beltramo P, Fernandez A, Iglesias A, García L, Allegue C, Sarquella-Brugada G, Coll M, Perez-Serra A, Mademont-Soler I, Mates J, Del Olmo B, Rodríguez Á, Maciel N, Puigmulé M, Pico F, Cesar S, Brugada J, Cuesta A, Gutierrez C, Brugada R. Molecular autopsy in a cohort of infants died suddenly at rest. Forensic Sci Int Genet. 2018 Nov;37:54-63. doi: 10.1016/j.fsigen.2018.07.023. Epub 2018 Jul 31. PMID: 30086531.

Chaplan, S. R., Bach, F. W., Pogrel, J. W., Chung, J. M., & Yaksh, T. L. (1994). Quantitative assessment of tactile allodynia in the rat paw. *Journal of Neuroscience Methods*, *53*(1), 55–63. https://doi.org/10.1016/0165-0270(94)90144-9

Chen TH, Koh KY, Lin KM, Chou CK. Mitochondrial Dysfunction as an Underlying Cause of Skeletal Muscle Disorders. Int J Mol Sci. 2022 Oct 26;23(21):12926. doi: 10.3390/ijms232112926. PMID: 36361713; PMCID: PMC9653750.

Choudhury SR, Fitzpatrick Z, Harris AF, Maitland SA, Ferreira JS, Zhang Y, Ma S, Sharma RB, Gray-Edwards HL, Johnson JA, et al. (2016). In Vivo Selection Yields AAV-B1 Capsid for Central Nervous System and Muscle Gene Therapy. Mol Ther 24, 1247–1257. 10.1038/mt.2016.84.

Cottenie E, Kochanski A, Jordanova A, Bansagi B, Zimon M, Horga A, Jaunmuktane Z, Saveri P, Rasic VM, Baets J, Bartsakoulia M, Ploski R, Teterycz P, Nikolic M, Quinlivan R, Laura M, Sweeney MG, Taroni F, Lunn MP, Moroni I, Gonzalez M, Hanna MG, Bettencourt C, Chabrol E, Franke A, von Au K, Schilhabel M, Kabzińska D, Hausmanowa-Petrusewicz I, Brandner S, Lim SC, Song H, Choi BO, Horvath R, Chung KW, Zuchner S, Pareyson D, Harms M, Reilly MM, Houlden H. Truncating and missense mutations in IGHMBP2 cause Charcot-Marie Tooth disease type 2. Am J Hum Genet. 2014 Nov 6;95(5):590-601. doi: 10.1016/j.ajhg.2014.10.002. Epub 2014 Oct 30. PMID: 25439726; PMCID: PMC4225647.

Cottenie, E., Kochanski, A., Jordanova, A., Bansagi, B., Zimon, M., Horga, A., Jaunmuktane, Z., Saveri, P., Rasic, V. M., Baets, J., Bartsakoulia, M., Ploski, R., Teterycz, P., Nikolic, M., Quinlivan, R., Laura, M., Sweeney, M. G., Taroni, F., Lunn, M. P., … Houlden, H. (2014). Truncating and Missense Mutations in IGHMBP2 Cause Charcot-Marie Tooth Disease Type 2. *The American Journal of Human Genetics*, *95*(5), 590–601. https://doi.org/10.1016/j.ajhg.2014.10.002

Cox GA, Mahaffey CL, Frankel WN. Identification of the mouse neuromuscular degeneration gene and mapping of a second site suppressor allele. Neuron. 1998 Dec;21(6):1327-37. doi: 10.1016/s0896-6273(00)80652-2. PMID: 9883726.Joseph et al., 2009)

Danastas, K., Miranda-Saksena, M., & Cunningham, A. L. (2020). Herpes simplex virus type 1 interactions with the interferon system. International Journal of Molecular Sciences, 21(14), 5150. https://doi.org/10.3390/ijms21145150de Planell-Saguer M, Schroeder DG, Rodicio MC, Cox GA, Mourelatos Z. Biochemical and genetic evidence for a role of IGHMBP2 in the translational machinery. Hum Mol Genet. 2009 Jun 15;18(12):2115-26. doi: 10.1093/hmg/ddp134. Epub 2009 Mar 19. PMID: 19299493; PMCID: PMC2685751.

De Vos KJ, Hafezparast M. Neurobiology of axonal transport defects in motor neuron diseases: Opportunities for translational research? Neurobiol Dis. 2017 Sep;105:283-299. doi: 10.1016/j.nbd.2017.02.004. Epub 2017 Feb 22. PMID: 28235672; PMCID: PMC5536153.

Duque S, Joussemet B, Riviere C, Marais T, Dubreil L, Douar AM, Fyfe J, Moullier P, Colle MA, Barkats M. Intravenous administration of self-complementary AAV9 enables transgene delivery to adult motor neurons. Mol Ther. 2009 Jul;17(7):1187-96. doi: 10.1038/mt.2009.71. Epub 2009 Apr 14. PMID: 19367261; PMCID: PMC2835208.

eClinicalMedicine. Raising the voice for rare diseases: under the spotlight for equity. EClinicalMedicine. 2023 Mar 24;57:101941. doi: 10.1016/j.eclinm.2023.101941. PMID: 37064509; PMCID: PMC10102897.

Eskildsen S, Hartmann R, Kjeldgaard NO, Justesen J . Gene structure of the murine 2'-5'-oligoadenylate synthetase family. Cell Mol Life Sci 2002; 59: 1212–1222.

Ezelle, H. J., & Hassel, B. A. (2012). Pathologic effects of RNase-L dysregulation in immunity and proliferative control. Frontiers in Bioscience (Scholar Edition), 4, 767

Fareed, M., & Afzal, M. (2017). Genetics of consanguinity and inbreeding in health and disease. Annals of Human Biology, 44(2), 99-107. https://doi.org/10.1080/03014460.2016.1265148

Feng G, Mellor RH, Bernstein M, Keller-Peck C, Nguyen QT, Wallace M, Nerbonne JM, Lichtman JW, Sanes JR. Imaging neuronal subsets in transgenic mice expressing multiple spectral variants of GFP. Neuron. 2000 Oct;28(1):41-51. doi: 10.1016/s0896-6273(00)00084-2. PMID: 11086982.

Ferrari S, Di Iorio E, Barbaro V, Ponzin D, Sorrentino FS, Parmeggiani F. Retinitis pigmentosa: genes and disease mechanisms. Curr Genomics. 2011 Jun;12(4):238-49. doi: 10.2174/138920211795860107. PMID: 22131869; PMCID: PMC3131731.

Gonzalez, M. A., Feely, S. M., Speziani, F., Strickland, A. V., Danzi, M., Bacon, C., Lee, Y., Chou, T. F., Blanton, S. H., Weihl, C. C., Zuchner, S., & Shy, M. E. (2014). A novel mutation in VCP causes Charcot-Marie-Tooth Type 2 disease. *Brain*, *137*(11), 2897–2902. https://doi.org/10.1093/brain/awu224

Gray SJ, Matagne V, Bachaboina L, Yadav S, Ojeda SR, Samulski RJ. Preclinical differences of intravascular AAV9 delivery to neurons and glia: a comparative study of adult mice and nonhuman primates. Mol Ther. 2011 Jun;19(6):1058-69. doi: 10.1038/mt.2011.72. Epub 2011 Apr 12. PMID: 21487395; PMCID: PMC3129805.

Grohmann K, Rossoll W, Kobsar I, Holtmann B, Jablonka S, Wessig C, Stoltenburg-Didinger G, Fischer U, Hübner C, Martini R, Sendtner M. Characterization of Ighmbp2 in motor neurons and implications for the pathomechanism in a mouse model of human spinal muscular atrophy with respiratory distress type 1 (SMARD1). Hum Mol Genet. 2004 Sep 15;13(18):2031-42. doi: 10.1093/hmg/ddh222. Epub 2004 Jul 21. PMID: 15269181.

Grohmann K, Schuelke M, Diers A, Hoffmann K, Lucke B, Adams C, Bertini E, Leonhardt-Horti H, Muntoni F, Ouvrier R, Pfeufer A, Rossi R, Van Maldergem L, Wilmshurst JM, Wienker TF, Sendtner M, Rudnik-Schöneborn S, Zerres K, Hübner C. Mutations in the gene encoding immunoglobulin mu-binding protein 2 cause spinal muscular atrophy with respiratory distress type 1. Nat Genet. 2001 Sep;29(1):75-7. doi: 10.1038/ng703. PMID: 11528396.

Grohmann K., Wienker T.F., Saar K., Rudnik-Schoneborn S., Stoltenburg-Didinger G., Rossi R. Diaphragmatic spinal muscular atrophy with respiratory distress is heterogeneous, and one form is linked to chromosome 11q13–q21. Am J Hum Genet. 1999;65(5):1459–1462.

Guenther UP, Handoko L, Varon R, Stephani U, Tsao CY, Mendell JR, Lützkendorf S, Hübner C, von Au K, Jablonka S, Dittmar G, Heinemann U, Schuetz A, Schuelke M. Clinical variability in distal spinal muscular atrophy type 1 (DSMA1): determination of steady-state IGHMBP2 protein levels in five patients with

infantile and juvenile disease. J Mol Med (Berl). 2009 Jan;87(1):31-41. doi: 10.1007/s00109-008-0402-7. Epub 2008 Sep 18. PMID: 18802676.

Hamilton, M. J., Longman, C., O'Hara, A., Kirkpatrick, M., & McWilliam, R. (2015). Growing up with spinal muscular atrophy with respiratory distress (SMARD1). *Neuromuscular Disorders*, *25*(2), 169–171. https://doi.org/10.1016/j.nmd.2014.10.005

Jablonka S, Yildirim E. Disease Mechanisms and Therapeutic Approaches in SMARD1-Insights from Animal Models and Cell Models. Biomedicines. 2024 Apr 11;12(4):845. doi: 10.3390/biomedicines12040845. PMID: 38672198; PMCID: PMC11048220.

Jackson L, Madan-Khetarpal S, Naik M, Michaels MG, Riley M. Infant Botulism in the Very Young Neonate: A Case Series. AJP Rep. 2017 Jul;7(3):e163-e166. doi: 10.1055/s-0037-1604407. Epub 2017 Jul 31. PMID: 28765793; PMCID: PMC5536996.

James, P. A., Cader, M. Z., Muntoni, F., Childs, A.-M., Crow, Y. J., & Talbot, K. (2006). Severe childhood SMA and axonal CMT due to anticodon binding domain mutations in the GARS gene. *Neurology*, *67*(9), 1710–1712. https://doi.org/10.1212/01.wnl.0000242619.52335.bc

Joseph S, Robb SA, Mohammed S, Lillis S, Simonds A, Manzur AY, Walter S, Wraige E. Interfamilial phenotypic heterogeneity in SMARD1. Neuromuscul Disord. 2009 Mar;19(3):193-5. doi: 10.1016/j.nmd.2008.11.013. Epub 2009 Jan 20. PMID: 19157874.

Kazamel M, Boes CJ. Charcot Marie Tooth disease (CMT): historical perspectives and evolution. J Neurol. 2015;262(4):801-5. doi: 10.1007/s00415-014-7490-9. Epub 2014 Sep 9. PMID: 25201224.

Kim YA, Jin HY, Kim YM. Diagnostic Odyssey and Application of Targeted Exome Sequencing in the Investigation of Recurrent Infant Deaths in a Syrian Consanguineous Family: a Case of Spinal Muscular Atrophy with Respiratory Distress Type 1. J Korean Med Sci. 2019 Feb 7;34(9):e54. doi: 10.3346/jkms.2019.34.e54. PMID: 30863264; PMCID: PMC6406039.

Laurá, M., Pipis, M., Rossor, A. M., & Reilly, M. M. (2019). Charcot-marie-Tooth disease and related disorders: An evolving landscape. *Current Opinion in Neurology*, *32*(5), 641–650. https://doi.org/10.1097/WCO.0000000000000735

Li, Y., Banerjee, S., Goldstein, S. A., Dong, B., Gaughan, C., Rath, S., Donovan, J., Korennykh, A., Silverman, R. H., & Weiss, S. R. (2017). Ribonuclease L mediates the cell-lethal phenotype of double-stranded RNA editing enzyme ADAR1 deficiency in a human cell line. Elife, 6https://doi.org/10.7554/eLife.25687

Li C, Wu S, Albright B, Hirsch M, Li W, Tseng YS, Agbandje-McKenna M, McPhee S, Asokan A, and Samulski RJ (2016). Development of Patient-specific AAV Vectors After Neutralizing Antibody Selection for Enhanced Muscle Gene Transfer. Mol Ther 24, 53–65. 10.1038/mt.2015.134.

Lim, S. C., Bowler, M. W., Lai, T. F., & Song, H. (2012). The Ighmbp2 helicase structure reveals the molecular basis for disease-causing mutations in DMSA1. *Nucleic Acids Research*, *40*(21), 11009–11022. https://doi.org/10.1093/nar/gks792

Lingappa L, Shah N, Motepalli AS, Shaik F. Spinal muscular atrophy with respiratory distress syndrome (SMARD1): Case report and review of literature. Ann Indian Acad Neurol. 2016 Jul-Sep;19(3):395-8. doi: 10.4103/0972-2327.168635. PMID: 27570397; PMCID: PMC4980968.

Liu, L., Li, X., Hu, Z., Mao, X., Zi, X., Xia, K., Tang, B., & Zhang, R. (2017). IGHMBP2-related clinical and genetic features in a cohort of Chinese Charcot–Marie–Tooth disease type 2 patients. *Neuromuscular Disorders*, *27*(2), 193–199. https://doi.org/10.1016/j.nmd.2016.11.008

Maddatu, T. P., Garvey, S. M., Schroeder, D. G., Hampton, T. G., & Cox, G. a. (2004). Transgenic rescue of neurogenic atrophy in the nmd mouse reveals a role for Ighmbp2 in dilated cardiomyopathy. *Human Molecular Genetics*, *13*(11), 1105–1115. https://doi.org/10.1093/hmg/ddh129

Manocha, G.D., Mishra, R., Sharma, N. et al. Regulatory role of TRIM21 in the type-I interferon pathway in Japanese encephalitis virus-infected human microglial cells. J Neuroinflammation 11, 24 (2014). https://doi.org/10.1186/1742-2094-11-24

Martin P.B., Holbrook SE, Hicks AN, Hines TJ, Bogdanik LP, Burgess RW, Cox GA. Clinically relevant mouse models of Charcot-Marie-Tooth type 2S. Hum Mol Genet. 2023 Apr 6;32(8):1276-1288. doi: 10.1093/hmg/ddac283. PMID: 36413117; PMCID: PMC10077500.

Martin, PB., Hicks, A. N., Holbrook, S. E., & Cox, G. A. (2020). Overlapping spectrums: The clinicogenetic commonalities between Charcot-Marie-Tooth and other neurodegenerative diseases. *Brain Research*, *1727*(October 2019), 146532. https://doi.org/10.1016/j.brainres.2019.146532

Martin, P.B., Kigoshi-Tansho, Y., Sher, R.B. et al. NEMF mutations that impair ribosome-associated quality control are associated with neuromuscular disease. Nat Commun 11, 4625 (2020b). https://doi.org/10.1038/s41467-020-18327-6

Mead, R.J., Shan, N., Reiser, H.J. et al. Amyotrophic lateral sclerosis: a neurodegenerative disorder poised for successful therapeutic translation. Nat Rev Drug Discov 22, 185–212 (2023). https://doi.org/10.1038/s41573-022-00612-2

McCarty, Douglas. (2008). McCarty, DM. Self-complementary AAV vectors; advances and applications. Mol Ther 16: 1648-1656. Molecular therapy : the journal of the American Society of Gene Therapy. 16. 1648-56. 10.1038/mt.2008.171.

Morales L, Gambhir Y, Bennett J, and Stedman HH (2020). Broader Implications of Progressive Liver Dysfunction and Lethal Sepsis in Two Boys following Systemic High-Dose AAV. Mol Ther 28, 1753–1755. 10.1016/j.ymthe.2020.07.009.

Nizzardo, M., Simone, C., Rizzo, F., Salani, S., Dametti, S., Rinchetti, P., Bo, R. Del, Foust, K., Kaspar, B. K., Bresolin, N., Comi, G. P., & Corti, S. (2015). Gene therapy rescues disease phenotype in a spinal muscular atrophy with respiratory distress type 1 (SMARD1) mouse model. March, 1–10. https://doi.org/10.1126/sciadv.1500078

Nonnenmacher M, Wang W, Child MA, Ren XQ, Huang C, Ren AZ, Tocci J, Chen Q, Bittner K, Tyson K, et al. (2021). Rapid evolution of blood-brain-barrier-penetrating AAV capsids by RNA-driven biopanning. Mol Ther Methods Clin Dev 20, 366–378. 10.1016/j.omtm.2020.12.006.

Paul, A., Tang, T. H., & Ng, S. K. (2018). Interferon regulatory factor 9 structure and regulation. Frontiers in Immunology, 9, 1831-1831. https://doi.org/10.3389/fimmu.2018.01831

Pisareva, V. P., Skabkin, M. A., Hellen, C. U. T., Pestova, T. V. & Pisarev, A. V. Dissociation by Pelota, Hbs1 and ABCE1 of mammalian vacant 80S ribosomes and stalled elongation complexes. EMBO J. 30, 1804–1817 (2011).

Pitt M, Houlden H, Jacobs J, Mok Q, Harding B, Reilly M, Surtees R. Severe infantile neuropathy with diaphragmatic weakness and its relationship to SMARD1. Brain. 2003 Dec;126(Pt 12):2682-92. doi: 10.1093/brain/awg278. Epub 2003 Sep 23. PMID: 14506069.

Powers S, Likhite S, Gadalla KK, Miranda CJ, Huffenberger AJ, Dennys C, Foust KD, Morales P, Pierson CR, Rinaldi F, Perry S, Bolon B, Wein N, Cobb S, Kaspar BK, Meyer KC. Novel MECP2 gene therapy is effective in a multicenter study using two mouse models of Rett syndrome and is safe in non-human primates. Mol Ther. 2023 Sep 6;31(9):2767-2782. doi: 10.1016/j.ymthe.2023.07.013. Epub 2023 Jul 22. PMID: 37481701; PMCID: PMC10492029.

Preibisch S, Saalfeld S, Tomancak P. Globally optimal stitching of tiled 3D microscopic image acquisitions. Bioinformatics. 2009 Jun 1;25(11):1463-5. doi: 10.1093/bioinformatics/btp184. Epub 2009 Apr 3. PMID: 19346324; PMCID: PMC2682522.

Quicke KM, Kim KY, Horvath CM, Suthar MS. RNA Helicase LGP2 Negatively Regulates RIG-I Signaling by Preventing TRIM25-Mediated Caspase Activation and Recruitment Domain Ubiquitination. J Interferon Cytokine Res. 2019 Nov;39(11):669-683. doi: 10.1089/jir.2019.0059. Epub 2019 Jun 25. PMID: 31237466; PMCID: PMC6820871

Raj D, Davidoff AM, Nathwani AC. Self-complementary adeno-associated viral vectors for gene therapy of hemophilia B: progress and challenges. Expert Rev Hematol. 2011 Oct;4(5):539-49. doi: 10.1586/ehm.11.48. PMID: 21939421; PMCID: PMC3200187.

Scheiper S, Ramos-Luis E, Blanco-Verea A, Niess C, Beckmann BM, Schmidt U, Kettner M, Geisen C, Verhoff MA, Brion M, Kauferstein S. Sudden unexpected death in the young - Value of massive parallel sequencing in postmortem genetic analyses. Forensic Sci Int. 2018 Dec;293:70-76. doi: 10.1016/j.forsciint.2018.09.034. Epub 2018 Oct 26. PMID: 30415094.

Schottmann G., Jungbluth H., Schara U., Knierim E., Morales Gonzalez S., Gill E. Recessive truncating IGHMBP2 mutations presenting as axonal sensorimotor neuropathy. Neurology. 2015;84(5):523–531.

Schneider CA, Rasband WS, Eliceiri KW. NIH Image to ImageJ: 25 years of image analysis. Nat Methods. 2012 Jul;9(7):671-5. doi: 10.1038/nmeth.2089. PMID: 22930834; PMCID: PMC5554542.

Shababi M, Villalón E, Kaifer KA, DeMarco V, Lorson CL. A Direct Comparison of IV and ICV Delivery Methods for Gene Replacement Therapy in a Mouse Model of SMARD1. Mol Ther Methods Clin Dev. 2018 Aug 17;10:348-360. doi: 10.1016/j.omtm.2018.08.005. PMID: 30202772; PMCID: PMC6127875.

Shababi, M., Feng, Z., Villalon, E., Sibigtroth, C. M., Osman, E. Y., Miller, M. R., Williams-Simon, P. A., Lombardi, A., Sass, T. H., Atkinson, A. K., Garcia, M. L., Ko, C.-P., & Lorson, C. L. (2016). Rescue of a Mouse Model of Spinal Muscular Atrophy with Respiratory Distress type 1 (SMARD1) by AAV9-IGHMBP2 is Dose Dependent. Molecular Therapy, 1(August 2015). https://doi.org/10.1038/mt.2016.33

Shababi, M., Smith, C. E., Kacher, M., Alrawi, Z., Villalón, E., Davis, D., Bryda, E. C., & Lorson, C. L. (2019). Development of a novel severe mouse model of spinal muscular atrophy with respiratory distress type 1: FVB-nmd. Biochemical and Biophysical Research Communications, 520(2), 341–346. https://doi.org/10.1016/j.bbrc.2019.10.032

Shao, S, von der Malsburg, K. & Hegde, R. S. Listerin-dependent nascent protein ubiquitination relies on ribosome subunit dissociation. Mol. Cell 50, 637–648 (2013).

Shao S, Brown A, Santhanam B, Hegde RS. Structure and assembly pathway of the ribosome quality control complex. Mol Cell. 2015 Feb 5;57(3):433-44. doi: 10.1016/j.molcel.2014.12.015. Epub 2015 Jan 8. PMID: 25578875; PMCID: PMC4321881.

Shawky, R. M., Elsayed, S. M., Zaki, M. E., Nour El-Din, S. M., & Kamal, F. M. (2013). Consanguinity and its relevance to clinical genetics. The Egyptian Journal of Medical Human Genetics, 14(2), 157-164. https://doi.org/10.1016/j.ejmhg.2013.01.002

Skre, H. (1974). Genetic and clinical aspects of Charcot-Marie-Tooth's disease. Clinical Genetics, 6(2), 98–118.

Smith CE, Lorson MA, Ricardez Hernandez SM, Al Rawi Z, Mao J, Marquez J, Villalón E, Keilholz AN, Smith CL, Garro-Kacher MO, Morcos T, Davis DJ, Bryda EC, Nichols NL, Lorson CL. The Ighmbp2D564N mouse model is the first SMARD1 model to demonstrate respiratory defects. Hum Mol Genet. 2022 Apr 22;31(8):1293-1307. doi: 10.1093/hmg/ddab317. PMID: 34726235; PMCID: PMC9029233.

Soung A, Klein RS. Viral Encephalitis and Neurologic Diseases: Focus on Astrocytes. Trends Mol Med. 2018 Nov;24(11):950-962. doi: 10.1016/j.molmed.2018.09.001. Epub 2018 Oct 9. PMID: 30314877; PMCID: PMC6546292.

Szklarczyk D, Gable AL, Lyon D, Junge A, Wyder S, Huerta-Cepas J, Simonovic M, Doncheva NT, Morris JH, Bork P, Jensen LJ, Mering CV. STRING v11: protein-protein association networks with increased coverage,

supporting functional discovery in genome-wide experimental datasets. Nucleic Acids Res. 2019 Jan 8;47(D1):D607-D613. doi: 10.1093/nar/gky1131. PMID: 30476243; PMCID: PMC6323986.

Tabebordbar M, Lagerborg KA, Stanton A, King EM, Ye S, Tellez L, Krunnfusz A, Tavakoli S, Widrick JJ, Messemer KA, Troiano EC, Moghadaszadeh B, Peacker BL, Leacock KA, Horwitz N, Beggs AH, Wagers AJ, Sabeti PC. Directed evolution of a family of AAV capsid variants enabling potent muscle-directed gene delivery across species. Cell. 2021 Sep 16;184(19):4919-4938.e22. doi: 10.1016/j.cell.2021.08.028. Epub 2021 Sep 9. PMID: 34506722; PMCID: PMC9344975.

Timmerman, V., Strickland, A. V., & Züchner, S. (2014). Genetics of Charcot-Marie-Tooth (CMT) disease within the frame of the human genome project success. Genes, 5(1), 13–32. https://doi.org/10.3390/genes5010013

Töpf A, Cox D, Zaharieva IT, Di Leo V, Sarparanta J, Jonson PH, Sealy IM, Smolnikov A, White RJ, Vihola A, Savarese M, Merteroglu M, Wali N, Laricchia KM, Venturini C, Vroling B, Stenton SL, Cummings BB, Harris E, Marini-Bettolo C, Diaz-Manera J, Henderson M, Barresi R, Duff J, England EM, Patrick J, Al-Husayni S, Biancalana V, Beggs AH, Bodi I, Bommireddipalli S, Bönnemann CG, Cairns A, Chiew MT, Claeys KG, Cooper ST, Davis MR, Donkervoort S, Erasmus CE, Fassad MR, Genetti CA, Grosmann C, Jungbluth H, Kamsteeg EJ, Lornage X, Löscher WN, Malfatti E, Manzur A, Martí P, Mongini TE, Muelas N, Nishikawa A, O'Donnell-Luria A, Ogonuki N, O'Grady GL, O'Heir E, Paquay S, Phadke R, Pletcher BA, Romero NB, Schouten M, Shah S, Smuts I, Sznajer Y, Tasca G, Taylor RW, Tuite A, Van den Bergh P, VanNoy G, Voermans NC, Wanschitz JV, Wraige E, Yoshimura K, Oates EC, Nakagawa O, Nishino I, Laporte J, Vilchez JJ, MacArthur DG, Sarkozy A, Cordell HJ, Udd B, Busch-Nentwich EM, Muntoni F, Straub V. Digenic inheritance involving a muscle-specific protein kinase and the giant titin protein causes a skeletal muscle myopathy. Nat Genet. 2024 Mar;56(3):395-407. doi: 10.1038/s41588-023-01651-0. Epub 2024 Mar 1. PMID: 38429495; PMCID: PMC10937387.

Tufts Medical Center. (2023). Approved Cell and Gene Therapy (CGT) products | Center for Biomedical System Design. TuftsMedicine. Retrieved May 15, 2024, from https://newdigs.tuftsmedicalcenter.org/payingforcures/defining-disruption/cell-and-gene-therapy-products-and-pipeline/approved-cell-and-gene-therapy-products/#:~:text=CBER%20uses%20both%20the%20Public,red%3B%20gene%20therapies%20as%20blue.

Vadla GP, Ricardez Hernandez SM, Mao J, Garro-Kacher MO, Lorson ZC, Rice RP, Hansen SA, Lorson CL, Singh K, Lorson MA. ABT1 modifies SMARD1 pathology via interactions with IGHMBP2 and stimulation of ATPase and helicase activity. JCI Insight. 2023 Jan 24;8(2):e164608. doi: 10.1172/jci.insight.164608. PMID: 36480289; PMCID: PMC9977310.

Vanoli F, Rinchetti P, Porro F, Parente V, Corti S. Clinical and molecular features and therapeutic perspectives of spinal muscular atrophy with respiratory distress type 1. J Cell Mol Med. 2015 Sep;19(9):2058-66. doi: 10.1111/jcmm.12606. Epub 2015 Jun 20. PMID: 26095024; PMCID: PMC4568910.

Viguier A, Lauwers-Cances V, Cintas P, Manel V, Peudenier S, Desguerre I, Quijano-Roy S, Vanhulle C, Fradin M, Isapof A, Jokic M, Mathieu-Dramard M, Dieterich K, Petit F, Magdelaine C, Giuliano F, Gras D, Haye D, Nizon M, Magen M, Bieth E, Cances C. Spinal muscular atrophy with respiratory distress type 1: A multicenter retrospective study. Neuromuscul Disord. 2019 Feb;29(2):114-126. doi: 10.1016/j.nmd.2018.10.002. Epub 2018 Oct 31. PMID: 30598237.

Villalón E, Shababi M, Kline R, Lorson ZC, Florea KM, Lorson CL, Selective vulnerability in neuronal populations in nmd/SMARD1 mice, Human Molecular Genetics, Volume 27, Issue 4, 15 February 2018, Pages 679–690, https://doi.org/10.1093/hmg/ddx434

Wagner JD, Huang L, Tetreault M, Majewski J, Boycott KM, Bulman DE; Care4Rare Canada Consortium; Dyment DA, McMillan HJ. Autosomal recessive axonal polyneuropathy in a sibling pair due to a novel homozygous mutation in IGHMBP2. Neuromuscul Disord. 2015 Oct;25(10):794-9. doi: 10.1016/j.nmd.2015.07.017. Epub 2015 Aug 5. PMID: 26298607.

Yong, K. J., Milenic, D. E., Baidoo, K. E., & Brechbiel, M. W. (2014). Impact of ??-targeted radiation therapy on gene expression in a pre-clinical model for disseminated peritoneal disease when combined with paclitaxel e108511. PLoS ONE, 9(9). https://doi.org/10.1371/journal.pone.0108511

Yuan, J., Hashiguchi, A., Yoshimura, A., Yaguchi, H., Tsuzaki, K., Ikeda, A., Wada-isoe, K., Ando, M., Nakamura, T., Higuchi, Y., Hiramatsu, Y., Okamoto, Y., & Takashima, H. (2017). Clinical diversity caused by novel IGHMBP2 variants. November 2016, 1–6. https://doi.org/10.1038/jhg.2017.15

Yubero D, Natera-de Benito D, Pijuan J, Armstrong J, Martorell L, Fernàndez G, Maynou J, Jou C, Roldan M, Ortez C, Nascimento A, Hoenicka J, Palau F. The Increasing Impact of Translational Research in the Molecular Diagnostics of Neuromuscular Diseases. Int J Mol Sci. 2021 Apr 20;22(8):4274. doi: 10.3390/ijms22084274. PMID: 33924139; PMCID: PMC8074304.

Zhu, J., Zhang, Y., Ghosh, A., Cuevas, R., Forero, A., Dhar, J., Ibsen, M., Schmid-Burgk, J., Schmidt, T., Ganapathiraju, M., Fujita, T., Hartmann, R., Barik, S., Hornung, V., Coyne, C., & Sarkar, S. (2014). Antiviral activity of human OASL protein is mediated by enhancing signaling of the RIG-I RNA sensor. Immunity (Cambridge, Mass.), 40(6), 936-948. https://doi.org/10.1016/j.immuni.2014.05.007

CRISPR-*Cas9* Mutagenesis. The C57BL/6J-Ighmbp2*em1Cx*/Cx (herein E365del, stock #28670, The Jackson Laboratory) and C57BL/6J-*Ighmbp2em5Cx*/Cx (herein Tyr918Cys, stock #33393, The Jackson Laboratory) strains were generated via CRISPR-*Cas9* mutagenesis performed by cytoplasmic microinjection of C57BL/6J zygotes with 100ng/μL *Cas9* mRNA and 50ng/μL of sgRNA (ACCACATCAAAGTAGTCCTCAGG) targeting exon 8 of *Ighmbp2* for E365del or 50ng/μL sgRNA (1: CTTCAGGCAGATGGTGGCTG; 2: CCCTCACTTCAGGCAGATGG) and 20ng/μL donor oligo (GCTGACAACACCTGTAGCTTCTCCAAGTGCTCGGCCAGCACCACCACTCTGGGCCA GTTCTGCATGCACTGTAGCCACCGCTGCTGCCTCAGCCACCATCTGCCCGAAGTGAG GGCCCCTTCTGGAC). Mosaic founder mice identified as carrying a mutation of interest in the targeted region were backcrossed to C57BL/6J. Resulting N1 progeny identified as carrying the mutation were further backcrossed to C57BL/6J to establish the colony and breed away from any potential off-target mutation. After a minimum of two backcrosses, mice were crossed in a sibling by sibling mating (N2F1) in order to assess animals carrying homozygous mutation of interest.

The C57BL/6J-Ighmbp2*em3Cx*/Cx (herein L362del, stock #28670, The Jackson Laboratory) and C57BL/6J-*Ighmbp2em4Cx*/Cx (herein 357Asp>Glu*fs*X383, stock #33393, The Jackson Laboratory) strains were generated via CRISPR-*Cas9* mutagenesis performed by cytoplasmic microinjection of C57BL/6J zygotes with 100ng/μL *Cas9* mRNA and 50ng/μL of sgRNA (CCTCAGGCAGCAGCTTCAGA) targeting exon 8 of *Ighmbp2* for L362del or 50ng/μL sgRNA (1: CTTCAGGCAGATGGTGGCTG; 2: CCCTCACTTCAGGCAGATGG) and 20ng/μL donor oligo (GCTGACAACACCTGTAGCTTCTCCAAGTGCTCGGCCAGCACCACCACTCTGGGCCA GTTCTGCATGCACTGTAGCCACCGCTGCTGCCTCAGCCACCATCTGCCCGAAGTGAG GGCCCCTTCTGGAC). The C57BL/6J-Ighmbp2*em6Cx*/Cx (herein C495del, stock #28670, The Jackson Laboratory). The Jackson Laboratory strains were generated via CRISPR-*Cas9* mutagenesis performed by cytoplasmic microinjection of C57BL/6J zygotes with 100ng/μL *Cas9* mRNA and 50ng/μL of sgRNA

(CTGCTGCTCATAGACACCGC) targeting exon 8 of *Ighmbp2* for C495del or 50ng/µL sgRNA (1:

CTGCTGCTCATAGACACCGC; 2: CTCATAGACACCGCTGGCTG) and 20ng/µL donor

oligo(AAGGACCAGGGAATCCTGGCTTGCAACTCACCCGGATTTCCCTTGGACTGGCTGTCCTCCTCCTCCAGCTCC

AGAAGCCCACAGCCAGCGATGTCTATGAGCAGCAGCGGGACACGTGTCTCCTCTG). Mosaic founder mice

identified as carrying a mutation of interest in the targeted region were backcrossed to C57BL/6J.

Resulting N1 progeny identified as carrying the mutation were further backcrossed to C57BL/6J to

establish the colony and breed away from any potential off-target mutation. After a minimum of two

backcrosses, mice were crossed in a sibling by sibling mating (N2F1) in order to assess animals carrying

homozygous mutation of interest.

Mouse Strains and Genotyping. All mouse husbandry and procedures were reviewed and approved by

the Institutional Animal Care and Use Committee at The Jackson Laboratory, and were carried out

according to the NIH Guide for Care and Use of Laboratory Animals. Mice were bred and maintained

under standard conditions. Tail or ear tissue was lysed in proteinase K at 55°C overnight and extracted

gDNA was used to determine genotype. Genotyping for C57BL/6J-*Ighmbp2*[em1Cx]/Cx (JAX stock #28670)

was performed via PCR using the following primers: forward primer specific to the wild type allele: 5'-

TGC TGC CTG AGG ACT ACT T -3'; forward primer specific to the mutant *em1* (L365del) allele: 5'-TGA

AGC TGC TGC CTG ACT-3' and reverse primer common for both alleles (i8r3) 5'-

AGGACTAACAGCCACACTGC-3'. Genotyping for C57BL/6J-*Ighmbp2*[em5Cx]/Cx (JAX stock #33393) was

performed via PCR forward primer: 5'- ACC ACT CTG GC CAG TTC T -3' and reverse primer 5'- CCC ACA

TC TCC AGA AGG -3' with a 5HEX-probe for the wildtype 5'CCA CCG CTA CTG CCT CAG -3' and a 6-FAM

probe for mutant allele 5'-CAC CGC TGC TGC CTC A -3'.

Genotyping for *Ighmbp2*[em3] and *Ighmbp*[em4] was performed via standard PCR and sanger sequencing

using the following primers: forward 5'- GCTCCTTTATCCAGTGAACC-3'; and reverse primer common for

both alleles 5'- AGGACTAACAGCCACACTGC-3'. Genotyping for *Ighmbp2^em6^* was performed via standard

PCR and sanger sequencing using the following primers: forward 5'-GTGAAGGAAGTCAGTCTTGC -3'; and

reverse primer common for both alleles 5'-AGAGGACCAATGCTCTTACC -3'.

In some experiments, motor axons were visualized by crossing the enhanced yellow fluorescence

protein (EYFP) motor-neuron-reporter line B6.cg(Thy1-YFP)16JrsJ {https://www.jax.org/strain/003709},

which were backcrossed to C57BL/6J, as described in Burgess et al 2006 to *Ighmbp2^em3^* and *Ighmbp2^em4^*

strains*.* Thy1-YFP mice were identified as reported previously (Feng et al., 2000).

Functional and Behavioral Assays.

von Frey Assessment. Mechanical allodynia was assessed by stimulating the plantar surface of the

mouse's hindpaw and measuring the latency to paw withdrawal. Mice are first habituated to the testing

room for a 60 minute period minimum and then allowed to habituate to the Plexiglas testing cubical for

30 minutes. The touch stimulator is moved to the paw for 1-2 seconds using the up-down method

(Chaplan et al., 1994). Between presentations of stimuli an interval of several seconds is used in order

to allow a response to the prior stimuli. Von Frey-type monofilaments with binding forces of 0.02,0.07,

0.16, 0.41, 1.0, 2.24, 5.5 g are applied successively to the plantar surface until a response is observed.

The threshold force required to elicit a withdrawal at least 50% of the time is determined. Males and

females were analyzed separately and compared and found no significant sex impact on von Frey assay.

Hot Plate Test. Hot plate test was utilized to evaluate thermal pain reflexes. Mice were habituated to

the testing room for a minimum of 30 minutes. A hot plate (Harvard apparatus LE7406) was maintained

at 52±2 ºC. Mice are placed into the cylinder and observed, with latency recorded to the first instance of

paw withdrawal, including jumping, hind paw lick, paw shack or flutter to the nearest 0.1 seconds by a

trained observer, who was blind to the subject's genotype. Maximum time allowed was 30s after which

the mouse was removed. Two trials were performed per mouse with an inter trial interval of 30

seconds. Males and females were analyzed separately and compared and found no significant sex impact.

Adhesive Tape Removal Test. To test both somatosensory and fine motor function an adhesive tape removal test was employed. Performance is assessed by measuring the time necessary to both sense and remove the adhesive. Briefly, the mice are acclimated to the procedure room for a minimum 60 minute period and then acclimated to the observation arena for 10 minutes prior to adhesive placement. Mice are gently restrained and adhesive label tape (Avery .25"-.75" diameter) is applied to the central forehead area. The latency to first contact with the tape, as well as the total time to remove is recorded. Maximum time allowed is 5 minutes. Males and females were analyzed separately and compared and found no significant sex impact.

Wire Hang Assay. Inverted wire hang assay was used to assess motor function starting at 2 weeks of age. Mice were placed on top of a wire mesh, which was then inverted allowing the mouse to hang suspended from it for a maximum of 60 seconds, and the latency to fall was measured. Mice were allowed to rest for a minimum of 5 minutes before repeating the test. The average of two tests was recorded per time-point. Where sex is not indicated, mice are presented as mixed sex, as prior analysis determined no significant sex impacts.

Rotarod Test. Rotarod was employed to test motor coordination of mice at 14 weeks of age. An Ugo Basile rotarod was utilized; briefly, the subject was placed on a fixed speed rod rotating at 4 rpm which increased linearly to a maximum of 40rpm over 300 seconds. Mice were given three successive trials, with about a one minute inter-trial interval. Males and females were analyzed separately and compared and found no significant sex impact.

Voluntary Homecage Wheel Running. Mice were individually housed with low profile running wheels with a wireless transmitter (Med Associates Inc, ENV-047). Running wheel rotations were measured in

1-hour bins to allow for distance traveled (sum of rotations) calculated per mouse each night. Average

rotations were calculated per mouse for each tracked night. Average speed while active was calculated

by isolating the dark hour intervals where activity was measured, and averaging the number of rotations

over the 12 hour dark period.

Nerve Conduction Analysis. Sciatic nerve conduction velocity (NCV) was assessed as previously

described (Bogdanik et al., 2013). Briefly, sciatic NCV was determined by measuring the latency of

compound motor action potentials recorded in the muscle of the right rear paw. Mice were

anesthetized with 1.5-2.0% isoflurane and placed on a thermostatically-regulated heat pad in order to

properly maintain normal body temperature. Action potentials were evoked via subcutaneous

stimulation at the sciatic notch and at the ankle. The reference electrode was placed in the skin

between the 4th and 5th digits, while the active recording needle electrode was inserted in the center of

the paw. To calculate velocity, the distance between the stimulation points was measured and divided

by the proximal minus distal latencies.

Grip Strength Test. To test for grip strength a commercially available grip-strength meter (Bioseb) was

used to measure forelimb and combined fore/hindlimb grasp strength as an indicator of neuromuscular

function. For measurements a wire grid was coupled to a strain gauge which measure peak force (kg)

the mouse was lowered gently towards the wire grid until it instinctively grasped the bar, with both

front paws only for forepaw measurements and all four paws for the combined. Animal was gently and

firmly pulled from the grid until it released, measuring the peak force in kg for a total of six consecutive

trials (3 forepaw only, 3 combined). An average over all 3 of each type of trial was calculated.

In vivo torque recording. Mice were anesthetized with isoflurane in O_2 (5% induction, 2-3%

maintenance) and the hair was trimmed off the lower limb. Mice were placed supine on a

homeothermic platform (32°C) with the left knee immobilized in a clamp employing a 25 gauge needle

pressed against the lateral, proximal tibia. The tibia was positioned horizontally, orthogonal to the left

hind paw that rested in a foot plate on a micromanipulator (300C-FP, Aurora Scientific, Ontario,

Canada). Tape (3M Transpore) was used to secure the dorsal surface of the paw to the foot plate. The

axis of the foot plate was attached to a torque sensor (605A, Aurora Scientific) and measures the torque

of the dorsiflexion of the foot when the tibialis anterior muscle contracts. Data was recorded with the

DMC software (Aurora Scientific) and analyzed with the DMA software (Aurora Scientific). Muscle

contractions were elicited by electrical stimulation (701C, Aurora Scientific) with a pair of stainless steel

electrodes. Duration of anesthesia was less than 15 min. Torque responses were recorded at increasing

frequencies at 10 s intervals: a single pulse (T0 or twitch), 10, 30, 50, 80, 120 and 150 Hz, with each

stimulation applied for 300 ms. The maximum torque obtained for each stimulation frequency was used

to produce the force-frequency curves.

Echocardiography. Mice were anesthetized with 5% isoflurane mixed with 100% oxygen at 1.0 l/min

flow and then maintained under anesthesia with 1.5% isoflurane/oxygen flow. Ophthalmic ointment was

placed on the eyes to prevent drying of the cornea while the mouse was anesthetized and tested. Mice

were placed on a thermostatically controlled heated platform, where isoflurane anesthesia was

maintained by delivery through a close fitting face-mask. A heating lamp was also used to keep the heart

rate and body temperature constant at physiological status during echocardiography. During the

examination, the animal's heart rate was monitored through the use of an electrocardiograph. The

mouse's heart rate and body temperature were monitored continuously during the scanning. Fur was

removed from the ventral surface of the mouse torso with clippers and Nair (Church & Dwight, Ewing,

NJ).

Respiratory Analysis through the PiezoSleep System. The PiezoSleep System, designed to monitor and

analyze sleep/wake cycles in rodents over extended periods of time,[3] was used as a non-invasive

method for measuring respiration in mouse pups aged from ages p1 to p14. The system consists of a

Piezoelectric polymer film that transforms mechanical pressure into electric signals,[3] which can then be

analyzed through a graph that shows the magnitude of the signal. Pups were swaddled with a piece of

gauze and medical tape (ages p1 to p7) or 'scruffed' and swaddled (p8 to p14) onto the pad in a way

that ensured the mouse's torso was making contact with the sensor. The 'scruffing' technique implies

gently grabbing the mice by the extra skin on their backs which helps calm them. This technique seems

to prevent them from running when placed on the sensor and causes them to relax. They were

monitored for excessive movement that would affect data collection and readjusted as necessary. A

heat lamp was placed on top of the cage and a thermometer inside of it to ensure temperature ranged

between 75° and 95° F, the range found to most decrease unwanted movement in the pups.

Five to ten minutes of quality data were collected for each pup, and data was analyzed in intervals of 3

and 10 seconds. The 3 second intervals were used to measure breath frequency, and the 10 second

intervals were used for qualitative analysis of certain breath patterns. Amplitude was not used as a

measurement due to external factors that can affect it, such as weight and position. Measuring

respiration in mouse pups is currently a challenge to many researchers due to a lack of methods and

equipment,[2] so this innovative method could be used for studying other early onset respiratory illnesses

in mice.

Histology.

Analysis of Nerves. Motor and sensory branches of the femoral nerve and phrenic nerve were dissected

and fixed overnight. For myelinated axon count and diameter analyses, images were captured using a

Nikon Eclipse E600 microscope with a 40x objective. The total number of myelinated axons in each

nerve was counted using an automated method in ImageJ with manual confirmation as previously

described. Briefly, with ImageJ software, the Threshold function was adjusted in order to only highlight

axoplasm on whole nerve sections, and Analyze particle function was then used to quantify the number

of myelinated axons and areas of each nerve. The diameter was determined from axonal area. Images of

large nerves that could not be captured as a single image at 40x magnification were generated as

montages to show the whole nerve, using the ImageJ Stitching Grid/Pairwise plugin.

G-Ratios. Femoral motor axons of 19 week old wildtype, heterozygous, and homozygous Y918C animals

were evaluated at 80 kV using a JEOL JM-1230 transmission electron microscope (JEOL, Tokyo, Japan)

and images collected with an AMT 2K digital camera (Advanced Microscopy Techniques, Woburn, MA.)

with a 4,000x objective. Myelin thickness and axon diameter of 100 axons per nerve were collected and

g-ratios were calculated by dividing the myelin thickness by the inner axon diameter by the outer axon

diameter for each respective axon.

Neuromuscular Junction Visualization and Quantification. Tissue (medial gastrocnemius & soleus) was

dissected and fixed for 2h in cold 2% paraformaldehyde/PBS. The samples were then incubated in

blocking solution (2.5% BSA (Sigma-Aldrich) and 1%Triton-X 100(Sigma-Aldrich) in PBS) for 1h before

they were gently teased apart and pressed between two glass slides using a binder clip for 15 minutes at

4°C. Nerves were visualized with the transgenic-EYFP. Acetylcholine receptors (AchRs) were visualized by

staining with 1:1000 α-bungarotoxin conjugated with Alexa-Fluor 594 (Invitrogen, Carlsbad, CA),

incubated at room temperature on a rocker in blocking solution for 2 hours. Post-incubation samples

were rinsed three times and washed at least four times for 15 minutes each. Samples were mounted in

gelvatrol (http://cshprotocols.cshlp.org/content/2006/1/pdb.rec10252.short). Occupancy of 50 or

greater randomly selected neuromuscular junctions (NMJs) were scored blinded to genotype on a Nikon

E600 fluorescence microscope. Full occupancy of NMJ was defined as when presynaptic nerve staining

fully overlaid with AChR, partial occupancy as when positive for AChR but only partially stained for

presynaptic nerve, and denervation as when positive for AChR but negative for presynaptic nerve

staining. Images were obtained on a Leica SP8 laser-scanning confocal microscope with a 63x objective

lens. Z stacks were collapsed into projected images and merged using ImageJ (NIH,

http://rsb.info.nih.goc/ij/).

H&E staining. Mice were euthanized and right hindlimb was extracted and post-fixed in Bouin's fixative.

For Gastrocnemius and Soleus muscles, mice were euthanized and right hindlimb was extracted and

post-fixed in Bouin's fixative for a minimum of two weeks. Whole hindlimbs were cross-sectioned

through middle portion of lower and upper legs. Similarly, the whole chest cavity of the mouse was

extracted, being sure to keep ribcage and diaphragm intact, and post-fixed in Bouin's fixative. Whole

chest cavity was coronally sectioned. The sectioned tissues were then paraffin-embedded, sectioned,

mounted and stained with hematoxylin and eosin for light microscopic analysis according to standard

histological procedures. Slides were scanned using a NanoZoomer 2.0 (Hamamatsu) at 40x

magnification. Whole lower hindlimb representative images were taken from 2.5x digital magnification

using NDP.view2 software (Hamamatsu) and stitched together using ImageJ Stitching Grid/Pairwise

plugin (Preibisch et al., 2009). Representative images were taken from 40x magnification from the

medial gastrocnemius (MG) and soleus (Sol) regions of the lower leg, using NDP.view2 software

(Hamamatsu). Similarly, the whole chest cavity representative images were taken from 1.5X

magnification and 40x for highlighted regions of intercostal and diaphragm. Analysis muscle fiber of the

MG, Sol, and intercostal muscles were performed by assessing muscle fiber area. Two images per muscle

per animal were captured using a Nikon Eclipse E600 microscope with 40x objective lens. Cross-

sectioned muscle fibers were manually traced using ImageJ from each image and combined per animal.

To assess diaphragm thickness ten linear measurements were taken every ~200µm from where the

diaphragm attaches to the intercostal region in NDP.view2 software (Hamamatsu). Thickness

measurements were presented as an average per animal.

Trichrome staining. Mice were euthanized with CO_2 and perfused with HBSS buffer (ThermoFisher). The heart was carefully removed and placed in 60mM KCl while still beating to synchronize the contractile phase for 5 min before fixing in 4% PFA overnight at 4°C. They were then embedded in paraffin and sectioned coronally around the mid-line of the heart and stained with trichrome. Representative images were taken from the upper portion of the left ventricle on Nikon Eclipse E600 microscope at 60x magnification.

TaqMan™ Gene Expression Analysis. Whole spinal cords were collected at 2 weeks of age and snap frozen on liquid. Frozen tissue was homogenized using a PowerGen 125 homogenizer (Fisher Scientific) in TRIzol™ reagent (Invitrogen #15596026). After the addition of chloroform and phase separation, the aqueous phase was transferred to a miRNEasy Kit column (Quiagen cat#217004) and processed according to the kit protocol with the addition of a DNase treatment (Qiagen cat#79254) on the column. RNA quantity was measured using a NanoDrop (ThermoFisher Scientific), and 1µg of total RNA was used to synthesize cDNA with a SuperScript® III First-Strand Synthesis Kit (Invitrogen #18080-0051) and random hexamers. Ighbmp2 was measured using a TaqMan™ gene expression assay (Applied Biosystems Mm00456315_m1 assay) and normalized against GAPDH expression (Applied Biosystems Mm99999915_g1 assay) in the same reaction. Data was graphed using Prism 7 software (GraphPad) and a 2-Way Anova with Tukey's multiple comparison test was used to determine significant differences.

Protein Expression Analyses. Mice were cervical dislocated and spinal cord and brain were immediately collected, snap-frozen in liquid nitrogen and stored at -80°C. Tissues were homogenized in lysis buffer (20 mM Tris-HCl (pH7.5), 150 mM NaCl, 5 mM EDTA (pH8), protease inhibitor (cOmplete Protease Inhibitor Cocktail, Roche)) using FastPrep™ Lysing MatrixD (MP Biomedicals,) with a FastPrep™ homogenizer set at speed 4 for 20s. Rest on ice for 10 minutes and draw off supernatant. Supernatant was sonicated, then pre-cleared at 16,0000 xg for 1hour at 4C. Protein concentrations were determined by BCA method using a Pierce BCA kit (Pierce). Protein samples were boiled into sample buffer and were

run on 4-15% Mini-PROTEAN TGX precast gels (BioRAD), transferred onto a PVDF membrane (type) and immunoblotted with 1:1000 anti-Ighmbp2 (clone11-24, Milipore-Sigma) incubated over 3 nights in CH block(from where) and 1:10000 anti-mouse (Perkin-Elmer). Blots were developed using ECL reagent a combination of 50% west supersignal pico and 50% west supersignal femto (Thermo Fisher) and images in an Azure Biosystem C600 Imager or on X-Ray film.

microCT at E18.5. Whole embryonic day 18.5 pups were isolated from timed-pregnant females and immediately immersed in 1xPBS buffer to euthanize according to the Jackson Laboratory IACUC protocol 99066. They were then immersion fixed in 4% paraformaldehyde in 1xPBS for 3 days before being placed in a tube with stabilization buffer (4% w/vol PFA, 4% w/vol acrylamide (BIO-RAD, Cat# 161-0140), 0.05% w/vol bis-arcylamide (BIO-RAD, Cat# 161-0142), 0.25% VA044 initiator (Wako Chemical, Cat# 017-19362), 0.05% w/vol Saponin (Sigma, Cat# 84510) in 1x PBS) for another 3 days. At this point, the samples were put in a desiccator and purged with nitrogen gas for 5 min before being placed in a 37°C incubator for 3 hours to allow the hydrogel to polymerize. Right before imaging, they were immersion stained with Lugol Solution (Sigma, Cat# L6146-1L) for 2 days at 4°C before being embedded in 1% agarose with 1xPBS on the day of imaging. Samples were imaged on a Skyscan 1172 microCT (Brunker) and images were reconstructed via NRecon Reconstruction software (Micro Photonics Inc). Imaging and analysis was done using 3DSlicer version 4.10.0 software.

p1 Intracerebroventricular injections: p1 pups were chilled on ice for ~ 15 minutes or until pups no longer responded to touch. The pup was then placed on a chilled clay ramp. With thumb and pointer finger behind the pup's head to keep it steady, 4uL of virus were injected into the lateral ventricle of the pup via glass Hamilton gas-tight 10uL syringe. Once the 4uLs of virus were injected, the needle was kept in place for ~8 seconds and restraint on the pup was released to ensure no leakage of virus. The pups were then put under a heat lamp and given light hand stimulation to allow faster recovery from

anesthesia and injection. Pups were then placed in 80-95F heated cage with wood chip bedding. Once all

pups recovered, they were toe clipped to keep track of each individual pup and to genotype. Once pups

were warmed and bleeding of the snipped toe clotted, they were returned to the original breeding pair.

Statistical Analyses. Statistical tests were performed using GraphPad's Prism 7 software. A threshold of

$p<0.05$ was considered significant. Significance was determined using a one or two-way ANOVA and a

post-hoc Tukey test for individual difference when appropriate. For data with males and females

combined, it was determined that there was no sex dependent difference with a one-way ANOVA. The

use of other tests are noted in the legends. Results are presented as means ± SD.

Supp. Table 1

Table 1. Perinatal lethality of homozygous IGHMBP2 null mice.

Litters	+/+	Heterozygous	Mutant	Total
1-7 (checked at 3 week wean)	15 (29.4%)	36 (70.6%)	0 (0%)	51
8-15 (checked at P0)	17 (29.3%)	30 (51.7%)	11(19%)	58

Supplemental Figure 1. C495del mutants at p7 bodyweight matched with +/+ at p1.
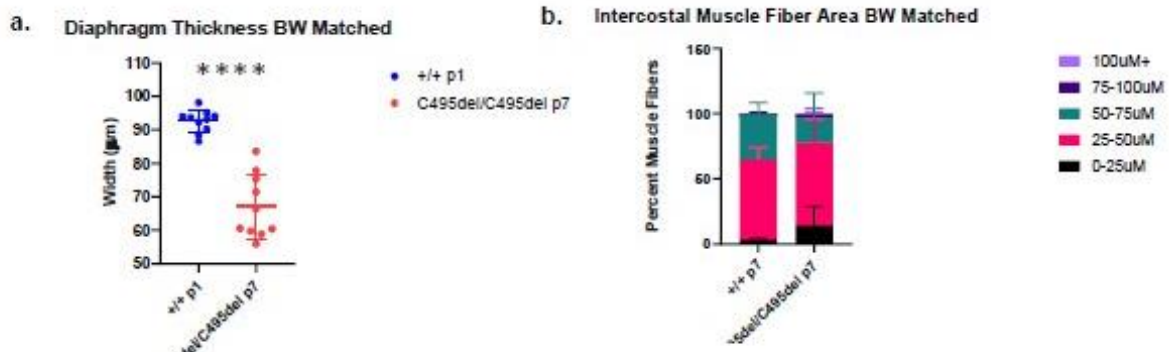
Supplemental Figure 1. C495del mutants at p7 bodyweight matched with +/+ at p1. (a) C495del/C495del mutants have significantly thinner diaphragms (p<0.0001) (N = 10 and 10 respectively). (b) There is no significant difference in intercostal fiber size between bodyweight matched C495del/C495del and +/+ pups.

Supplemental Figure 2. Schematic of three assessed cohorts for CMT assessment pipeline.
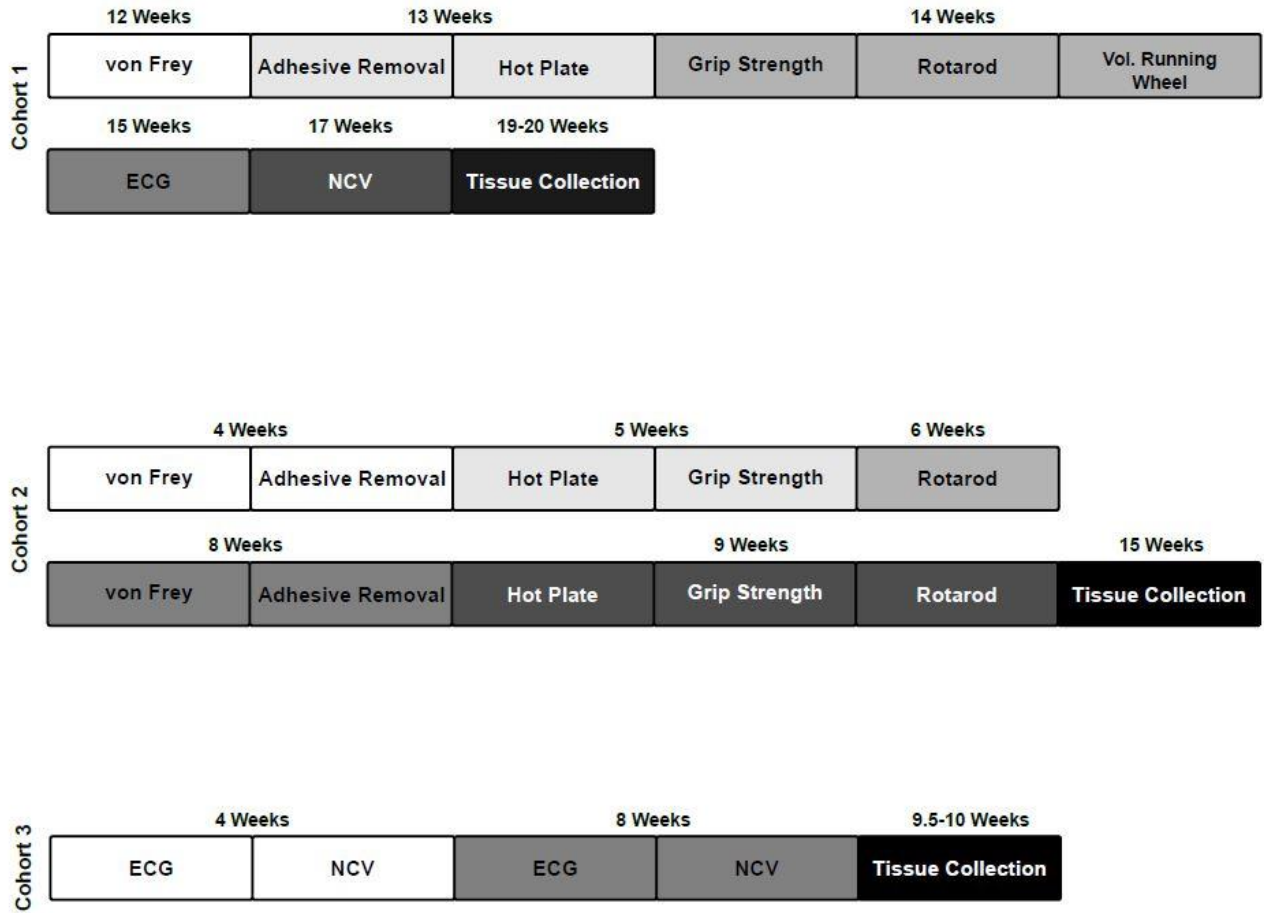
Supplemental Figure 2. Schematic of three assessed cohorts for CMT assessment pipeline. An outline of the cohorts and when measurements, assays, and tissues were collected over course of E365del experiments.

Supplemental Figure 3. Heterozygous E365del mice do not show neuromuscular deficits at 12-20 weeks of age.
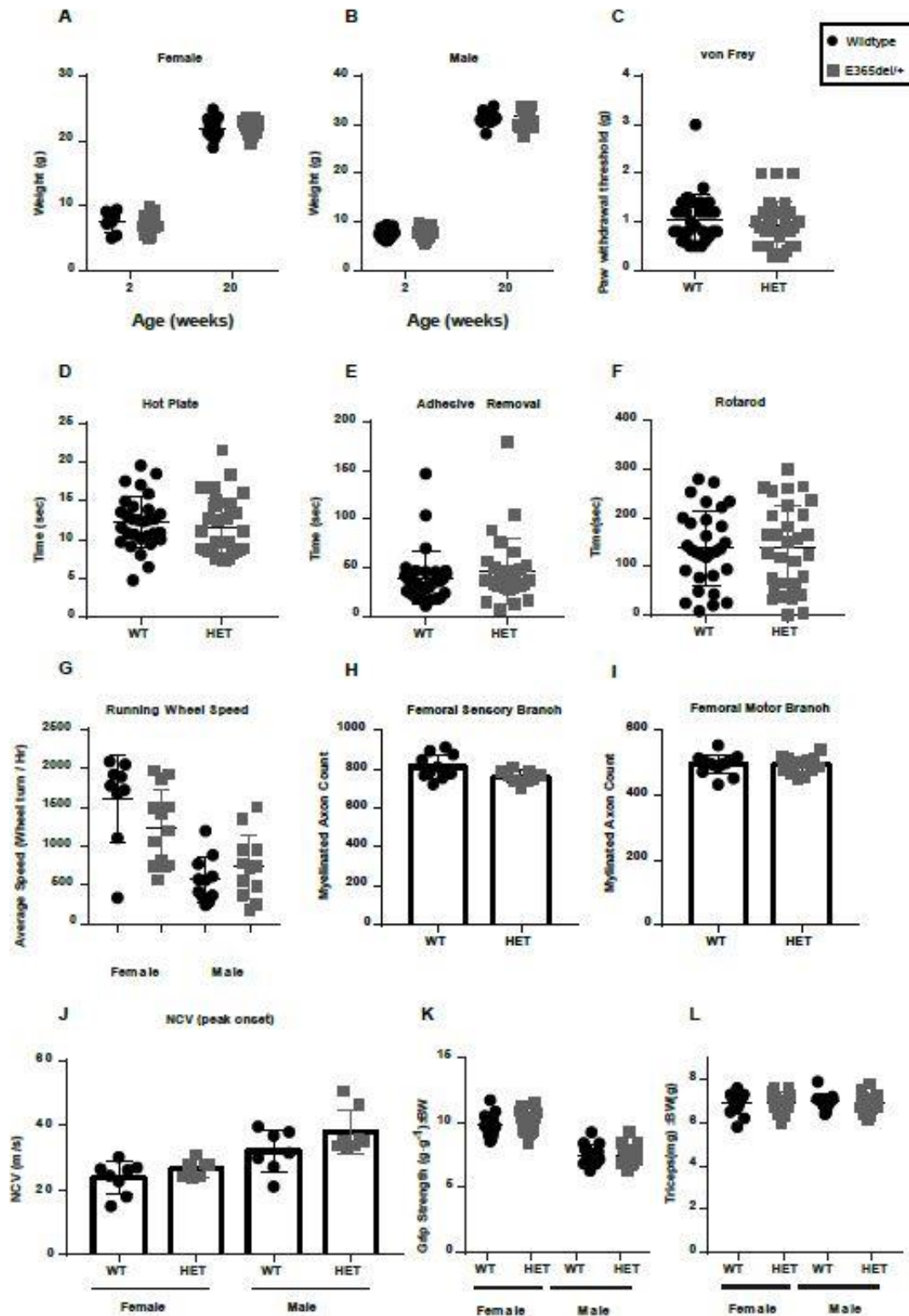
Supplemental Figure 3. Heterozygous E365del mice do not show neuromuscular deficits at 12-20 weeks of age. (a) Female wildtype and heterozygous mice were comparable body weights at 2 weeks of age (wildtype: n=8, 7.46±1.58g; heterozygous n=18, 7.37±1.30g) and 20 weeks of age (wildtype: n=15, 21.96±1.48g; heterozygous: n=15, 22.1±1.09g). **(b)** Male wildtype and heterozygous mice were comparable boy weights at 2 weeks of age (wildtype; n=13, 7.56±1.09g; heterozygous n=16, 7.56±1.14g) and 20 weeks of age (wildtype: n=31.59±1.28g, n=15; heterozygous: n=15, 31.64±1.99g). **(c)** von Frey assessment indicated that wildtype mice (1.0±0.5g, n=30) at 12 weeks of age had comparable paw withdrawal threshold as heterozygous littermates (0.9±0.48g, n=30). **(d)** Response time to thermal pain with the hot plate assay at 13 weeks of age was not significantly different between wildtype (12.29±3.3s, n=30) and heterozygous littermates (11.63±3.8s, n=30). **(e)** The cumulative time to remove an adhesive sticker from the forehead at 13 weeks of age was not significantly different between wildtype (39.8±27s, n=30) and heterozygous (46.27±33.1s, n=30) littermates. **(f)** Wildtype (137.9±77.7s, n=30) and heterozygous (138.7±87.9s, n=30) mice exhibited similar motor performance on the rotarod at 13 weeks of age. **(g)** As a test of motor performance and endurance voluntary running wheels were assessed for average speed over the 12 hour dark period. Speed was not significantly different for both female wildtype (1621±561.8 turns/hour, n=9) and heterozygous (1238±498.2 turns/hour, n=13) and male wildtype (571±289.3 turns/hour, n=11) and heterozygous (739±408.5 turns/hour, n=12). **(h)** Cross-sections of the femoral sensory branch were quantified for myelinated axons at 20 weeks of age and found no difference between wildtype (813±62.2 axons, n=11) and heterozygous (762.9±32.1, n=9). **(i)** No difference was observed at 20 weeks of age in the femoral motor branch myelinated axons of wildtype (496.1±28.3, n=15) and heterozygous (494±24.4, n=15). **(j)** Nerve conduction velocity was not different at 18 weeks of age in either female (wildtype: 23.7±5.0, n=8; heterozygous:26.6±2.6, n=7) or male (wildtype:32.0±6.6, n=7; heterozygous:37.9±6.7, n=8). **(k)** Muscle strength was comparable for wildtype and heterozygous mice for both female (wildtype: 9.8±0.83, n-15; heterozygous 9,9±0.9, n=15) and male (wildtype: 7.5±0.8, n=15; heterozygous: 7.5±0.8, n=15). **(l)** To assess muscle mass a ratio of triceps to body weight was taken for female (wildtype: 6.9± 0.5, n=15; heterozygous: 6.94±047, n=15) and male (wildtype:6.9±0.46, n=15; heterozygous: 6.94±0.47, n=15).

**Supplemental Figure 4. Neuromuscular junctions are denervated by 8 weeks of age.**
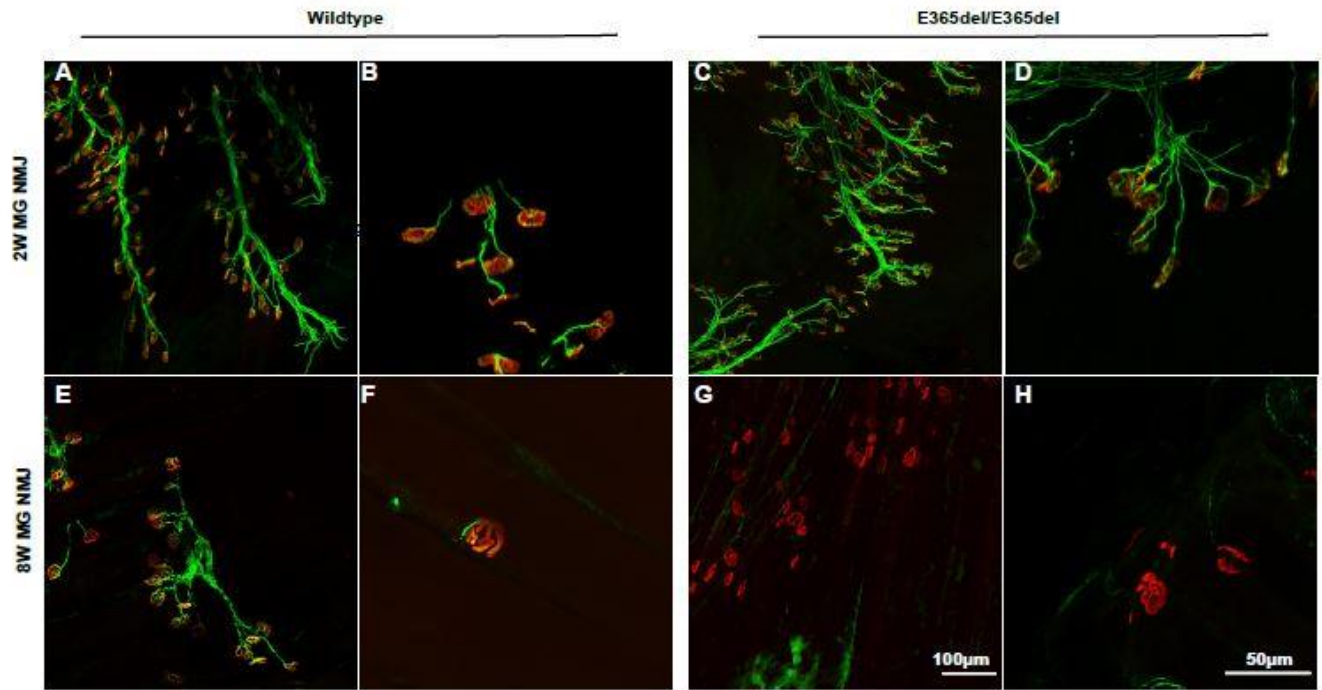
Supplemental Figure 4. Neuromuscular junctions are denervated by 8 weeks of age. (a,b) NMJs from the MG muscle of 2 week old wildtype and c,d, homozygous E365del mice are innervated and fully occupied. However, by 8 weeks of age wildtype Ee,f, show full innervation, while homozygous mutants G,H, show many denervated junctions.

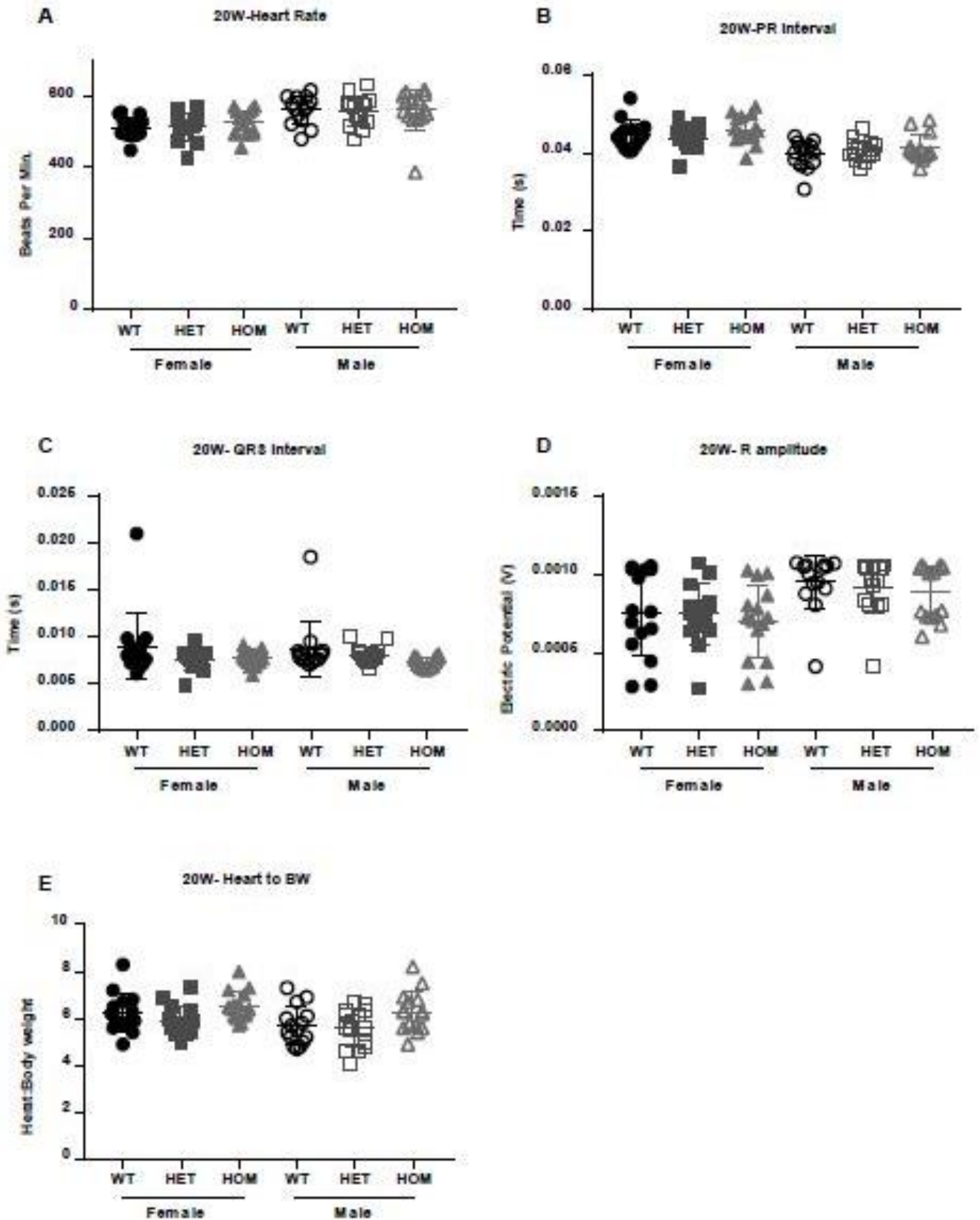**Supplemental Figure 5. Homozygous mice display muscular weakness and atrophy.**
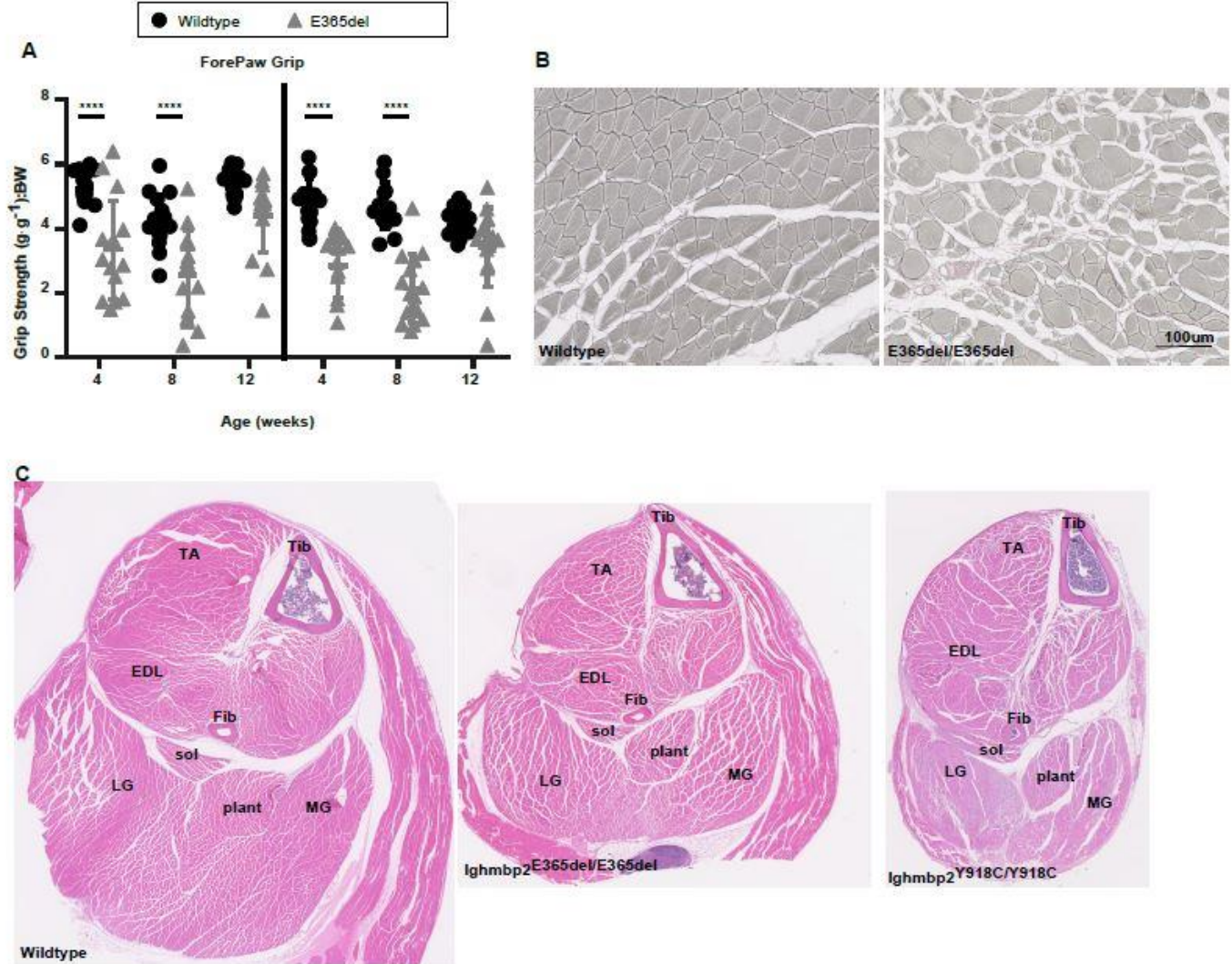
Supplemental Figure 5. Homozygous mice display muscular weakness and atrophy. (a) Forepaw grip strength assessment indicated that homozygous mice were weaker than wildtype at 4 and 8 weeks of age ($p < 0.0001$) for both male and female, but were not significantly different at 12 weeks of age (female: $p = 0.0517$, male: $p = 0.1854$). **(b)** Reticulin stain of wildtype and homozygous medial gastrocnemius **(c)** Whole cross-section of the lower hindlimb stained with H&E with wildtype (8 weeks), E365del (8 weeks), and Y918C (16 weeks) with E365del and Y918C showing atrophic fibers. Y918C is overtly the smallest of the cross-sections. Abbreviations are as follows: MG (medial gastroneumius), plant (plantaris), sol (soleus), LG (lateral gastrocnemius), Fib (fibula), EDL (extensor digitorum longii), TA (tibialis anterior), Tib (tibia).

Supplemental Figure 6. E365del mice had progressive muscular weakness.
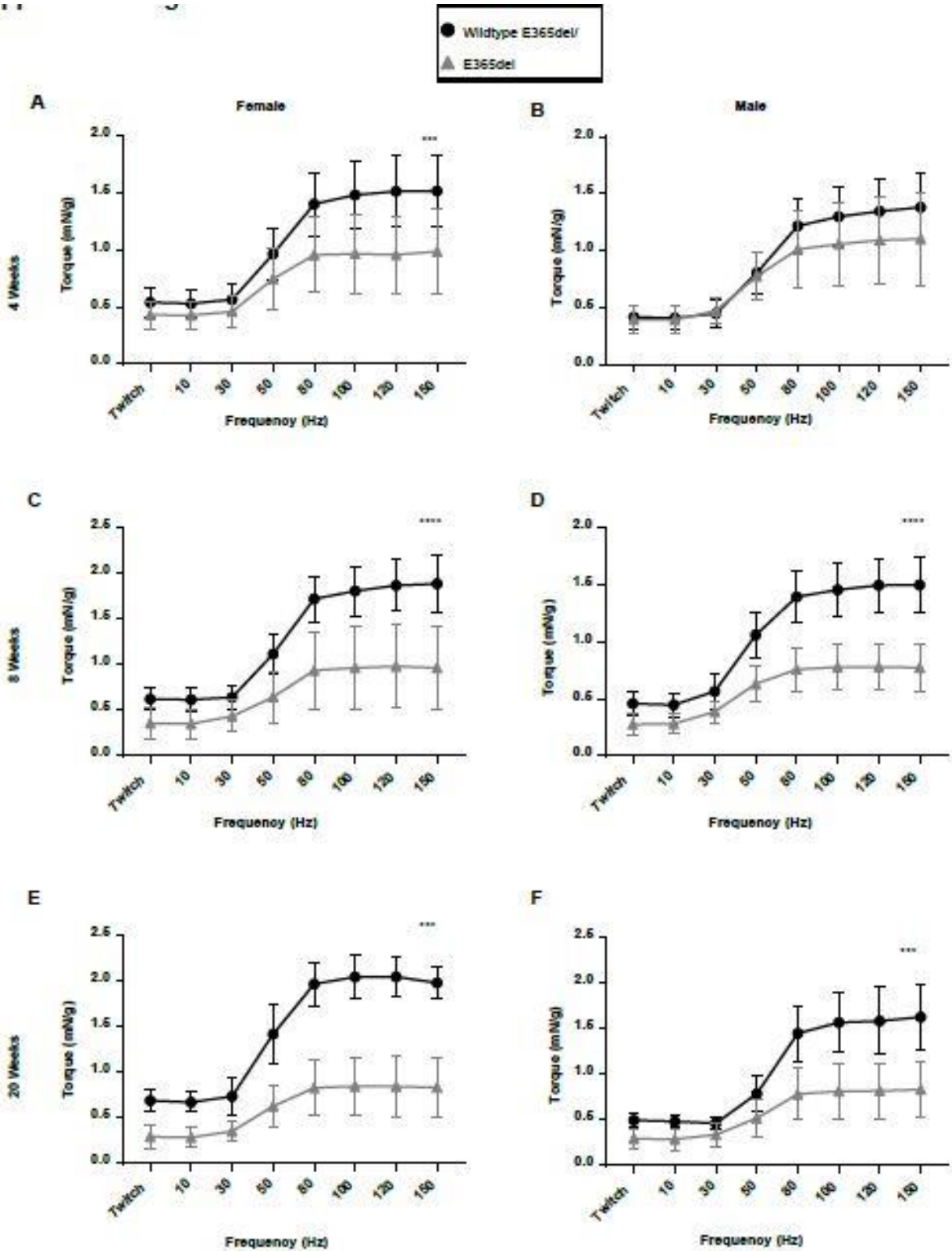
Supplemental Figure 6. E365del mice had progressive muscular weakness. (a) Female homozygous mice (n=15) show muscular weakness as evident by decreased force response normalized to body weight compared to wildtype littermates (n=15) (p=0.0007) **(b)** Male wildtype (n=12) and homozygous mice (n=13) do not show a difference in isometric force normalized to bodyweight at 4 weeks of age (p=0.1678) **(c)** Female homozygous mice (n=15) continue to show significant muscular weakness compared to wildtype littermates (n=15) at 8 weeks of age (p<0.0001) **(d)** Male homozygous mice (n=13) also continue to show significant muscular weakness compared to wildtype littermates (n=12) at 8 weeks of age (p<0.0001) **(e)** Female homozygous (n=8) mice show a muscular weakness compared to wildtype littermates (n=8) at 20 weeks of age (p<0.001) **(f)** Male homozygous (n=8) mice show a muscular weakness compared to wildtype littermates (n=8) at 20 weeks of age (p<0.001)

Supplemental Figure 7. E365del homozygous mice do not exhibit any cardiac phenotype

Supplemental Figure 7. E365del homozygous mice do not exhibit any cardiac phenotype. (a) Heart rate was not different between wildtype (Female: 511.6±29.14, n=15; Male:562.3±39.85, n=14), heterozygous (Female:512.8±37.01, n=14; Male:559.2±42.12, n=15), or homozygous (Female: 526.1±35.17, n=15; Male: 562.9±56.8, n=15). **(b)** The PR interval was not different at 20 weeks of age between wildtype (Female:0.044±0.00355, n=15; Male:0.03965±0.0035, n=14), heterozygous (Female: 0.0437±0.003, n=14; Male: 0.0406±0.0025, n=15), homozygous (Female: 0.0459±0.0035, n=15; Male: 0.041±0.0035, n=14). **(c)** The QRS interval was not different at 20 weeks of age between wildtype (Female: 0.0089±0.0035, n=15; Male: 0.0087±0.0028, n=14), heterozygous (Female: 0.0075±0.0011, n=14; Male: 0.0079±0.00096, n=15), homozygous (Female: 0.0077±0.00085, n=15; Male: 0.0072±0.00096, n=14). **(d)** R amplitude was not different at 20 weeks of age wildtype (Female: 0.00074±0.0002, n=15; Male:0.00095±0.0001, n=14), heterozygous (Female: 0.000797±0.0002, n=14; Male: 0.00092±0.00017, n=15) and homozygous (Female: 0.00069±0.0002, n=15; Male: 0.0008±0.0001, n=15) **(e)** Cardiac muscle was not different as indicated by heart to body weight ratio wildtype (Female: 6.2±0.82, n=15; Male: 5.6±0.80, n=15), heterozygous (Female: 5.9±0.62, n=15; Male 5.59±0.81, n=15) and homozygous (Female 6.5±0.624, n=15; Male 6.28±0.85, n=15).

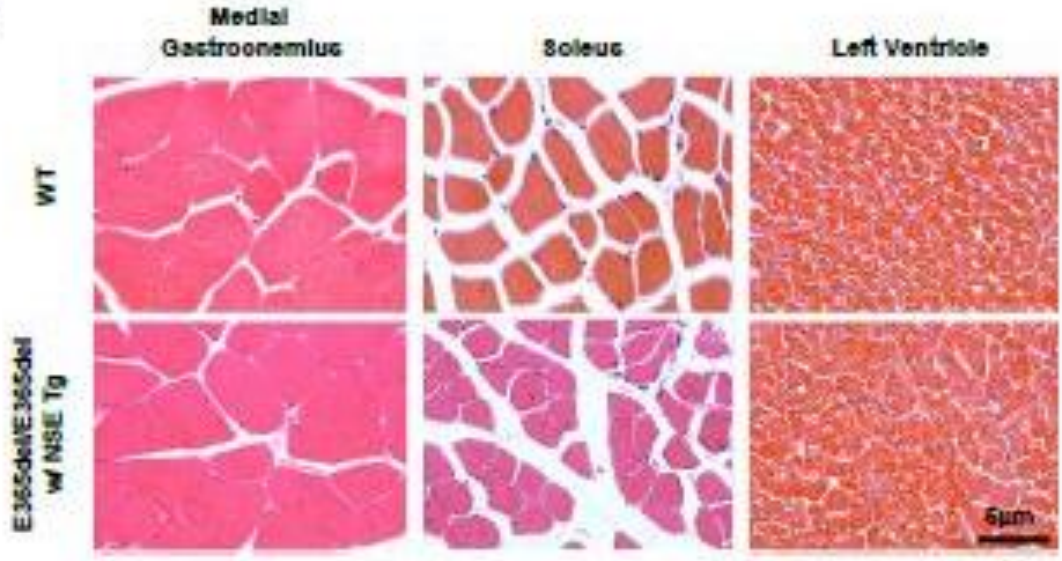**Supplemental Figure 8. E365del homozygous mice are rescued with neuronal expression of *Ighmbp2***

E
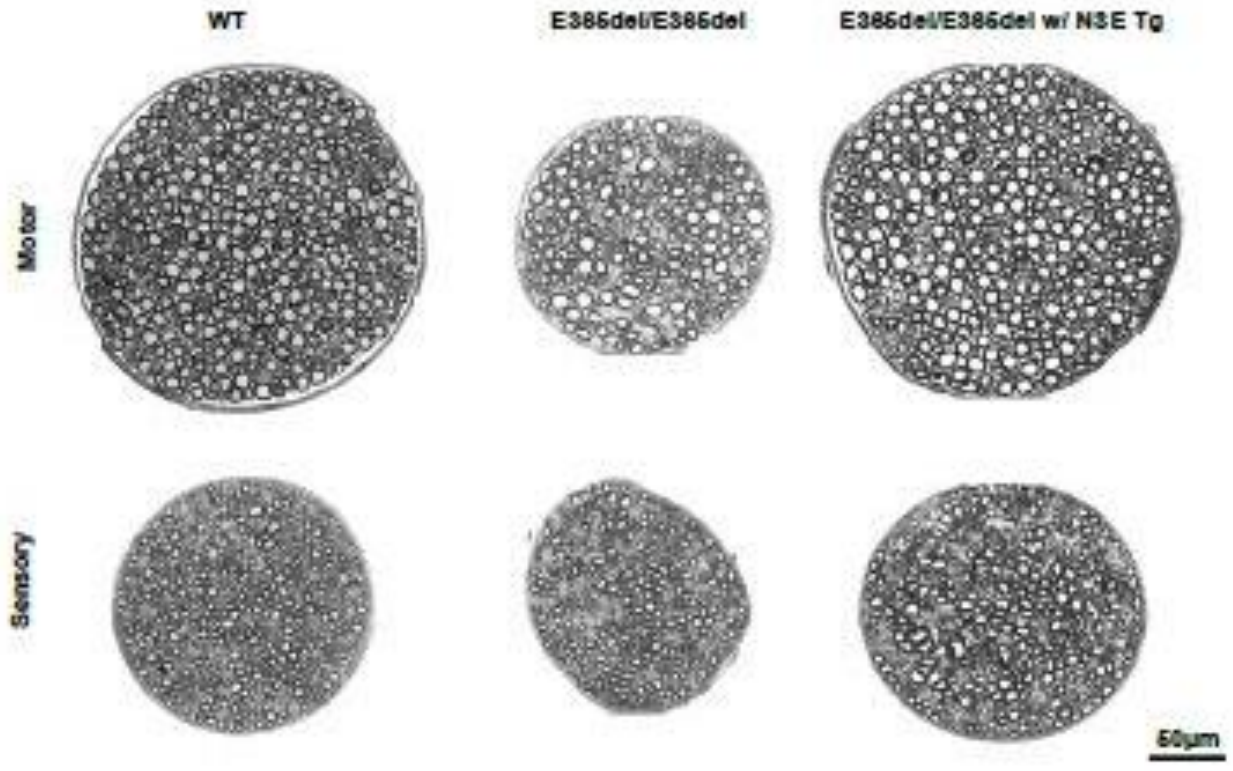
	WT	E385del/E385del	E385del/E385del w/ NSE Tg
Motor			
Sensory			

50µm

F

	Medial Gastrocnemius	Soleus	Left Ventricle
WT			
E385del/E385del w/ NSE Tg			

5µm

Supplemental Figure 8. E365del homozygous mice are rescued with neuronal expression of _Ighmbp2._(a) 8-month-old homozygous E365del mice are thin and wasted, while the e365del homozygous mice carrying the _Ighmbp2_-NSE transgene are indistinguishable from wildtype littermates. **(b)** The lifespan of the _Ighmbp2_-NSE rescued E365del homozygous mice is not significantly different from the E365del homozygous mice (p=0.1265; Log-Rank, Mantel-Cox test) **(c)** Growth curves of female control, E365del homozygous with the NSE transgene and E365del homozygous shows no significant difference between NSE rescued and controls (Two-way ANOVA, p=0.0986), while E365del homozygous with NSE have an increased growth curve compared to the E365del homozygous (p<0.0001; Two-way ANOVA). **(d)** Male E365del homozygous with NSE rescued had shifted growth curves to male control mice (Two-way ANOVA, p<0.0001), apparent by 32 weeks of age (Sidak's multiple comparisons test, p=0.0008). while they had an improved curve when compared to E365del homozygous mice (Two-way ANOVA, p<0.0001), apparent by 7 weeks of age (Sidak's multiple comparisons test, p=0.0073).

(e) Femoral motor and sensory nerves showed overall size and counts to be comparable to wildtype myelinated axons at 8 months of age (Scale bar = 50μm). **(f)** 8-Month-old Hematoxylin & Eosin stained skeletal (medial gastrocnemius and soleus) and Trichrome stained cardiac muscles of E365del homozygous with NSE transgene taken at 40x magnification (Scale bar=5μm).
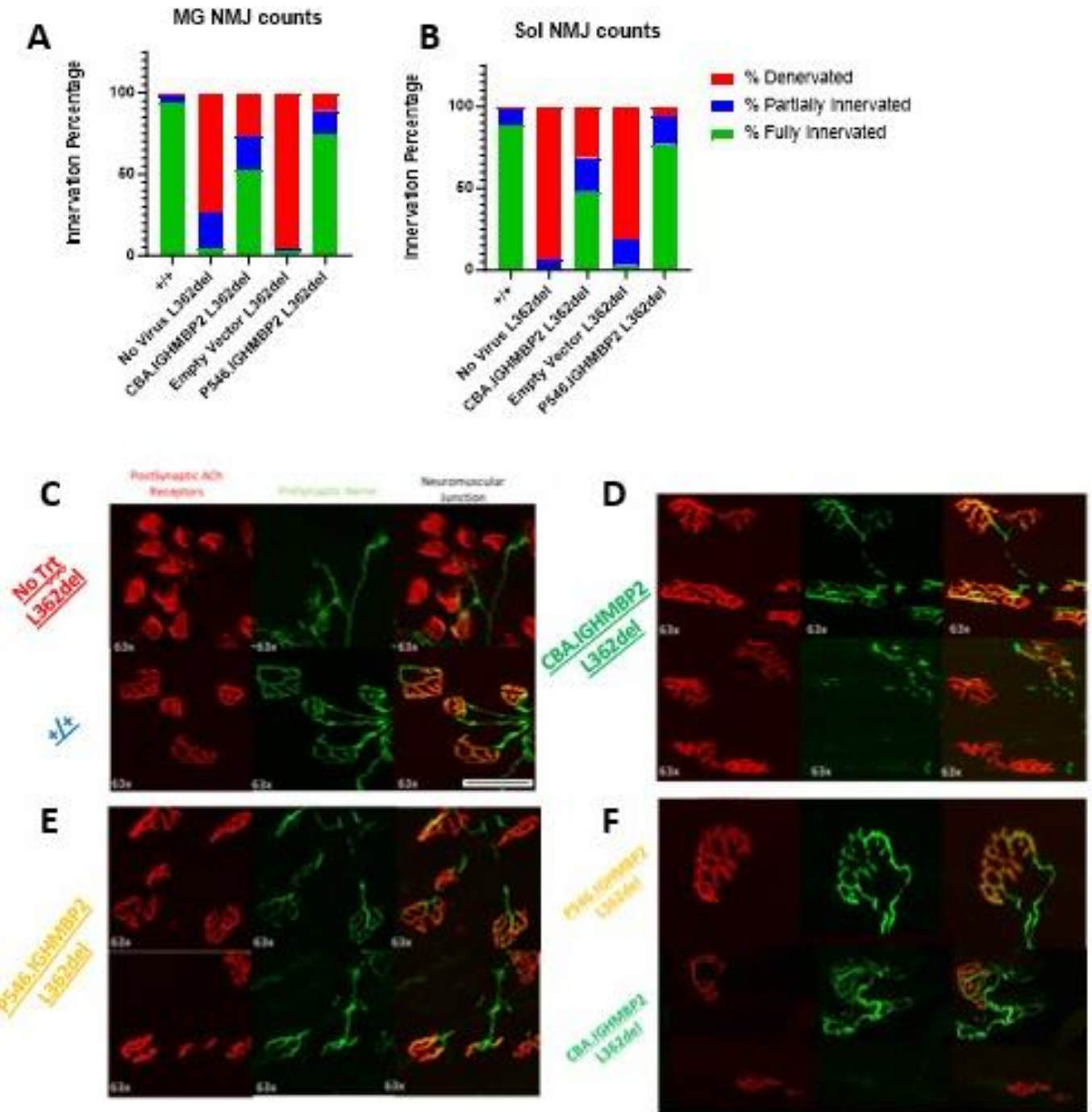
Supplemental Figure 9. CBA.IGHMBP2 and P546.IGHMBP2 L362del intercostal fibers are larger than

untreated mice but smaller than +/+.
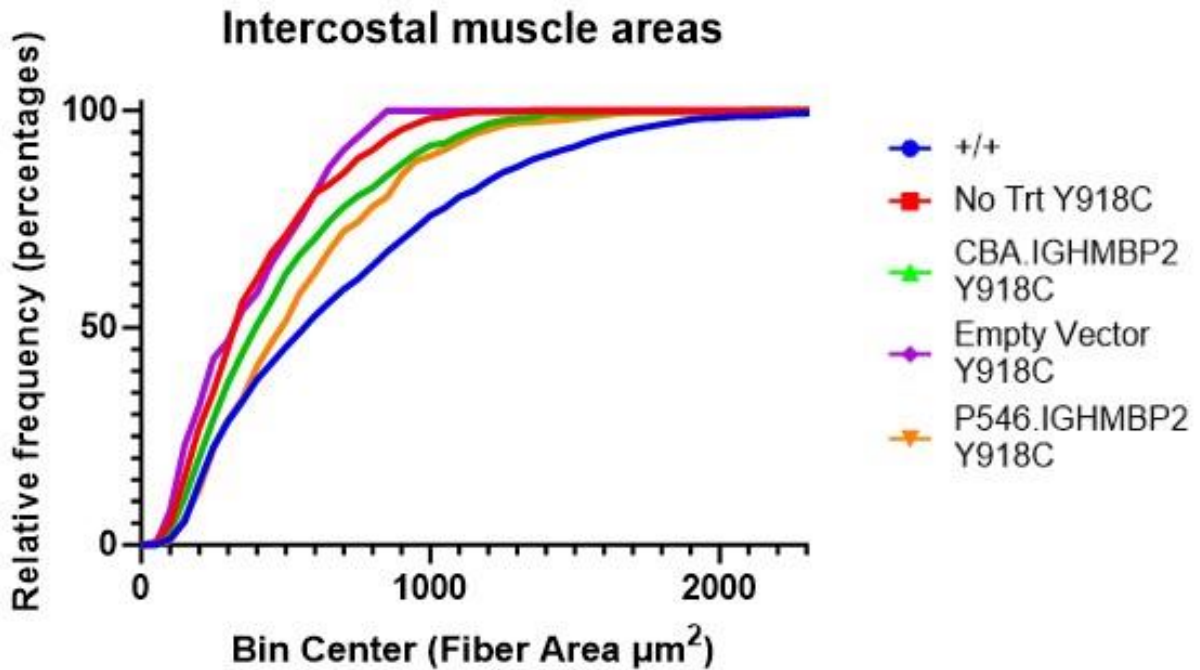
Supplemental Figure 9. CBA.IGHMBP2 and P546.IGHMBP2 L362del intercostal fibers are larger than untreated mice but smaller than +/+. The cumulative frequency of the Intercostal shows that CBA.IGHMBP2 and P546.IGHMBP2 mice are significantly different from +/+ (p<0.0001) and the untreated and empty vector L362del mice (p<0.0001). P546.IGMHBP2 also has significantly larger intercostal muscles compared to CBA.IGHMBP2 (p=0.0148). Untreated and empty vector Y918C are not significantly different form each other. Means: +/+ = 717μm +/- 507, Untreated Y918C = 415μm +/- 251, CBA.IGHMBP2 = 505μm +/- 324, Empty Vector Y918C = 389μm +/- 222, P546.IGHMBP2= 572μm +/- 340).

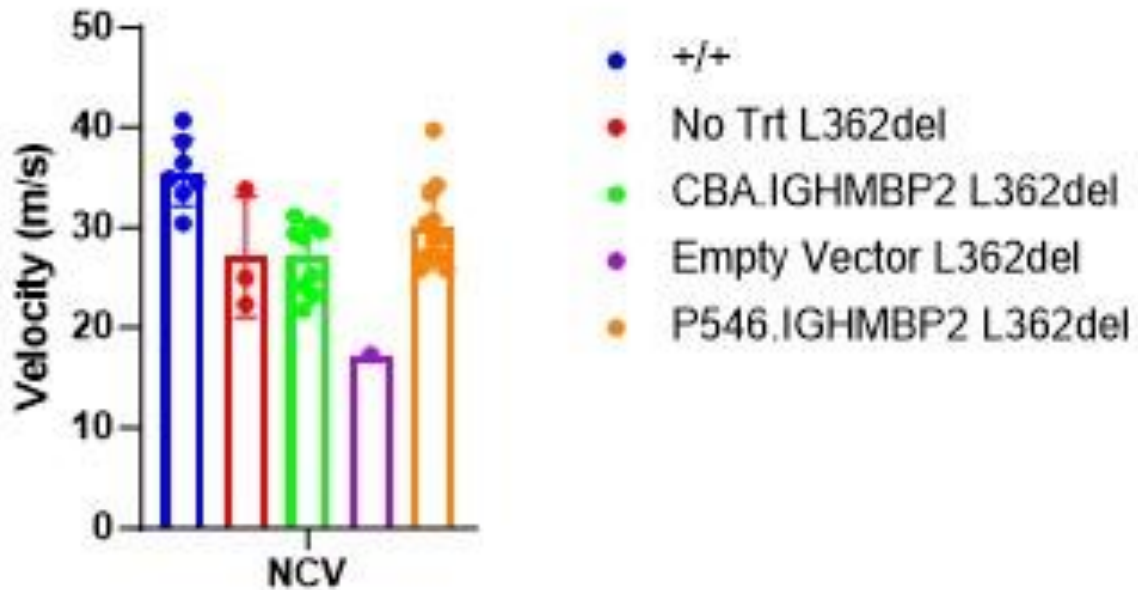**Supplemental Figure 10. CBA.IGHMBP2 L362del mice show signs of sprouting and reinnervation. (a)**

NMJ occupancy of the MG.

Supplemental Figure 10. CBA.IGHMBP2 L362del mice show signs of sprouting and reinnervation. (a) NMJ occupancy of the MG. +/+, CBA.IGHMBP2, and P546.IGHMBP2 L362del are significantly more innervated than the untreated or empty vector L362del mice (p<0.0001). +/+, CBA.IGHMBP2, and P546.IGHMBP2 L362del also show significant difference in full innervervated NMJ occupancy from each other. +/+ vs CBA.IGHMBP2 (p<0.0001). +/+ vs P546.IGHMBP2 (p=0.004). P546.IGHMBP2 has significantly more fully innervated NMJs than CBA.IGHMBP2 (p=0.0116). Untreated and empty vector mice are not significantly different. (b) NMJ occupancy of the Sol. +/+, CBA.IGHMBP2, and P546.IGHMBP2 L362del are significantly more innervated than the untreated or empty vector L362del mice (p<0.0001). +/+ and CBA.IGHMBP2 also show significant difference in full innervated NMJ occupancy from each other. +/+ and P546.IGHMBP2 are not significantly different from each other. +/+ vs CBA.IGHMBP2 (p<0.0001). P546.IGHMBP2 has significantly more fully innervated NMJs than CBA.IGHMBP2 (p=0.0106). Untreated and empty vector mice are not significantly different. (c) Immunofluorescent images of the NMJs of +/+ and untreated L362del mice show the vast difference between the denervation in the untreated L362del mice (no overlap of the red PostSynaptic Ach receptor channel and the green Presynaptic Nerve channel) and the fully innervation of the +/+ (complete overlap of the red PostSynaptic Ach receptor channel and the green Presynaptic Nerve channel making "pretzel" structures). White scale bar is 50 μm. (d) Immunofluorescent images of the CBA.IGHMBP2 L362del mice show elongated or "hotdog" like morphology of the NMJs and some partial and denervated NMJs. (e) Immunofluorescent images of the P546.IGHMBP2 L362del mice show typical "pretzel" like morphology of the NMJs. (f) Instances of sprouting and reinnervation in both CBA.IGHMBP2 and P546.IGHMBP2 models.

Supplemental Figure 11. Nerve Conduction velocities of treated L362del mice are not significantly increased from untreated L362del mice.

Supplemental Figure 11. Nerve Conduction velocities of treated L362del mice are not significantly increased from untreated L362del mice. CBA.IGHMBP2 and P546.IGHMBP2 models are significantly different from +/+, but not the untreated L362del mice. +/+ vs untreated L362del (p=0.0328). +/+ vs CBA.IGHMBP2 (p=0.0021). +/+ vs P546.IGHMBP2 (p=0.00434). Means: +/+ (N=7 = 35.6m/s +/- 3.4, Untreated L362del (N=3, 27.1m/s +/- 6), CBA.IGHMBP2 (N=9, 27.1m/s +/- 3.5, Empty Vector L362del (N=1, 17.3m/s +/- 0, P546.IGHMBP2 (N=12, 30m/s +/- 4.1).

Supplemental Figure 12. CBA.IGHMBP2 and P546.IGHMBP2 Y918C mice show difference in NMJ occupation from those of +/+, but do show significant difference in NCVs.
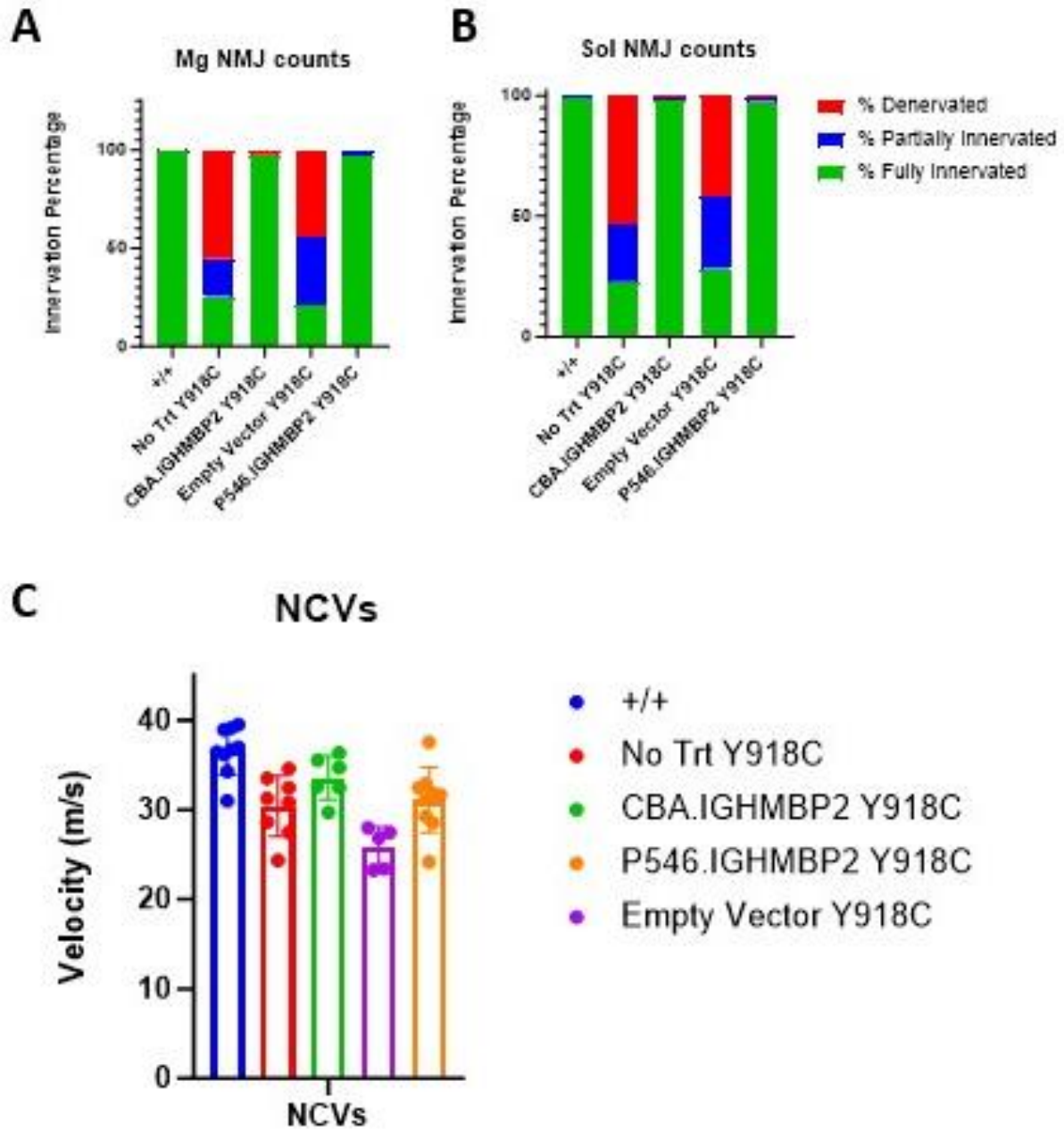
Supplemental Figure 12. CBA.IGHMBP2 and P546.IGHMBP2 Y918C mice show difference in NMJ occupation from those of +/+, but do show significant difference in NCVs. (a) NMJ occupancy of the MG. +/+, CBA.IGHMBP2, and P546.IGHMBP2 L362del are significantly more innervated than the untreated or empty vector Y918C mice (p<0.0001). +/+, CBA.IGHMBP2, and P546.IGHMBP2 L362del show no significant difference in fully innervated NMJ occupancy from each other. (b) NMJ occupancy of the Sol. +/+, CBA.IGHMBP2, and P546.IGHMBP2 L362del are significantly more innervated than the untreated or empty vector Y918C mice (p<0.0001). +/+, CBA.IGHMBP2, and P546.IGHMBP2 L362del show no significant difference in fully innervated NMJ occupancy from each other. (c) CBA.IGHMBP2 is not significantly different from +/+ and untreated Y918C mice. P546.IGHMBP2 is significantly different from +/+ (p=0.0044) but not untreated Y918C mice. However both CBA.IGHMBP2 and P546.IGHMBP2 are significantly different from empty vector mice (CBA.IGHMBP2: p=0.0166 ;P546.IGHMBP2: p=0.0299). Means: +/+ (N=9, 36.6m/s +/- 2.7, Untreated Y918C (N=8, 30.4m/s +/- 3.4), CBA.IGHMBP2 (N=6, 33.6m/s +/- 2.4, Empty Vector Y918C (N=5, 25.8m/s +/- 2.3, P546.IGHMBP2 (N=9, 31.1m/s +/- 3.6).

Supplemental figure 13. RLR Pathway.
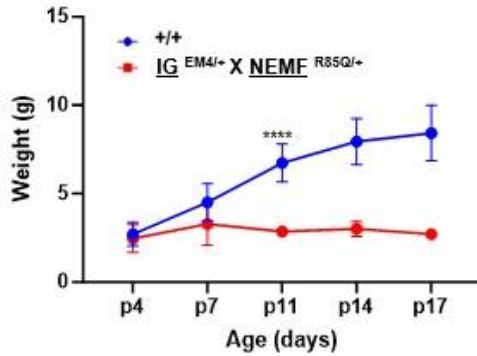

RIG-I Like Receptor Pathway
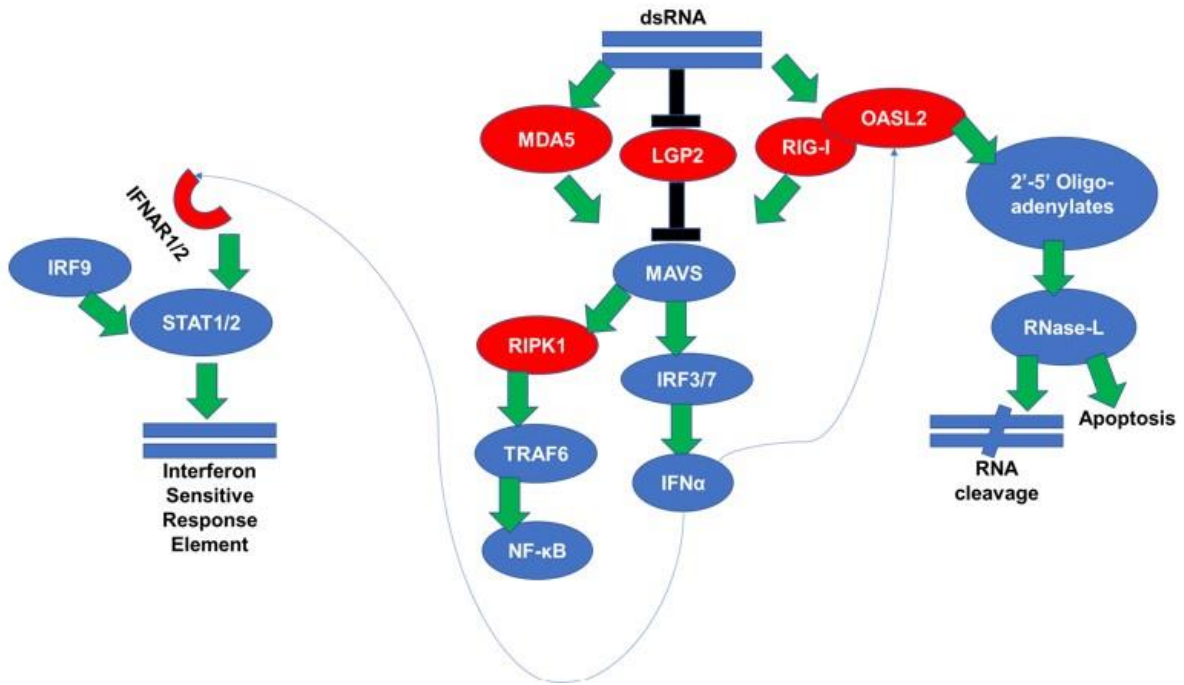
Supplemental figure 13. RLR Pathway. Diagram of RLR pathway with key genes for the various branches and sensors colored in red.
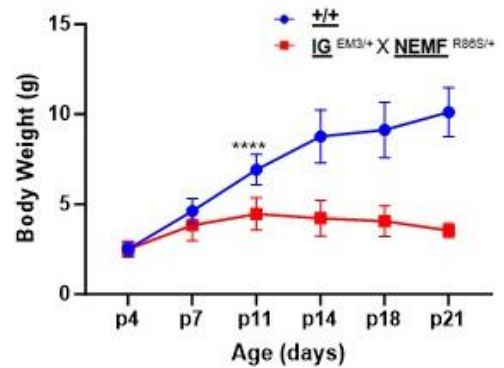
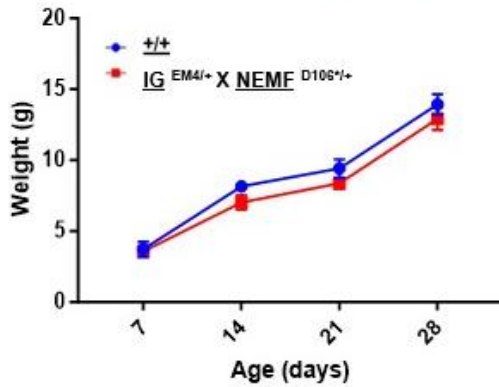**Supplementary Figure 14. Body Weights of IGHMBP2 x NEMF crosses.**
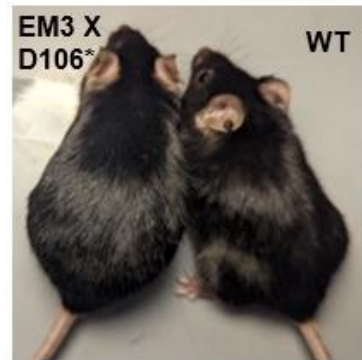
Supplementary Figure 14. Body Weights of IGHMBP2 x NEMF crosses. (a) There is a significant difference between +/+ (N=10) mice and IGHMBP2-EM4/+ x NEMF-R85Q/+ (N=10) mice starting at p11 (p<0.0001). (b) There is a significant difference between +/+ (N=10) and IGHMBP2-EM3/+ x NEMF-R86S/+ (N=9) mice starting at p11 (p<0.0001.) (c) There is no significant difference in body weights between +/+ (N=5) and IGHMBP2-EM4/+ x NEMF-D106/+ (N=4) mice. (d) IGHMBP2-EM3 x NEMF-D106* show no overt difference in size at 1.5 years from +/+.

BIOGRAPHY OF THE AUTHOR

Sarah Holbrook was born in Brunswick, Maine but spent most of her early years in Fort Fairfield, ME. Fort Fairfield is a small community in The County best known for its Potato Blossom Festival. This community helped nurture her love for academia and science with special thanks to Mr. Roberts, Ms. Kozura, Mr. Martin, and Mr. McCrea. She graduated summa cum laude with Honors in Biology with minors in Psychology and Neuroscience from the University of Maine. There she conducted research primarily in alcohol addiction and chronopsychobiology with the Rosenwasser lab. She was also under the tutelage of chytrid biologist, Joyce Longcore, and collaborated with several labs for her Honors thesis such as the Fremouw and Townsend labs. Sarah is a candidate for the Degree of Doctor of Philosophy

in Biomedical Science from the University of Maine, August 2024.